

## **ABSTRACT**

CANSIZOGLU, OMER. Mesh Structures with Tailored Properties and Applications in Hip Stems. (Under the direction of Ola Harrysson (chair) and Denis Marcellin-Little (co-chair).)

The purpose of the research has been to develop mesh structures with tailored properties for hip stems. Stress shielding is one of the crucial problems with current hip implants due to the modulus mismatch between the bone and the hip stem. Solid titanium or cobalt-chromium stems are changing the natural stress patterns in the femur. Stresses are transferred through the hip stem and are concentrated more at the distal end of the stem, which weakens the top portion of the femur and overloads the distal portion of the femur. Stress shielding in the long term may result in implant failure due to bone loss, which is costly and painful for the patient. Naturally, biomaterials have tailored structures that display optimal behaviors under tensile, bending and other applied loads. Bones are also tailored to the loading conditions and show stress patterns accordingly. This thesis reports on the development of new hip implants where the mechanical properties of the stems are tailored to match the bone's properties using open cell structures and mesh structures. Solid free form fabrication techniques are used in this thesis to manufacture parts in the Electron Beam Melting (EBM) by Arcam AB, Sweden. This processing method offers a unique way of making hip stems with mesh and solid sections together in one build. Different designs of hip stems have been manufactured and tested. Their affects on the bones have been analyzed and demonstrated using the Finite Element Analysis (ABAQUS). Hip implants were tested on cadaver bones to measure the difference between mesh stems and solid commercial hip stems. This thesis also includes studies about the mesh quality under different processing conditions, and the applications of structural optimization.

Mesh Structures with Tailored Properties  
and Applications in Hip Stems

by  
Omer Cansizoglu

A dissertation submitted to the Graduate Faculty of  
North Carolina State University  
in partial fulfillment of the  
requirements for the Degree of  
Doctor of Philosophy

Industrial Engineering

Raleigh, North Carolina

2008

APPROVED BY:

---

Dr. Denis J Marcellin-Little  
Co-Chair of Advisory Committee

---

Dr. Ola L.A Harrysson  
Chair of Advisory Committee

---

Dr. Denis Cormier  
Advisory Committee

---

Dr. Harvey A. West  
Advisory Committee

---

Dr. Afsaneh Rabiei  
Advisory Committee

## **DEDICATION**

Without my grandma's encouragement, I would have never gone to the primary school in Turkey. My parents, Kezban and Mehmet, always supported me during my education with undying sacrifices. My wife, Aysegul, helped to start and finish the PhD and always support me on every subject. My sister, Serap, always helped me to find my way in the undergraduate program at Bilkent University. My brother, Burak, helps me to keep up the morale. My relatives always support me to pursue higher degrees. I dedicate this work to all of them and to anyone who might benefit from it.

## **BIOGRAPHY**

Omer Cansizoglu was born in Eskisehir, Turkey. He obtained his bachelor's degree in Industrial Engineering from Bilkent University in 2003. He was accepted to the Ph.D. program at North Carolina State University after his BS Degree. He got interested in rapid manufacturing and tissue engineering after a couple of graduate courses at NC State University. He switched to the manufacturing concentration without prior experience. He practiced with all the equipment and all the machines in Parkshop lab and learned the practical manufacturing on his own. His advisors and their interesting projects motivate him to pursue a PhD in this research area. He decided to include the structural optimization into the rapid manufacturing area after learning about unit cell generation in tissue engineering with topology optimization methods. He has developed hip stems with tailored structures, which is a novel medical implant. His research interests include structural optimization, rapid manufacturing, medical implants, manufacturing process development, and robotics.

# Acknowledgements

My sincere thanks go to my advisors, Dr. Ola Harrysson and Dr. Denis Marcellin-Little, and to the other members of my Ph.D. committee at North Carolina State University (NCSU), for their invaluable help and support during the entire research. I also thank all the members of the Edward P. Fitts Department of Industrial and Systems Engineering at NCSU, who were my great supporters during my doctoral study. I acknowledge them for their continuous support and encouragement.

I appreciated the help from Dr. Peter Mente, Dr. Simon Roe, and Mr. Ryan McCulloch for helping me to set up the implant testing.

Staff at Harnett county animal shelter was very friendly and helpful in bone collection.

I acknowledge my friends Tushar Mahale, Kyle Knowlson, Daniel Brooks, Dimitrios Makrozahopoulos, Engin Murat Reis, Merivan Tunc Reis, Murat Erenli, Canguzel and Fahir Zulfikar, Mustafa Bakkal, Hilmi Aydin, Evren Tipi, Bugra Akben, Burcu Ozcam, Rabiya Zeynep Sarica, for their continuous support at NC State.

# TABLE OF CONTENTS

<b>List of Tables .....</b>	<b>vii</b>
<b>List of Figures.....</b>	<b>viii</b>
<b>1. Introduction.....</b>	<b>1</b>
<b>2. Mesh Structure Development.....</b>	<b>6</b>
2.1. REVIEW OF MESH STRUCTURE MANUFACTURING .....	6
2.1.1. Plasma Spray .....	8
2.1.2. Combustion synthesis.....	8
2.1.3. Powder metallurgy .....	9
2.1.4. Electrical Discharge Compaction .....	9
2.1.5. Plastic mold techniques .....	10
2.1.6. Wire Mesh .....	10
2.1.7. Vapor deposition .....	10
2.1.8. Orientation with Magnetic field .....	12
2.1.9. Chemical Etching .....	13
2.1.10. Selective laser sintering.....	15
2.1.11. Direct metal laser sintering (DMLS).....	15
2.1.12. Laser Engineered Net Shaping .....	16
2.1.13. Microsintering .....	18
2.1.14. 3D printing .....	19
2.1.15. 3D fiber deposition.....	21
2.1.16. Electron Beam Melting.....	21
2.2. MECHANICAL BEHAVIOR OF METALLIC FOAMS .....	27
2.3. INITIAL HEXAGON MESHES .....	35
2.3.1. Design and Fabrication of Structures.....	38
2.3.2. Compression Test Procedure .....	39
2.3.3. Flexural Test Procedure .....	40
2.3.4. Experimental results.....	41
2.3.5. Finite element modeling.....	46
2.3.6. Discussion.....	47
2.3.7. Conclusions and Future Directions .....	49
2.4. RHOMBIC STRUCTURES .....	50
2.4.1. EBM Manufacturing .....	52
2.4.2. Testing .....	52
2.4.3. Analysis and FEA .....	53
2.4.4. Compression Testing .....	54
2.4.5. Flexure Testing.....	57
2.4.6. Discussion and Conclusions.....	58
2.5. MELTING EFFECTS ON MESH STRUCTURES .....	60
2.5.1. Structure Design.....	60
2.5.2. Manufacturing.....	61
2.5.3. Mechanical testing.....	62
2.5.4. Results and Discussion .....	62
<b>3. Applications of Structural Optimization .....</b>	<b>66</b>
3.1. TOPOLOGY OPTIMIZATION .....	66
3.1.1. Results from topology optimization .....	74
3.2. MESH BASED OPTIMIZATION.....	79
3.2.1. Updating Iterations: Optimization Methods.....	80

3.3.	OPTIMIZED MESH STRUCTURES .....	81
3.3.1.	<i>Design of structures</i> .....	81
3.3.2.	<i>Optimization of structures</i> .....	83
3.3.3.	<i>Fabrication of structures</i> .....	90
3.3.4.	<i>Testing of structures</i> .....	91
3.3.5.	<i>Discussion</i> .....	93
3.3.6.	<i>Conclusion</i> .....	95
<b>4.</b>	<b>Design and fabrication of hip stems .....</b>	<b>96</b>
4.1.	HIP IMPLANT SYSTEMS.....	96
4.2.	BONE REMODELING.....	101
4.2.1.	<i>Bone Remodeling Models</i> .....	102
4.3.	DESIGNS TO PREVENT STRESS SHIELDING .....	104
4.3.1.	<i>Different geometric designs</i> .....	104
4.3.2.	<i>Composite stems</i> .....	109
4.4.	PATENTS RELATED TO REDUCED STRESS SHIELDING.....	115
4.5.	METAL MESH STEMS.....	116
<b>5.</b>	<b>Biomechanical Testing of stems .....</b>	<b>124</b>
5.1.	IN VITRO TESTING.....	127
5.1.1.	<i>Overview</i> .....	127
5.1.2.	<i>Materials and Methods</i> .....	127
5.1.3.	<i>Results and Discussion</i> .....	132
5.1.4.	<i>Conclusion</i> .....	134
<b>6.</b>	<b>Conclusion and Future Work.....</b>	<b>136</b>
<b>7.</b>	<b>References.....</b>	<b>138</b>
<b>8.</b>	<b>Appendix .....</b>	<b>150</b>
8.1.	APPENDIX 1 .....	151
8.2.	APPENDIX 2.....	152
8.3.	APPENDIX 3.....	155

## LIST OF TABLES

Table 1: Cell type and some of the manufacturing methods are listed. ....	7
Table 2: Some of the companies related with laser fabrication process. Source: (Santos, Shiomi et al. 2006), reprinted by permission from Elsevier.....	15
Table 3: Summarizes compression test results for 4 mm, 5 mm and 6 mm structures.....	43
Table 4: Bending test results .....	46
Table 5: Compression testing of rhombic structures with cell sizes from 3 mm to 12 mm. ....	55
Table 6: Comparison of tested structures and simulated structures with 0.49 mm <sup>2</sup> square profile beams. ....	57
Table 7: Bending test results for 3mm, 6mm, and 8 mm structures .....	58
Table 8: Melting parameters for 3 sets of mesh structure samples.....	61
Table 9: Beam thicknesses and comparison to the max force .....	65
Table 10: Compliance ratios in testing and FEA for updated coordinates and thicknesses .....	92
Table 11: Material combinations and wear rates. SOURCE : (Semlitsch and Willert 1997) .....	97
Table 12: 800N measurement of 9 paired samples .....	133
Table 13: 1600N measurement of 6 paired samples .....	134
Table 14: List of Cadaver Bones .....	151
Table 15: Cadavre surgery notes .....	152
Table 16: Xray templating.....	155

## LIST OF FIGURES

Figure 1: Trabecular Metal (Zimmer, Inc, Warsaw, Ind previously Hedrocel, Implex Corp.), (Boby, Stackpool et al. 1999), Reprinted by permission from the author.....	11
Figure 2: Low relative density honeycomb core manufacturing (Wadley, Fleck et al. 2003), Reprinted by permission from Elsevier.....	12
Figure 3: Magnetic field applied while filling the cavity. Source: (Chino, Mabuchi et al. 2006) ,Reprinted by permission from Elsevier.....	13
Figure 4: Structure of the multilayered mesh surface. (a) Pattern design and (b) Laminations. Source: (Kusakabe, Sakamaki et al. 2004), Reprinted by permission from Elsevier.....	14
Figure 5: 3D mesh structures in stainless steel and in cobalt-chrome Source: <a href="http://www.mcp-group.com/rpt/rpttslm_1.html">http://www.mcp-group.com/rpt/rpttslm_1.html</a> reprinted by permission from the MCP-group.com.....	16
Figure 6: OPTOMECC, medical device fabrication. Source: <a href="http://www.optomec.com">http://www.optomec.com</a> , LENS®, reprinted by permission from Optomec.....	17
Figure 7: Parts from the LENS process. Source: (Wu and Mei 2003) reprinted by permission from Elsevier.....	18
Figure 8: Powder deposition with adjustable layer thickness and density. Source: (Haferkamp, Ostendorf et al. 2004) reprinted by permission from Elsevier.....	19
Figure 9: 3D printer (Curodeau, Sachs et al. 2000) , Copyright © 2000. Reprinted by permission of John Wiley & Sons, Inc.....	20
Figure 10 : Different surface texture geometries and surface image of the castings (Curodeau, Sachs et al. 2000) , Copyright © 2000. Reprinted by permission of John Wiley & Sons, Inc.....	21
Figure 11: Sketch illustrated the Beam control system Source: EBM manual .....	22
Figure 12 : Electron beam is melting the current layer (CoCr test parts in EBM S12) .....	25
Figure 13: EBM build platform with sintered powder surrounding the actual parts. ....	25
Figure 14: Compressive stress-strain curve for 6101 Al foam (9.2% density), (Nieh, Higashi et al. 2000) reprinted by permission from Elsevier.....	28
Figure 15: a) $M < 0$ and it is a bending mechanism b) $M = 0$ and It is stiff with horizontal beam in tension c) $M > 0$ and it is over-constrained.....	29
Figure 16: A stress-strain curve of a cellular solid with typical densification. ....	31
Figure 17: Structures with straight holes were manufactured using EBM.....	32
Figure 18: Less stiff implant designed with straight holes.....	33
Figure 19: Edges of Honeycomb are intertwined to other layer in variable porosity.....	33
Figure 20: Titanium solid model of the honeycomb design made with EBM. ....	34
Figure 21: Flexible implant example from different views.....	34
Figure 22: a) beam thickness is shown before slicing of the beam b) Overlaps, defined as $L1-L2$ , between successive layers are shown with the related parameters. ....	36
Figure 23: Close up view of Strut Qualities from earlier samples.....	36
Figure 24: Range of Strut Qualities for same beam melting parameters at same micrograph scale a) 20°, b) 30°, c) 40°, d) 50°, e) 60°, f) 70°, g) 80° angle with respect to XY plane.....	37
Figure 25: a) Top view shows 0.7mm beam thickness, 4mm cell size, and build angle of 30° b) Front view , c) Isometric View of Hexagonal Lattice Structure.....	39

Figure 26: Compression Specimens with 2mm (not tested),3mm (not tested),4 mm, 5 mm, and 6 mm Unit Cell Dimensions.....	39
Figure 27: Compression test was done using parallels at each face for 4mm, 5mm and 6mm cell sizes.....	40
Figure 28: Compression Test Results for 4mm structures with maximum loading up to 5500N .....	42
Figure 29: Compression Test Results for 5mm structures with maximum loading up to 2400 N .....	42
Figure 30: Compression Test Results for 6mm structures .....	43
Figure 31: Comparison of tested and estimated results A) Compressive strength as a function of relative structure density B) Elastic modulus (E) as a function of relative structure density .....	45
Figure 32: a) two copies each of three different bend specimens with cell sizes of 4 mm, 5 mm and 6 mm b) Flexural testing .....	45
Figure 33: Elastic modulus (E) versus relative density for different builds of specimens. Each build has 2 copies of each unit size of long beams. Data points are average of each build sets for each cell sizes. ....	46
Figure 34: a) Simulated FEA results for different beam thickness of different cell sizes b) Comparison of ANSYS results and Testing results in scaling .....	47
Figure 35: SEM picture of Lattice structure is showing the unmelted powder attached to the beams. ....	48
Figure 36: SEM picture of the crushed lattice structure is shown with sintered Ti64 powder particles. ....	48
Figure 37: a) Relative dimensions of one face of the rhombic dodecahedron unit cell b) front view of the unit cell c) rectangular flexural test bar with rhombic dodecahedron unit cells .....	50
Figure 38: Principal fabrication of thin struts using layered fabrication technology. ....	51
Figure 39: Structures fabricated via Electron Beam Melting: a) Cubes with 40% relative density (60% porous) b) Cubes with relative densities of 8.0%, 5.0%, and 3.8% c) Bending specimens with 8 mm and 6 mm cell sizes (7.3% and 11.9% relative density) ..	52
Figure 40: Three point flexure testing of rectangular mesh beam.....	53
Figure 41: ANSYS simulated mesh structure.....	53
Figure 42: a) Average compression strength versus relative density for tested and estimated mesh structures b) Ansys simulated results for compression stiffness versus relative density in XY orientation and Z orientation. ....	56
Figure 43: Bending test results for specimens with unit cell size of 3 mm and 40% relative density. ....	58
Figure 44: Top and front views of the sample a) mesh with extra 3D diagonal beams b) mesh with extra vertical beams c) extra 2D side crosses d) control structure without supports .....	62
Figure 45: Load versus displacement data of Set 1 sample are shown in the figure. P1-1 is referring to sample A and numbering is consistent with the given sample figure.....	63
Figure 46: P2-1, Set 2 sample, is referring to sample A and numbering is consistent with the given sample figure. ....	63
Figure 47: P3-1, Set 3 sample, is referring to sample A and numbering is consistent with the given sample figure. ....	64

Figure 48: Molds and sintered final parts. (Hollister, Maddox et al. 2002) with permission from Elsevier. ....	69
Figure 49: Porosity level 49% for mandibular condyle (Lin, Kikuchi et al. 2004) reprinted with permission from Elsevier. ....	71
Figure 50: Porosity level 35% for mandibular condyle (Lin, Kikuchi et al. 2004) reprinted with permission from Elsevier. ....	71
Figure 51: Design domain and resulted optimal topology with support design method, (Buhl 2002) reprinted with permission from Elsevier. ....	73
Figure 52: SEM photo of 3D compliant mechanism and experimental measurement set up, (Huang and Lan 2006) with permission from IOP publishing. ....	74
Figure 53: Left side of the material boundary was fixed and loading was at right bottom corner in -Fx and Fy direction. Volume reduction is constrained to 50% with 60 iterations. ....	75
Figure 54: Volume reduction is constrained to 75% with 20 iterations. ....	75
Figure 55: 3D volume topology optimization example. Force is applied at the bottom corners. Structure volume reduced to 50% of initial boundary volume. Left are density readings in the boundary. Right is one slice showing the cross section density. ....	75
Figure 56: Selected elements based on density of 0.9. Zero density means void. ....	76
Figure 57: Mitchell type test part original and simplified. ....	76
Figure 58: Original structure and final structure with element densities in the topology optimization modules (ANSYS). ....	77
Figure 59: Outside nodes of the selected elements which have densities between 0.4 and 1. ....	77
Figure 60: Geomagic point processing to make surfaces for this 2D part. ....	77
Figure 61: Magics stl file fixing for RP process. ....	78
Figure 62: Some of the features are recognized in SolidWorks ....	78
Figure 63: Final Mitchell structure made from Ti6Al4V powder using the EBM S12. ....	79
Figure 64: a) 10 vertices are defined for each beam and 2 of them are actual nodal points. b) Two beams are shown without additional cube at intersection. ....	82
Figure 65: a) Original STL-file of two dimensional truss beams constructed from FEA truss elements b) stl-file of simplified two dimensional truss beam. ....	83
Figure 66: 2D cantilever beam example ....	86
Figure 67: a) Original 3D grid with dimensions of 20 x 20 x 20 mm b) Analysis output structure in 3D beams c) Output structure as STL-file format. ....	87
Figure 68: a) 3D grid with the dimensions 20X20X20 mm b) Solution output structure in beam elements c) Output structure as STL-file format (Figures are not at same scale) ....	88
Figure 69: a) Overall dimensions of the structure are 12 mm in Z and 10.4 mm in X and Y, where $a=1.5$ and $b=a/\tan(30)$ , b) Input 3D lattice structure in MATLAB, c) Output 3D lattice structure in the STL-format. ....	89
Figure 70: Compliance and constraint history of rhombic structures for 200 iterations ...	89
Figure 71: a) 2d cross sections for initial implant mesh b) after node movement cycle in 2d beam plots c) initial structure in Magics, and d) output structure in Magics ....	90
Figure 72: Optimized and original structures fabricated using an SLA 190 and EBM. ....	91
Figure 73: a) 2D grid, EBM part, original versus optimized structure is shown optimized/original stiffness ratio 1.42 b) Plastic 3D grid optimized/original stiffness ratio 7.02. ....	92

Figure 74: a) Cube grid 2, EBM part, for loading in x direction (shear) ratio is 1459.1/390.31=3.73. b) Cube grid 1, EBM part, in compression loading ratio is 2.52 (beams are ~2mm) .....	92
Figure 75: Load and displacement after structures contacted the loading plates entirely. Optimized over original stiffness ratio is 1.71.....	93
Figure 76: a) A thin low angled beam structure fabricated using the EBM technology b) effect of low build angle on thin beam structures structure .....	94
Figure 77: A cervico-trochanteric prosthesis: (a) inner side, (b) outer side, and (c) configuration with three screws. Source: (Tai, Shih et al. 2003) with permission from Elsevier.....	105
Figure 78: The loading configuration of generated 3-D finite meshes for the (a) intact, (b) C-T, and (c) PCA implanted femora. Source: (Tai, Shih et al. 2003) with permission from Elsevier. ....	105
Figure 79 : Maximum principal stresses within the cement mantle for the Charnley stem with a proximal bond (A), Charnley stem without a proximal bond (B), Distal-Round stem with a proximal bond (C), and Distal-Round stem without a proximal bond (D). Source: (Mann, Bartel et al. 1997).....	106
Figure 80: Progression of flat-collared, conical-collared, and collarless tapered stem designs. Source: (Mandell, Carter et al. 2004), with permission from the author.....	107
Figure 81: Simple stem designs for less stress shielding. Source:(Gross and Abel 2001), with permission from Elsevier.....	108
Figure 82 : Modern tapered rectangular press fit design of Zweymuller (SL-Plus, Plus Orthopedics AG, Rotkreuz, Switzerland). Source: (Swanson 2005), with permission from Elsevier. ....	109
Figure 83: Mechanical behavior of composite stem made using carbon fibers and glass fabric pre-impregnated with poly-etherimide C-G/PEI (Santis, Ambrosio et al. 2000) with permission from Elsevier.....	114
Figure 84: Long carbon fibers closed the carbon powder core, (Adam, Hammer et al. 2002) with permission from Elsevier. ....	114
Figure 85: Modular hip implant, U.S. Pat. No. 6,319,286. ....	115
Figure 86: Different configurations of hip stems a) Mesh block, Solid hip stem, and resulting mesh hip stem b) Complete mesh hip stem after Boolean operations. c) Solid hip stem with holes. ....	117
Figure 87: Hip stems with mesh, with holes, and solid from (left to right). ....	117
Figure 88: Results of bend testing of solid stem, stem with holes, and stem with mesh structure are shown in the graph .....	118
Figure 89: Testing of the hip stems.....	118
Figure 90: Finite Element Analysis tetrahedral meshes of the femur-hip implant assembly and hip stem.....	119
Figure 91: Left) Von Mises stresses at the same scale show results for solid Co-Cr stem, solid Ti-6Al-4V stem, and mesh Ti-6Al-4V stem from left to right. Right) Von Mises stresses on the femur for a) Co-Cr stem b) Ti-6Al-4V stem c) mesh Ti-6Al-4V stem at the same stress color coding. ....	120
Figure 92: Left) Hip stems size9 and 10 were manufactured with reference features Right) Wafer supports are shown on the part surface.....	121
Figure 93: Left) Solid hip stem without bone ingrowth region, Right) Bone ingrowth region.....	123

Figure 94: Hip stem with bone ingrowth meshes and reference features for finishing. ..	123
Figure 95: Strain gages at five levels are shown at heel strike loading set up, (Waide, Cristofolini et al. 2003), reprinted with permission from Elsevier. ....	125
Figure 96: Left) Hip stems were aligned vertically at 10° with using impaction hole in the stem, and Right) aligned horizontally with reference to the screws on the alignment fixture. ....	128
Figure 97: Four strain gages were attached at the bending direction and one is at the same level at strain gage-2 opposite direction.....	129
Figure 98: Example test set up which shows 4 strain gages, (Munting and Verhelpen, 1995) .....	130
Figure 99: In Vitro testing set up for hip stems. ....	130
Figure 100: Close up view of implant head and cup in a testing set up.....	131
Figure 101: Strain Gage readings for Bone11-BFX at 1600N loading.....	133

# 1. INTRODUCTION

Osteoarthritis (OA), rheumatoid arthritis (RA), avascular necrosis, and trauma may cause defects at the cartilage. OA alone indicates the degeneration of articular cartilage together with the changes in the subchondral bone and mild intraarticular inflammation. A number of environmental risk factors, such as obesity, occupation, and trauma, may initiate various pathological pathways (Sarzi-Puttini, Cimmino et al. 2005). Severe defects in cartilage lead to pain and loss of joint function. Hip implants are used to replace the socket and head of the femur with artificial components, when surgery is the only option. There are also alternative treatments for different stages of the defects in cartilage such as cartilage replacement, surface replacement of the femoral head, and pain reducing drugs for early stages. Cartilage replacement is still at infancy. Tissue engineering has been used, but cell selection, scaffold design and biological stimulation are the current challenges of cartilage replacement. Drugs are used to adequately control pain, improve function, and reduce disability when applicable.

Hip implants have been used since the 18<sup>th</sup> century (Scales 1966). The Rigid fixation method became popular with Charnley's technique (Charnley 1960). Charnley's technique has a very high rate of success in the older population (Madey, Callaghan et al. 1997). However, a lower success rate has been reported for younger patients. The average implant life time is 10 to 15 years and depends on the patient, implant type, fixation methods, and materials. Ultra High Molecular Weight Polyethylene (UHMWPE) is still used in the acetabular cup of hip implants today, but new materials have been studied from ceramics to different metals to get less wear rate than UHMWPE. A different

version of this material has also been developed to solve the wear problem in UHMWPE. Structure, morphology, and mechanical properties of the polymer have been studied at different stages of the production (Kurtz, Muratoglu et al. 1999). Metal-on-plastic combinations have been widely used in the industry. Alternative combinations are a ceramic head on a ceramic cup, a metal head on a metal cup, and a metal head on a ceramic cup. New material development is continuing to decrease the wear rate in hip and knee implants.

Cementless implants have been developed as an alternative to cemented implants. In cementless implants, the implant surface is coated with metal beads, meshes, or fine particles for bone ingrowth. Implant loosening was associated with the cement in the literature and studies have focused on porous coatings. Different manufacturing methods have been tried to get good surface adhesion between bones and implant coating.

The differences in patient anatomy are important for cementless implants, and the surgeon has to make sure that the implant is positioned firmly to assure good initial fixation for bone ingrowth. Long term success is related with the fit between implant and bone. Modular implants have been developed to provide flexibility in the options available for each bone. In modular implant systems, different sizes of the stem, head, and acetabular cup can be used to improve the fit between implant and bone. Modular implants with too many components are not acceptable to surgeons. Each additional component is creating a risk of extra metal wear particles and this is related to widely known problems. Implants are expected to stay in the body for a long period of time, so implant performance is important to avoid revision surgery. A new era of implants has been started with a customization of implants to the patients. Customization of implants has been done before with low-end technology. For bone plates, surgeons have been

manually bending and fitting the plates to the bone to have a good fit at the interface (Imatani, Ogura et al. 2005). High tech methods have enabled surgeons to just use the customized implants designed and manufactured before the surgery without manual adjustments. Customization of the implants to each patient has been successfully done with the help of 3D imaging software and new manufacturing techniques.

Another problem with implants is that the stiffness between bone and implant are mismatched. Titanium hip stems have a modulus of 110 GPa, while the modulus of the bones are 15-20 GPa. The increase in the stiffness of the implant creates more stress shielding. Cobalt chrome stems have higher modulus than titanium stems and also increased stress shielding. Metal stems distort the loading mechanism of the bone. Stresses around the femur change with stiff stems, which is explained in the next sections. Rigid hip implant stems result in less load transfer proximally leading to the stress shielding of the proximal femur. A decrease in stress levels around the bone will decrease the density of the bone, which will make it more susceptible to failure. Lower stiffness material will transfer the load more proximally, but it will result in higher load transfer stresses at the bone and implant interfaces with the risk of interface failure. Implant micromotions will increase with a more flexible implant. There is a trade off between stress shielding and implant failure. Many studies have analyzed different geometries and materials to solve these discussed problems. Femur head replacement has been tried instead of inserting a solid stem into the femur with a low success rate. Femur head replacement is also limited to special cases. Composite hip implants and modular hip implants have been tried without much success. Different hip implant designs have also been studied to reduce the stress shielding. Different implants with lower stiffness have been observed to show less stress shielding than stiffer implants when using finite

element analysis (FEA), and also in testing. The degree of flexibility of the implant depends on the bone density of the patient, which changes according to the age, activity level, hormone level and so on. Therefore, each bone will require different implant geometries and implant mechanical properties.

With the advent of the Rapid Prototyping (RP) technologies, each patient's bone properties can be used to design an optimal hip implant. This multidisciplinary work will include the design, analysis, manufacturing, and testing of the hip stems. Hip stems will be manufactured with internal structure out of titanium. The hip implants will be designed using Mimics (Materialise, Belgium), MAGICS X and Solid Works 2005. An internal structure will be designed to match the desired stiffness at different sections. Initially, grooves and holes will be designed and optimized with design analysis in ANSYS according to the required stress and strain energy levels. Internal mesh structures will be designed according to the material properties of the metal and the bone. Design iterations will be evaluated in FEA using ANSYS. Mechanical tests will be done for manufactured representative blocks and hip stem alternatives. Stress and strain levels around the implant will be measured for different designs. Electron Beam Melting (EBM), 3D Printing (Zcorp, MA, US), Fused Deposition Modeling (FDM) processes will be used to build models for visual inspection and functional testing. Final implants will be manufactured with bone in-growth surfaces using a minimum number of steps, which is revolutionary compared to the current manufacturing techniques for implants. The top and bottom surfaces of the implant will be CNC machined in a 4-axis milling machine for final dimensions. In a future study, clinical trials will be done for successful designs and bone remodeling simulations will be done for different implant designs. Accumulated and

developed topological design methods and manufacturing techniques will be applied to other implants and other areas which require the development of tailored part properties.

This thesis combines RP technologies and design optimization methods to develop and manufacture hip stems with custom flexural modulus.. The long term goal will be to use the combination of solid free form fabrication and topological design optimization. This goal will have a higher impact on increasing the efficiency of the products. Product weight and performance will be designed optimally and complex RP processes will be capable of fabricating those products by satisfying the process specific constraints. 2D and 3D structures with customized mechanical properties will be possible with layout optimization methods and RP. Recent examples of the method and details about hip stems are given in the next sections.

## **2. MESH STRUCTURE DEVELOPMENT**

Metal foam and metal lattice structure manufacturing methods are related to this study. Some manufacturing methods especially related to open cell structures are reviewed in this section.

### **2.1. Review of mesh structure manufacturing**

Homogenous porous systems have been fabricated using many different methods. Porous metallic systems can be divided into closed cell and open cell structures. Closed cell foams are usually resulting from random foaming processes. Porous material properties are controlled by the pore size, shape and pore distribution (Brothers and Dunand 2006). Energy absorption is one of the primary applications of porous metal structures. Rabiei et al. developed a new composite metal foam which uses hollow spheres that are packed into random order and infiltrated with an aluminum alloy (Rabiei and O'Neill 2005). This foam showed superior compressive strength that averaged around 67MPa and good energy absorption. Their recent work about Al-steel composite cast foam at relative density of ~42% showed plateau stresses of 50-90MPa and a strength/density ratio of 21-37 (Vendra and Rabiei 2007).

Various fabrication processes have been developed to produce porous metallic systems. Some of them are listed in Table 1 below.

**Table 1: Cell type and some of the manufacturing methods are listed.**

<b>Cell type</b>	<b>Method</b>
Closed	Gas Injection
Closed	Decomposition of foaming agents
Open	Sintered metal powders
Open	Sintered metal fibers
Open	Space holder method
Open	Replication
Open	Combustion synthesis
Open	Plasma spraying
Open	Oriented wire mesh
Open	Vapor deposition
Open	Rapid Prototyping
Open	Electro discharge compaction

Some of the processes such as casting or vaporous deposition have more control over pore size, interconnection and distribution, while other processes such as decomposition of foaming agent result in more random pores. Challenges for porous materials besides pore size control are fatigue strength (Yue, Pilliar et al. 1984; Crowninshield 1986) and corrosion (Jacobs, Gilbers et al. 1998). Some of the processes related to the open cellular structures are explained in detail in the next sections.

### **2.1.1. Plasma Spray**

Plasma spraying can be used to create varying porosity in the surfaces (Ryan, Pandit et al. 2006). It has been used to create 3 different layers of surface coating for implants. Yang et al. prepared graded porous coatings by regulating the spraying power and the content of Ti powder (Yang, Tian et al. 2000). Small particles melted and formed the dense region, while large particles partly melted and formed the macro pores. Mechanical, physical and metallurgical bonding between the Ti substrate and coating was observed. Sandblasting treatment was observed to increase the mechanical bonding. The physical attraction between the Ti substrate and the coatings was also observed. A reducing working atmosphere helped to reduce the oxide layer thickness, which helped with the direct contact of powder and base. The porous coating was prepared as a dense layer near the surface of the substrate, micro pores at the middle, and macro pores at the outside.

### **2.1.2. Combustion synthesis**

Combustion synthesis has been used to produce metallic foams. Reactants are mixed and cold pressed. Samples are placed in an inert atmosphere and ignited to start the thermal explosion mode or self-propagating high thermal synthesis. Zhang X et al. used combustion synthesis to produce porous surfaces that resulted in bone ingrowths without an immune response (Zhang, Ayers et al. 2001). One of the process advantages was high purity of the foams. Kanetake et al. synthesized nickel aluminide foam and porous Ti composite (TiC, TiB<sub>2</sub>/Ti) (Kanetake and Kobashi 2006). An exothermic reaction between the Ti and C or the Ti and B<sub>4</sub>C was used to make the titanium foams. To increase

the porosity, foaming agents were mixed with the base powders before the reaction. Effects of the different blending ratios were observed on the pore morphology. Porosity of the precursor also affected the pore morphology. Open pore structures were obtained by using a low titanium blending ratio and highly porous initial compacted material. Closed pores were obtained with higher Ti/B<sub>4</sub>C ratio, which increased the fluidity of Ti and tendency to form spherical pores with surface tension.

### **2.1.3. Powder metallurgy**

Powder metallurgy is a common technique for producing cellular structures. Porosity is the natural result of the process. For dense parts, parts manufactured by powder metallurgy are infiltrated with other materials to fill the porosity. Porosity levels can be increased by adding blowing agents. The mixture is compacted to get a semi finished product. After that, it is heat treated near the melting temperature of the matrix material. The blowing agent releases gas while the matrix is at the elevated temperature. These methods are suitable for Al, Zn, and Mg foams but Ti foams are unsuitable due to the high melting point temperature and reactivity. Conventional sintering of titanium alloy powders requires high temperatures in high vacuum for a long period of time. Wen and coworkers have fabricated titanium foams by using a Powder metallurgical process including space holder particles (Wen, Yamada et al. 2002). Densities of the titanium foams were approximately 50-65% which is close to cortical bone.

### **2.1.4. Electrical Discharge Compaction**

As sintering of titanium is difficult, new alternatives have been studied for porous titanium alloys. Electrical discharge compaction (EDC) has been used to fast sinter powders with rapid heating and pressure. Electrical energy is released suddenly with

discharging capacitors. Qiu and coworkers fabricated composite titanium dental implants with electro discharge compaction (Qiu, Dominici et al. 1997). Lee et al. reported that porous implants produced by EDC are biocompatible and allow rapid osseointegration (Lee, Park et al. 2000).

#### **2.1.5. Plastic mold techniques**

Molds are prepared from polyurethane type material foams and coated with metallic slurry. The polyurethane is removed by heating slowly and pressure is sometimes applied to keep the structure intact. After removing the molding foam, it is sintered. Molds can be in different shapes. Li et al. used polyurethane struts as a mold and coated them with a titanium slurry (Li, Wijn et al. 2006). After removing the polyurethane, the powder was sintered. The porosity of the porous titanium alloy was 88% with a compressive strength of 10 MPa.

#### **2.1.6. Wire Mesh**

Wires can be randomly put together to get meshes or they can be oriented to get woven structures. Naidu et al. developed orderly oriented wire mesh (OOWM) structures as an alternative to porous beads and fiber meshes (Naidu, Moulton et al. 1997). Wires are woven into a regular meshwork and pressure sintered to the surface. Mechanical pull out tests were done at 4 weeks, 8 weeks, and 12 weeks after implantation. OOWM was reported to be as effective as porous beads in bone ingrowths and stability.

#### **2.1.7. Vapor deposition**

A carbon skeleton was obtained from the thermosetting polymer foam, which has a repeating dodecahedron structure. Pore sizes and density of the polyurethane foam

changes the pore size and mechanical properties of the Trabecular Metal<sup>®</sup> as shown in Figure 1. The tantalum deposited into the carbon skeleton using chemical vapor deposition with 50 $\mu\text{m}$  coating thickness. Deposition thickness affects the pore size and mechanical properties. Textured microstructures are the result of this process due to the orientation during deposition and crystallographic growth. Average pore diameter was around 547  $\mu\text{m}$  with 75-80% homogenous porosity. The Trabecular Metal<sup>®</sup> was approved by the FDA in 1997 as a bone ingrowth material. Trabecular Metal<sup>®</sup> has been reported to have good mechanical properties with an elastic modulus of 3 GPa (Boby, Stackpool et al. 1999). This is reasonably similar to cancellous bone (0.1-1.5 GPa). In contrast, cortical bone has an elastic modulus of 12-18 GPa (Medlin, Charlebois et al. 2004).

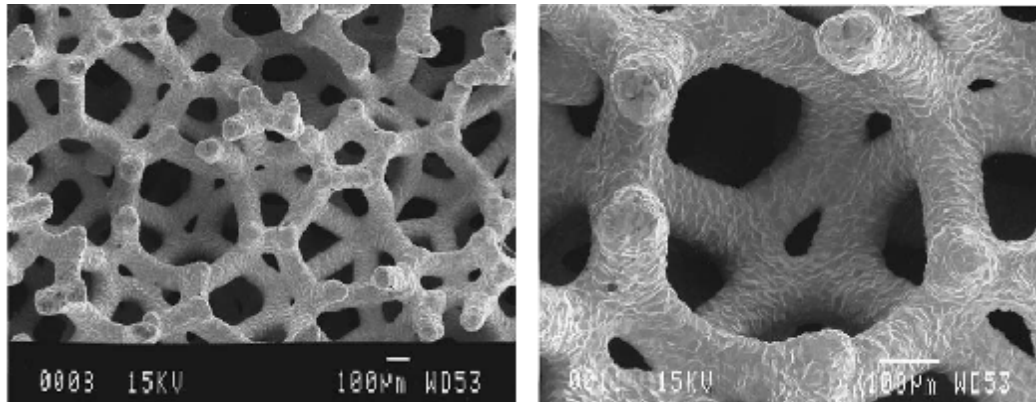


**Figure 1: Trabecular Metal (Zimmer, Inc, Warsaw, Ind previously Hedrocel, Implex Corp.), (Boby, Stackpool et al. 1999), Reprinted by permission from the author.**

Sandwich panels can be assembled from the metal foams using metal face sheets (Banhart 2000). Wadley and Fleck et al. reported another way for sheet forming of trusses and shell elements with periodic open cell pores (Wadley, Fleck et al. 2003). Low density metallic honeycomb cores were manufactured from corrugated sheets and bonded together by resistance welding as shown in Figure 2.

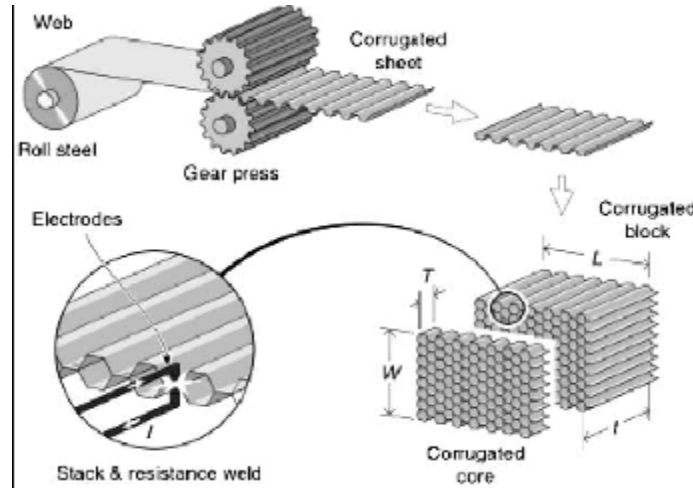


**Figure 2: Low relative density honeycomb core manufacturing (Wadley, Fleck et al. 2003), Reprinted by permission from Elsevier.**

### **2.1.8. Orientation with Magnetic field**

Preferred orientation induced by a magnetic field is applicable to ferromagnetic metal fibers, but there are limitations in controlling the structure. Chino et al. used a static magnetic field to control porous structures in a restricted way (Chino, Mabuchi et al. 2006). Ferromagnetic metal fibers were cut with chatter vibration cutting tools. A magnetic field was applied while filling the carbon die with fibers as shown in Figure 3. It was shown that fibers lined up parallel to the direction of a magnetic field, so oriented green compaction was made in the die. Higher collapse stress was observed with a magnetic field effect than with regular compaction.

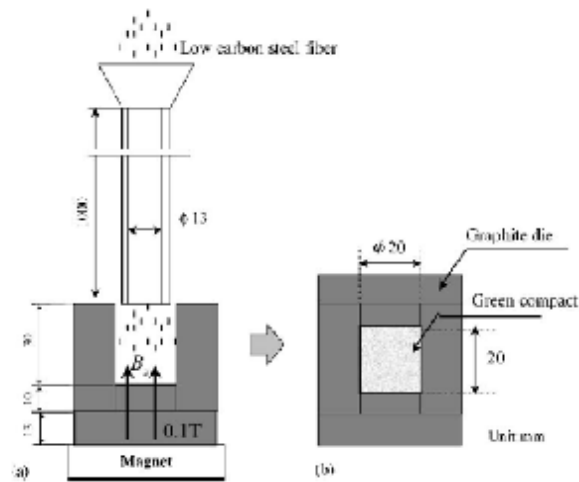


**Figure 3: Magnetic field applied while filling the cavity. Source: (Chino, Mabuchi et al. 2006) ,Reprinted by permission from Elsevier.**

### 2.1.9. Chemical Etching

Besides creating the porosity by controlling the process parameters, new methods have been studied to control the mesh geometries with the design. Intended surface structures have been designed and manufactured. Kusakabe et al. studied a new type of porous coating for hip prostheses called “multilayered mesh” and tested under weight-bearing conditions (Kusakabe, Sakamaki et al. 2004) as shown in Figure 4. Hydroxyapatite (HA)-coated multilayer meshes resulted in more bone ingrowth than the bead-coated implants.

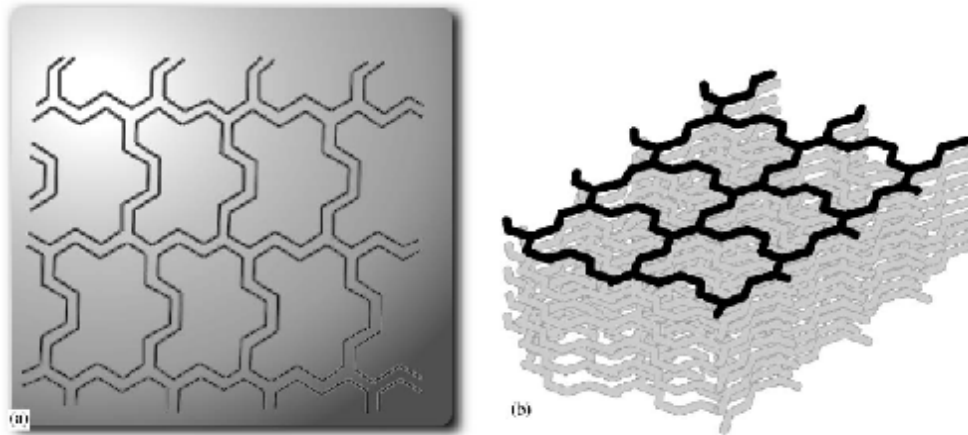


**Figure 4: Structure of the multilayered mesh surface. (a) Pattern design and (b) Laminations. Source: (Kusakabe, Sakamaki et al. 2004), Reprinted by permission from Elsevier.**

The multilayered structure provided a permanent bonding between bone ingrowths and the surface structure. A 3D pattern was obtained from 2D layer titanium meshes created by chemical etching. Ten layers of 100 $\mu$ m thick titanium 2D meshes were bonded by heat process at 900 $^{\circ}$ C. The porosity of the structure was around 80%. Hydroxyapatite was applied to the surface by thermal spraying at 3000 $^{\circ}$ C. Multilayers were heated to 650 $^{\circ}$ C in a vacuum furnace to release the residual stress. The HA coating did not alter the pores or the uniform distribution. The HA coating was added for increased chemical bonding to bone. A textured surface of multilayered mesh was thought to be required for a long lasting support. The multilayered structure was observed to be more resistive to shear forces and tensile forces than bead-coated implants (Bellemans 1999).

RP systems are other alternatives to building controlled mesh structures. Many different RP processes are available today to build dense metal parts. Direct metal fabrication processes are of interest to this work. It is also possible to use indirect metal fabrication methods to build 3D structures, but titanium alloys are reactive and it is

difficult to do investment casting with prototyped plastic molds. Focus will be on the direct fabrication for its efficiency and controlled properties. Some of the metal based systems are 3D welding, jet solidification, shape-deposition manufacturing, laser based systems, electron beam melting, spray metal, and 3D printing. The most popular systems are laser systems and different types of laser based systems have been developed. Some of them are given in Table 2.

**Table 2: Some of the companies related with laser fabrication process. Source: (Santos, Shiomi et al. 2006), reprinted by permission from Elsevier.**

Machines	Company	Process	Laser	Power
Sinterstation 2000/2500	DTM	DMLS	CO <sub>2</sub>	50 W
EOSINT 250	EOS	DMLS	CO <sub>2</sub>	200 W
EOSINT 270	EOS	DMLS	Ytterbium fibre laser	200 W
LUMEX 25C	MATSUURA	SLM	Pulsed CO <sub>2</sub>	500 W
TrumaForm LF 250	TRUMPF	SLM	Disk laser	250 W
Realizer	MCP	SLM	Nd:YAG	100 W
Lasform	Aeromet	3D laser cladding	CO <sub>2</sub>	10-18 kW
LENS 850	Optomec	3D laser cladding	Nd:YAG	1kW
Trumaform DMD 505	TRUMPF	3D laser cladding	CO <sub>2</sub>	2-6kW

### 2.1.10. Selective laser sintering

A roller mechanism is used to spread the powder over the build platform and each layer is selectively bonded by the CO<sub>2</sub> laser beam. The fabrication platform is lowered, new powder is delivered, and the process repeats until the build is finished (Kruth, Wang et al. 2003). The metal powder is mixed with a polymeric binder, so the laser energy binds the particles as a green part, which needs secondary processing of sintering and infiltration. When sintering is completed, the resulting part is porous and infiltration with a metallic or polymeric material may be required.

### 2.1.11. Direct metal laser sintering (DMLS)

DMLS uses a powerful CO<sub>2</sub> laser of 200W and directly sinters the metal powder. Secondary sintering or infiltration is not needed with this process. Examples of the 3D

mesh structures from the direct metal laser sintering are given in the Figure 5. Three-dimensional mesh structures in stainless steel and in cobalt-chromium were built with DSLM technology and resulted in nearly 90% reduction in weight. It is also applied in dental applications for low volume production of dental caps.

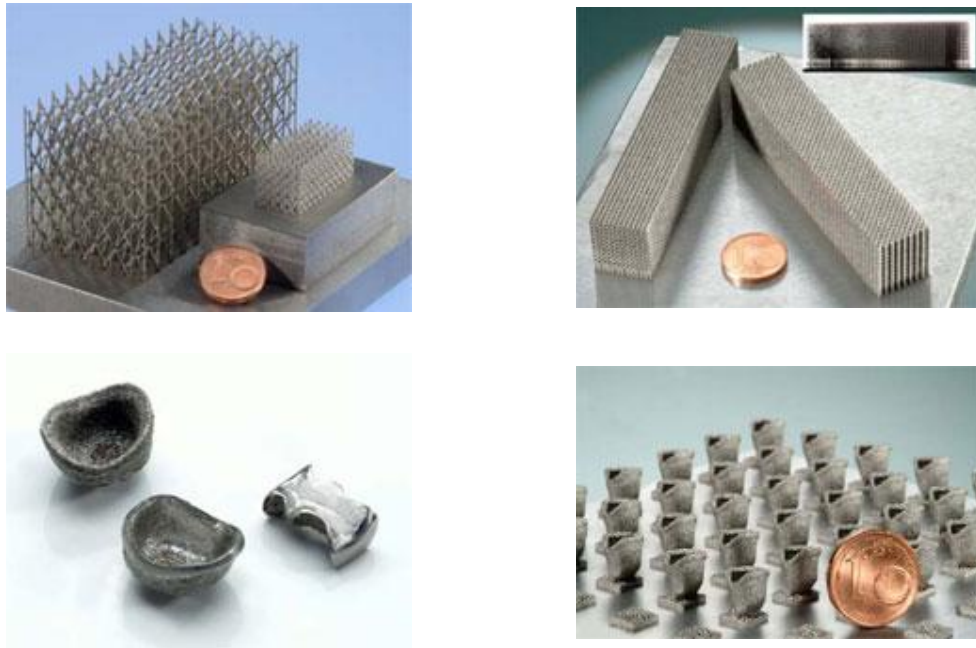


**Figure 5: 3D mesh structures in stainless steel and in cobalt-chrome** Source: [http://www.mcp-group.com/rpt/rpttslm\\_1.html](http://www.mcp-group.com/rpt/rpttslm_1.html) reprinted by permission from the MCP-group.com

EOS GmbH (Munich, Germany) has a machine called the EOSINT M 270. It has a Yb-fibre laser of 200W with precision optics. The build speed (material-dependent) is given from 2 to 20mm<sup>3</sup>/s and the layer thickness is from 0.0254 to 0.1 mm. Direct part and direct tool applications have been done for industrial applications.

### **2.1.12. Laser Engineered Net Shaping**

A high power laser, 500-1000W, is used to melt the metal powder. The laser beam and the powder are delivered at the same head coaxially as shown in Figure 6. Shielding

gas may also be delivered through the same head while melting the powder. The head is moved in the Z direction instead of moving the platform. Sandia National Laboratory developed the laser engineered net shaping (LENS<sup>®</sup>). It is primarily useful for repair operations, because it does not use a powder bed as is shown in the figure below. It has other advantages such as hybrid manufacturing ([www.optomec.com](http://www.optomec.com)). It is possible to add wear resistant materials or other types of materials locally. LENS<sup>®1</sup> has been commercialized through OPTOMECC (Albuquerque, NM) and different powder materials have been developed for this process.

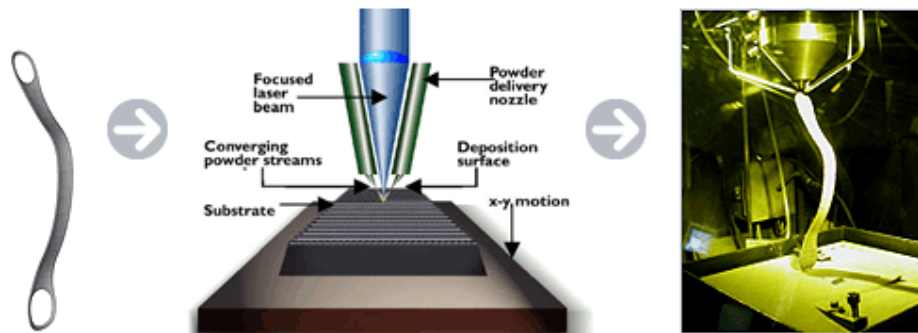


**Figure 6: OPTOMECC ,medical device fabrication. Source: <http://www.optomec.com>, LENS<sup>®</sup>, reprinted by permission from Optomecc.**

Wu and Mei have manufactured Ti alloys and SiAl alloy onto Ti-6Al-4V alloy (Wu and Mei 2003). The laser power ranged from 180 to 1200W with a scanning rate of 150 to 1000 mm/min. Test structures were built with overhanging features and thin sections as shown in Figure 7. Ti-6Al-4V alloy has been reported to have a narrow window for the processing parameters, and it is easy to form a porous microstructure.

---

<sup>1</sup> LENS is a registered trademark of Sandia National Laboratories

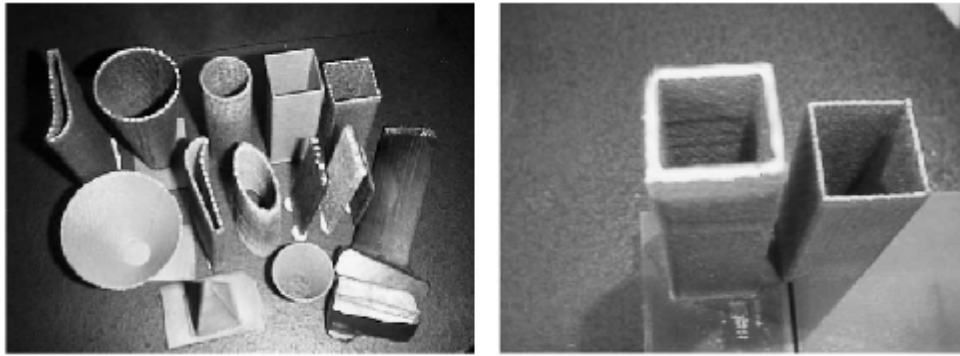


**Figure 7: Parts from the LENS process. Source: (Wu and Mei 2003) reprinted by permission from Elsevier.**

### **2.1.13.    Microsintering**

Small scale structures were built with the microsintering process using layer resolutions at the micro level. 3D-Micromac AG, (Chemnitz, Germany) offers microsintering technology to fabricate freeform micro parts. Micrometer resolution is possible with a surface roughness of  $1.5\mu\text{m}$ . The density of the micro parts made from powder mixtures is around 95%. Haferkamp et al. developed a microsintering system with a density controlled deposition mechanism as shown in Figure 8 (Haferkamp, Ostendorf et al. 2004). The layer thickness has been reported to be in the range of 10-100 $\mu\text{m}$ . The minimum spot size of the shaped laser beam was around 20 $\mu\text{m}$ .

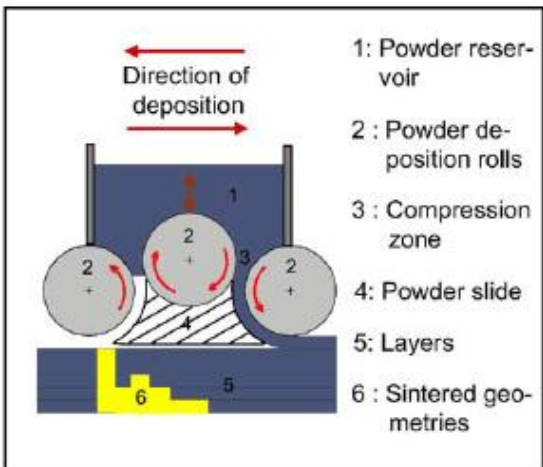


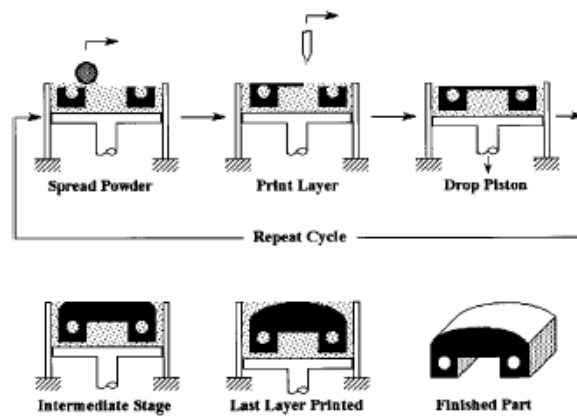
**Figure 8: Powder deposition with adjustable layer thickness and density. Source: (Haferkamp, Ostendorf et al. 2004) reprinted by permission from Elsevier.**

**2.1.14. 3D printing**

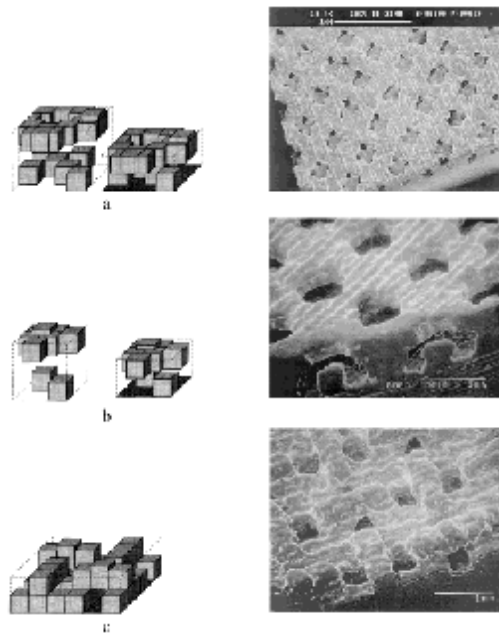
Recently, 3D printing has been used to produce porous implants with controlled size, shape and distribution of porosity. Three-dimensional printing is a solid freeform fabrication technique that can generate complex geometries from different materials layer by layer as seen in

Figure 9. Melican et al. used 3D printing to prepare the molds with a dimensional resolution of 175 μm (Melican, Zimmerman et al. 2001). Bone ingrowth surfaces were produced from the textured surfaces of the molds and three experimental textures were fabricated with the surface layer and the deep layer at different porosity ratios. Surfaces of commercially sintered beaded coatings were used as controls. A canine transcortical implant model was used in the study. Mechanical push-out tests were used to test the interfacial shear strength at periods of 6, 12, and 26 weeks. Three textured surfaces were evaluated and reported to have significantly higher shear strength at 26 weeks than the controls. The relation between bone ingrowth and the level of porosity was discussed for high shear strength.

Curodeau et al. produced sub-millimeter surface textures with overhangs and undercut geometries as bone ingrowth surfaces for implants (Curodeau, Sachs et al. 2000). Three-dimensional printing, as shown in Figure 10, is used for ceramic molds of alumina powder with silica binder. Surfaces were textured with 5 layers of different geometries with an overall porosity from 30 to 70%. Features as small as 350 x 350x 200  $\mu\text{m}$  were successfully cast (Figure 10). Removal of the powder from the ceramic molds and the required pressure to fill these small features with metal limited the possible feature sizes.



**Figure 9: 3D printer (Curodeau, Sachs et al. 2000) , Copyright © 2000. Reprinted by permission of John Wiley & Sons, Inc.**



**Figure 10 : Different surface texture geometries and surface image of the castings (Curodeau, Sachs et al. 2000) , Copyright © 2000. Reprinted by permission of John Wiley & Sons, Inc.**

### **2.1.15. 3D fiber deposition**

Three dimensional metal structures can be created through extrusion. The metal slurry can be prepared at different concentrations and compositions to adjust the viscosity and the cured density of the extruded line. Li et al. prepared a porous Ti6Al4V scaffold by extruding a titanium slurry (Li, Wijn et al. 2006). The external shape and the interconnections were controlled while building the part. Ti6Al4V powder was mixed with methylcellulose and stearic acid (34 vol%). The slurry was stirred for 1hr and then extruded using a syringe under pressure. The deposited fibers were sintered in a high vacuum furnace while applying heat up to 1250 °C.

### **2.1.16. Electron Beam Melting**

The inventors Ralf and Ove Larson developed an early version of these RP machines. In 1993, Ralf Larson applied for a patent about welding the metal powder

layers together with an electron beam<sup>2</sup>. The development of this method was done in collaboration with Chalmers University of Technology in Gothenburg, Sweden. Arcam (Arcam AB, Sweden) was founded after the approval of the patent. Now, Arcam is offering this relatively new electron beam melting technology for cutting edge applications.

Arcam's electron beam melting technology is now on the market with its "CAD to Metal" system to produce fully dense metal parts. It uses a 4.8kW electron beam gun to melt the metal powder with the electrons' kinetic energy. The electron beam gun is fixed on top of the vacuum chamber and it has a cathode, an anode, and an electromagnetic focusing unit. Emitted electrons from a filament are accelerated towards the build substrate and controlled with the magnetic fields. The beam focuses on specific regions at scanning speeds up to 1000m/s as shown in Figure 11. The current commercial models are the S12 and the A2.

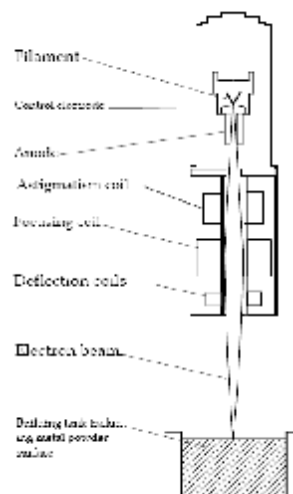


**Figure 11: Sketch illustrated the Beam control system Source: EBM manual**

---

<sup>2</sup> [http://www.speedpart.se/about\\_history.html](http://www.speedpart.se/about_history.html)

Three-dimensional parts are sliced into 2D layers using special software, similar to other RP file processing systems. The layers are melted one at the time and then new powder is delivered at a predetermined thickness. The layer is preheated for initial sintering and attachment of the powder to the previous layer, and also to help to build parts with less thermal internal stresses (Cormier, Harrysson et al. 2004). The current layer is melted after completing the preheating steps and the support structure. After melting the current layer, a new layer of metal powder is added over the previous one, and the procedure is repeated. The part is melted slice by slice similar to the other RP processes as shown in Figure 12. The unmelted powder acts as a support for the part during the fabrication and is easily removed and reused. Electron beam melting in vacuum has many advantages over laser sintering systems. It provides high power efficiency, good material properties, and laser systems are known to have problems with reflectivity which decreases the power efficiency. The laser lifetime is limited, while the electron beam is relatively free except for the cost of the filaments. The melting process is done under vacuum, which eliminates impurities, eliminates oxidation of the molten material, and yields higher strengths of the materials. The vacuum is costly to maintain but the vacuum tank is also designed to block any harmful gamma rays. Melting of reactive materials like titanium can only be done under vacuum and the processing also prevents oxidation of the unused powder in the machine. The mechanical properties of the resulting parts are comparable to wrought titanium and better than cast titanium (Arcam, Sweden). The control system of the electron beam does not include any optics or moving mirrors as used in the laser based control system. The lasers based systems also need to match the wavelength for different materials to achieve maximum efficiency. The

electrical-to-optical conversion efficiency of a high-power diode laser unit is around 20 % with a maximum of 50 % (Lin 2000). However, laser based systems have higher accuracy and better surface finish compare to the EBM parts.

In the EBM system, parts can be set up with different processing parameters, which make it possible to build light structures and solid sections at the same time. Contours and hatches are used to scan the part for preheating, post heating and melting. The preheating is important for the attachment of the newly spread powder to the previous layer, which will increase the electrical and thermal conductivity. Invisible supports are created by further sintering the powder under the down-facing regions. The scan speed, power settings, hatch properties, and heating parameters can be changed in the EBM control system. The control of the process parameters in the EBM machine is similar to the parameter controls in laser based systems (Mazunder, Schifferer et al. 1999). Modeling of the EBM process for melting of solid metals has been reported in the literature (Vutova and Mladenov 1999). There are also solid-interaction models based on physics but there is no model for the electron beam interaction with metal powders as used in free form fabrication systems. One of the important additions to the EBM system is the wafer supports. This is similar to the break-away supports used in stereolithography systems and consists of thin porous walls that connect the inclined surfaces to the platform.

Different metal powders can be used in the machine after the process parameter development is completed. Powder size, conductivity, and vaporization are important factors in the selection of the powder. H13 tool steel was the only material available from ARCAM when the EBM machine was introduced in 2003. Currently pure titanium,

Ti6Al4V, Ti6Al4V ELI, and CoCrMo are commercially available for the EBM system through Arcam (ARCAM, Sweden).

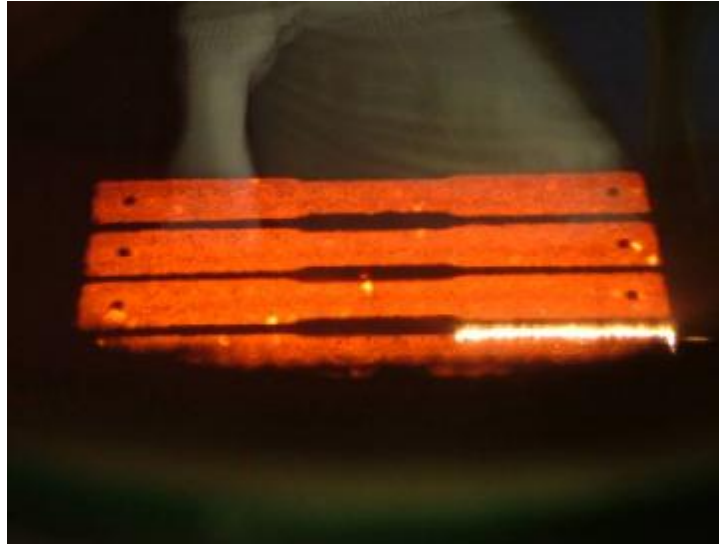


**Figure 12 : Electron beam is melting the current layer (CoCr test parts in EBM S12)**



**Figure 13: EBM build platform with sintered powder surrounding the actual parts.**

The EBM has been used to manufacture custom knee implants and custom bone plates (Harrysson, Cormier et al. 2003; Cormier, Harrysson et al. 2004). The custom bone plates were designed based on patient specific image data and fabricated using the EBM. Finishing of the surfaces was necessary and post processing was done using a CNC

milling machine. Implants with metal mesh coating have recently been manufactured using the EBM system. New materials have also been processed after developing new processing parameters. GRCop-84, developed at the NASA Glenn Research Center for use in regeneratively cooled rocket engines<sup>3</sup>, has recently been used to build test parts. D. Cormier et al., 2004, have also produced thin walled Ti6Al4V components and characterized the material properties as compared to bulky structures (Cormier, West et al. 2004).

Electron beams are also used for other applications areas and some of them were developed before the RP methods, such as melting metal at high purity, welding, curing, lithography, sterilization, high powered beam applications, and film deposition. Baris et al. studied the coatings of TiN, TiC, TiB<sub>2</sub>, and  $\delta$ -MoB powders on a titanium base using an accelerated electron beam at the nuclear physics lab (Baris, Golkovsky et al. 2000). The experimental settings were 1.4MeV for the electron beam energy, 20 to 30 mA for the beam current, and a beam velocity of  $10^3 \text{ m.s}^{-1}$ . Sterilization is one of the application areas of electron beam beyond the free form forming techniques. With the increased focus on the electron beam, the shortest sterilization times can be achieved. Calhoun et al. reported that the overall processing time including transportation is around 5 to 7 minutes (Calhoun, Allen et al. 1997).

---

<sup>3</sup> D.L. Ellis, D.J. Keller. Thermophysical Properties of GRCop-84. NASA CR2000-210055, 2000. <http://gltrs.grc.nasa.gov>

## **2.2. Mechanical Behavior of Metallic Foams**

Researchers have been interested in foam materials and their properties for a long time. Recent work about electrical, mechanical, and thermal properties of the foam materials helped to understand metal foams and develop new processes for specific applications (Ashby, Evans et al. 2000; Banhart 2000; Gibson 2000). Many studies have been done on stochastic metallic foams and some examples are given here. Harte et al. investigated the fatigue strength of the open cell Al 6101-T6 foam in cyclic four point bend (Harte, Fleck et al. 2001). Analytical models were developed to predict the fatigue strength for each of the different failure modes. The fatigue strength and the failure mode were displayed in a design map as a function of beam geometry.

Nieh studied compressive properties of open cell 6101 aluminum foams with different densities and morphologies (Nieh, Higashi et al. 2000). It is reported that the modulus and the yield strengths of the foams were affected by changes in the density. Aluminum foams were fabricated by using a directional solidification technique. The compression stress-strain curves showed a general three stage behavior: elastic, nearly-perfect plastic, and densification as shown in Figure 14. The effect of cell size was observed to be negligible while keeping the density the same but the cell shape has a significant influence. Models were developed to show the effect of cell shape and size in rectangular unit cells.

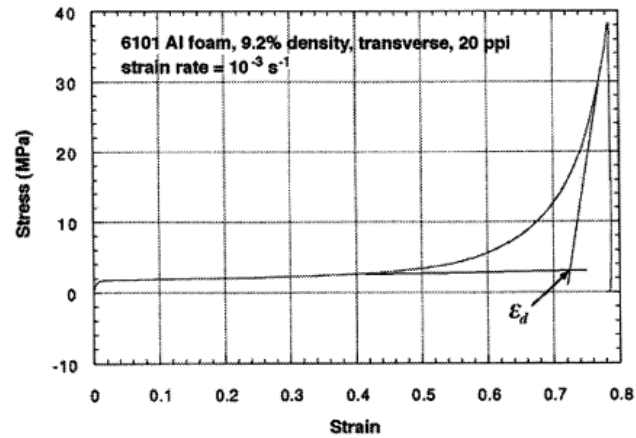


Figure 14: Compressive stress-strain curve for 6101 Al foam (9.2% density), (Nieh, Higashi et al. 2000) reprinted by permission from Elsevier.

Non-stochastic structures or lattice structures are similar to foam materials and they represent the cellular structures. Mechanical models describe metal foams as bending dominated or stretch dominated structures (Ashby 2006). The type of the structure is of importance when deriving the equations. Cellular structures with closed cells or open cells can show bending dominated behaviors. Maxwell, who is famous in electromagnetism and other fields, showed that the stability criterion describes when bending or stretching happens in cells in a simple formulation (Maxwell 1864).

$$M=b-2j+3 \quad (1)$$

where  $b$  is the number of struts and  $j$  is the number of nodes in 2D. The equation for 3D cases is given below.

$$M=b-3j+6 \quad (2)$$

Stretch dominated structures will have  $M \geq 0$  and bending dominated structures will have  $M < 0$ . A simple schematic shows the difference of mechanism type structures, stiff structures and over-constrained structures in Figure 15.

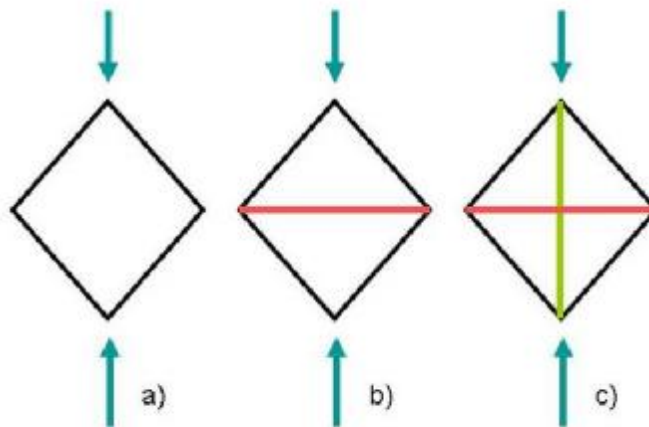


**Figure 15: a)  $M < 0$  and it is a bending mechanism b)  $M = 0$  and It is stiff with horizontal beam in tension c)  $M > 0$  and it is over-constrained.**

Ashby stated that space filling polyhedral cells in 3D do not have structures with  $M \geq 0$ . However, space-filling combinations of cells have a rigid framework such as the tetrahedron and the octahedron structures. In metal foams, structures are modeled as space filling structures and the same unit cell repeats for the entire material volume (Ashby 2006).

Cell topology and connections define the structure type, and the number of connecting beams at each node defines the structure mechanism. Their properties are related to the material they are made of, cell topology, shape, and relative density. Different scaling laws for mechanical, thermal, and electrical properties have been derived for bending dominated and stretch dominated structures based on the relative density. Relative density of the structure was defined in relation to the edge thickness and cell size. The materials were assumed to be linear and the equations were derived for plastic yielding, buckling, and fracture (Gibson 2000). Gibson reviewed the elastic modulus, strength, yield criterion, creep, and fatigue of metallic foams in his article

(Gibson 2000). It is stated generally that mechanical properties are independent of the cell size. Bulk modulus and foam modulus were given as proportional to the square of the relative density and multiplied by a constant which depends on the structure. In open cell foams, the modulus is calculated based on the dimensional analysis of edge bending and given as  $\frac{E^*}{E_s} = C_1 \left(\frac{\rho^*}{\rho_s}\right)^2$ . In closed foams, bending and stretching of the faces are

represented as  $\frac{E^*}{E_s} = C_1 \left(\frac{\rho^*}{\rho_s}\right)^2 + C_2 \left(\frac{\rho^*}{\rho_s}\right)$ , where  $\rho^*$  is the density of the foam,  $\rho_s$  is the

density of the solid of which it is made. First term represents the bending of the cell edges and second term accounts for stretching of the faces. Other relations were also given for yield strength, yield criteria and creep.

Metal foams were also modeled as cellular lattice type structures, because the skins are very thin and they fail at small loads (Ashby 2006). A generic stress-strain curve of a cellular solid shows yielding point, plateau stress, and densification is shown in Figure 16. This behavior is mostly attributable to the plastic failure. Fractures in the structure break the lattice connections and cause catastrophic failure.

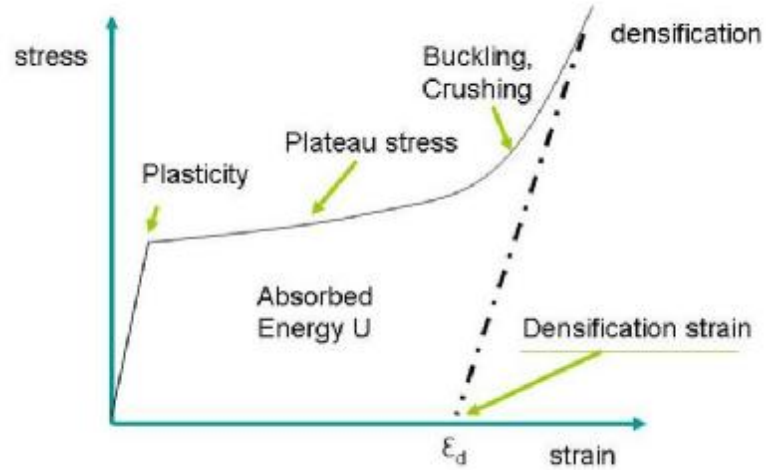


**Figure 16: A stress-strain curve of a cellular solid with typical densification.**

Crushing will not show densification because it will not have connections to limit the movement of other node points and prevent further bending or buckling. Examples about that are given in this section for initial lattice structures. Defects on the lattice or crack initiation points represent stochastic failure properties. It is also important to say that other types of failures can happen at the same time besides the main failure type.

In the literature, lattice structures have been studied for tissue engineering applications to modify the unit cells for a specific porosity, pore size, and material properties (Hollister, Maddox et al. 2002; Lin, Kikuchi et al. 2004; Hollister 2005). Related fabrication methods and topology optimization based design methods for these applications will be discussed in the following chapter. Structure unit libraries and related procedures have been discussed in the literature (Fang, Starly et al. 2005; Sun, Starly et al. 2005; Wettergreen, Bucklen et al. 2005). Image based methods were mostly used in their studies. Representative unit cells were optimized according to the specific constraints, and then replicated features from the unit cells are merged together with the

implant region or the scaffold region. Similar unit cell based replications and Boolean operations were used in this study to create the implant designs with cellular structures.

There are limitations in layered manufacturing processes in terms of feature sizes, layer connectivity, material choices, processing parameter flexibility in different features, and complexity of the build. The layered Electron Beam Melting process has limitations in terms of structure connectivity, dimensions, and type of features possible without extra sintering or solid supports. In the next sections, lattice structures with different cellular designs are discussed and their properties are given from different tests. Some examples of EBM based cellular manufacturing are also given in an optimization context. The primary reason for these structures are medical applications, so details about tailoring structures to specific bone properties are also given below.

Several mesh configurations were tested in the preliminary stages of this research. Structures with holes were investigated first, but they did not show much difference in structural elastic modulus compared to solid titanium structures, see Figure 17. Hip stems based on this design were also manufactured and tested, Figure 18.

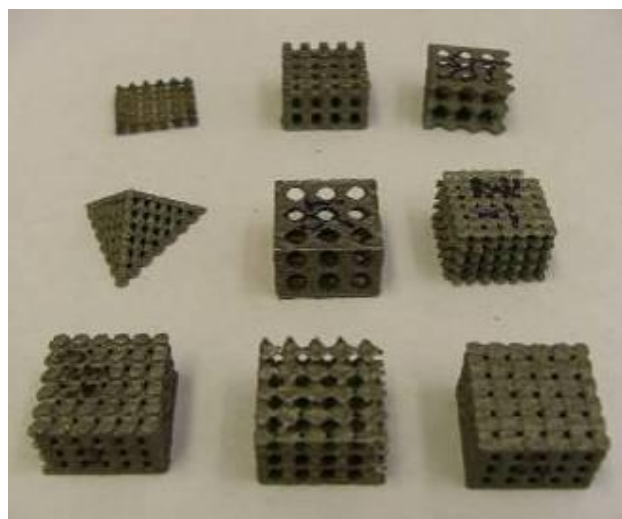


**Figure 17: Structures with straight holes were manufactured using EBM.**



**Figure 18: Less stiff implant designed with straight holes.**

Initial mesh structure designs based on repeating features are given below in Figure 19, Figure 20, and Figure 21.

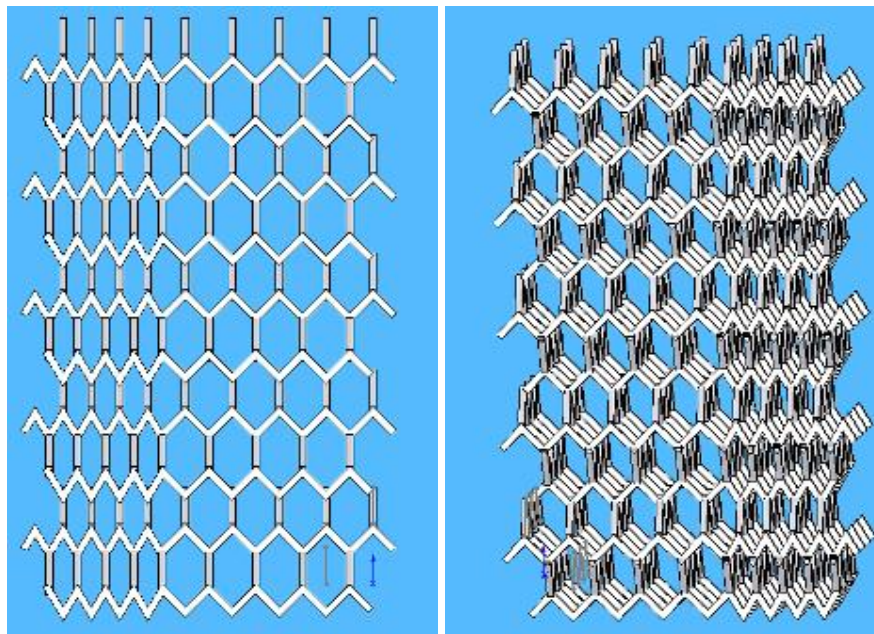


**Figure 19: Edges of Honeycomb are intertwined to other layer in variable porosity**

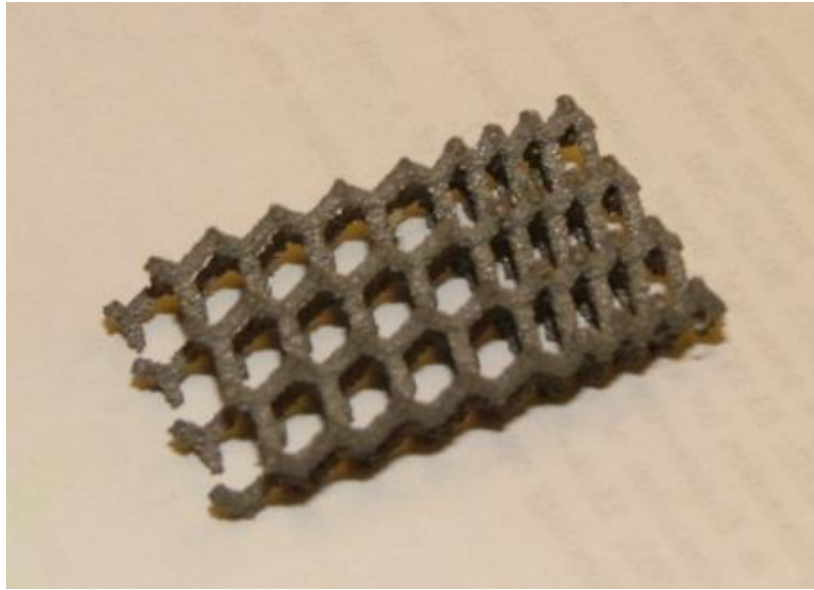


**Figure 20: Titanium solid model of the honeycomb design made with EBM.**

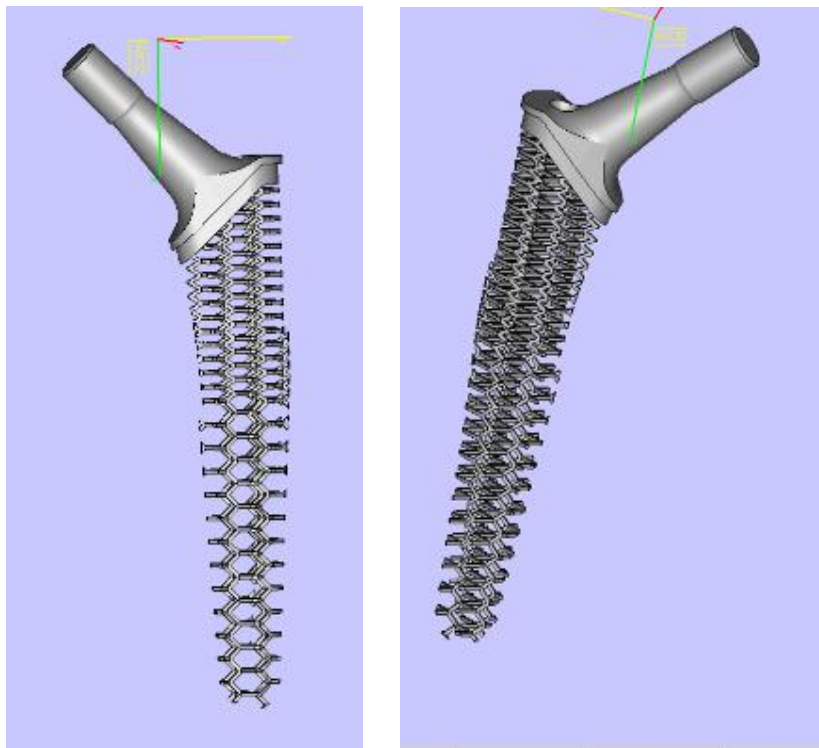


**Figure 21: Flexible implant example from different views.**

### 2.3. Initial hexagon meshes

Arcam developed and provided the basic process parameters for producing lattice structures in Ti-6Al-4V. The information was used as a starting point to investigate the process capabilities for lattice structures. The lattice structures were designed using Solidworks™; commercially available solid modeling software. It was observed that the cross sectional area assigned to the thin beams of the lattice in the CAD-software varied from the actual part produced on the EBM system. The first experiment used the original lattice design with varying cross sectional diameter of the beam elements (0.5 mm, 0.75 mm, and 1.0 mm). The angle at which a beam is built with respect to the XY plane (build plane), the thickness of the beam, and the layer thickness of the thin structures are of high importance due to the layered fabrication approach. If the build angle is too low and the individual beams are thin or the layers are too thick, then there will be a very small overlap between the adjacent layers. Non-stochastic structures with beams built at an angle from 10° to 80° to the build plane were designed and fabricated in order to understand the influence of the beam angle on beam quality.

During the initial experimentations, it was observed that lattices whose struts were oriented at an angle of less than 20° with respect to the build plane had little or no structural integrity for small cross sections. Figure 22 illustrates the problem. The default layer thickness with the EBM process is 0.1 mm. At this layer thickness, it is clear that continuity between the layers becomes a problem as the strut angle relative to the built plate decreases for small cross sections. The overlapping distance between adjacent 0.1 mm thick layers can be expressed as  $L_1 - L_2$ , where  $L_1 = T/\sin(\alpha)$ , where T is the beam

thickness ,  $L_2 = 0.1\text{mm}/\tan(\alpha)$ ,  $T$  is the strut thickness, and  $\alpha$  is the angle of the strut with the build plane.

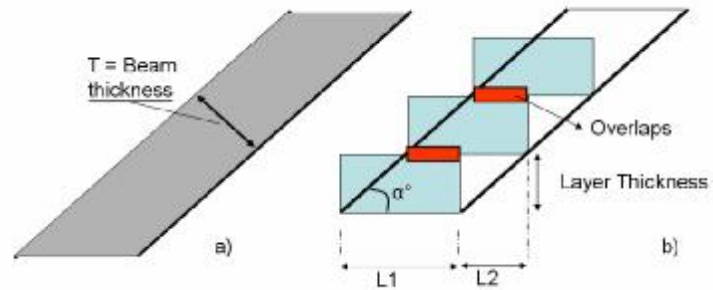


**Figure 22:** a) beam thickness is shown before slicing of the beam b) Overlaps, defined as  $L1-L2$ , between successive layers are shown with the related parameters.

Figure 23 shows a relatively good strut at left and a poor strut at right. Figure 24 show a relatively rough struts at low angles (top row), whereas it shows thicker beams at high angles with better connectivity (bottom row). These micrographs help to illustrate that the strut quality is sensitive to the build angle and melting parameters. More information is given about the effect of the melting parameters and changes in meshes properties in the next sections.

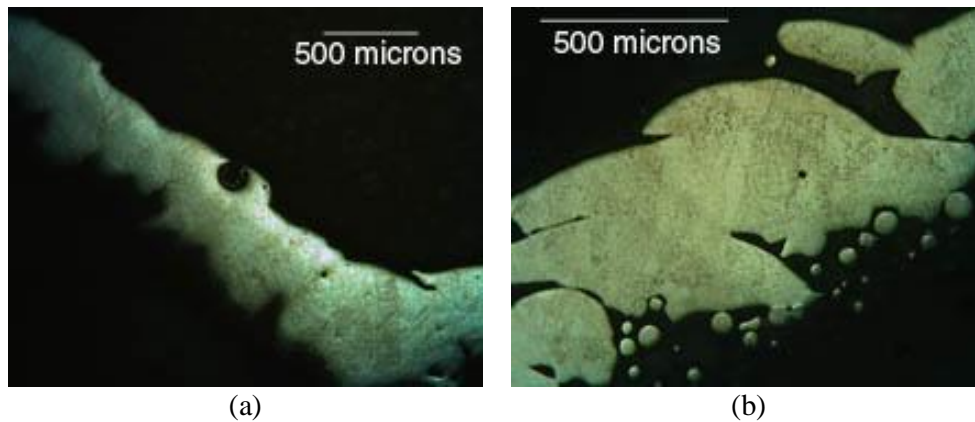


**Figure 23:** Close up view of Strut Qualities from earlier samples

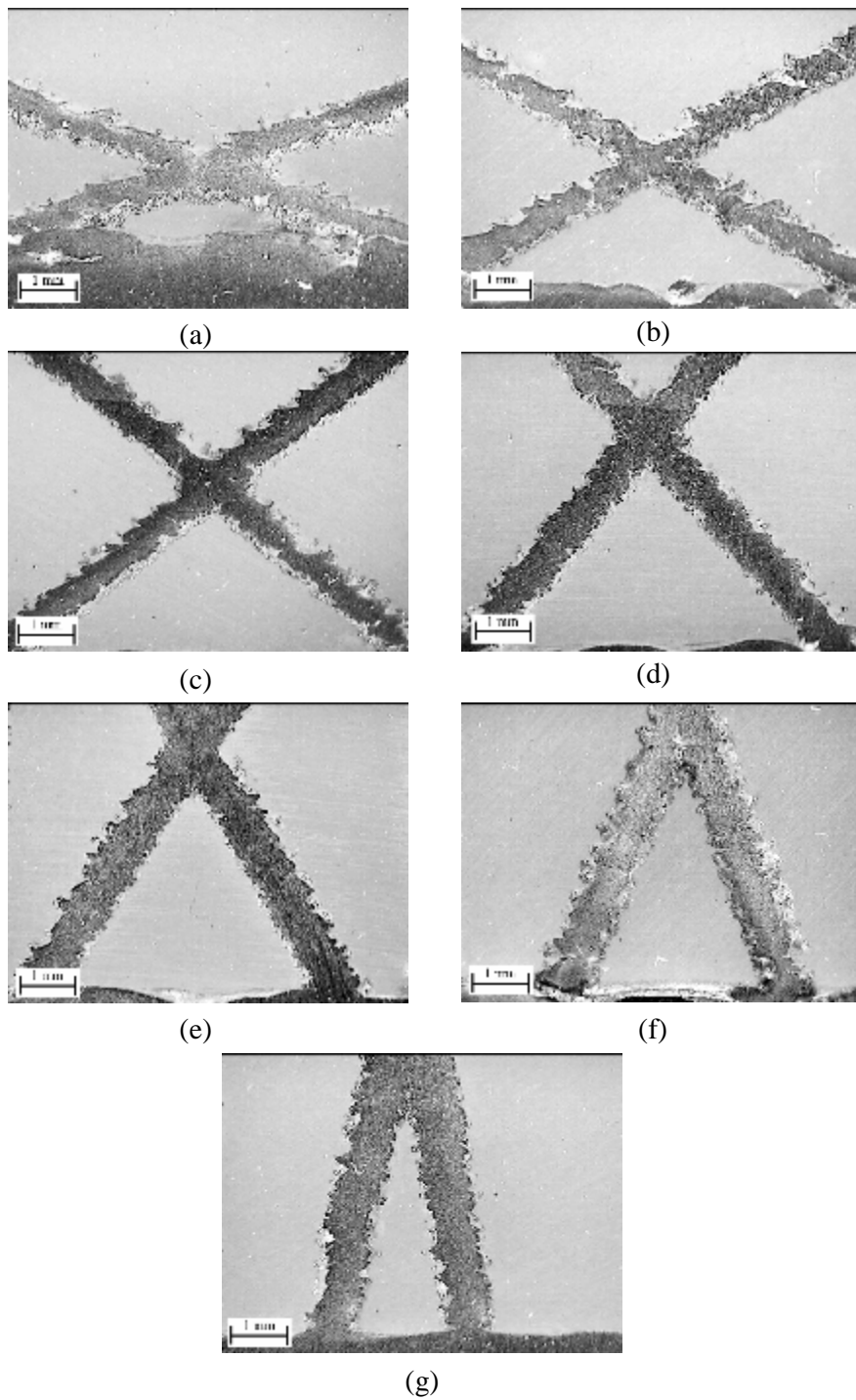


**Figure 24: Range of Strut Qualities for same beam melting parameters at same micrograph scale a) 20°, b) 30°, c) 40°, d) 50°, e) 60°, f) 70°, g) 80° angle with respect to XY plane**

From the process capability study it was decided that the struts should be modeled with a 0.7 mm beam thickness and a minimum angle of 20° with respect to the build plane in order to achieve good interlayer integrity. Using these parameters, a wide variety of non-stochastic cell structures were designed in SolidWorks and fabricated on the electron beam melting machine for mechanical testing. The non-stochastic cell structures were designed as cubes for crush testing and as beams for flexural testing. However, the material properties presented in the remainder of this section pertain to the non-stochastic structures with hexagonal unit cells shown in Figure 25.

### **2.3.1. Design and Fabrication of Structures**

For compression and flexural testing; cubes and beams with hexagonal unit cells were designed with different relative densities using 4, 5, and 6 mm unit cells (see Figure 25 ). The cubes were 25 mm x 25 mm x 25 mm and the beams had a length of 192 mm and 18.5 mm, 23 mm or 27 mm cross section for the different cell sizes. A strut diameter of 0.7 mm was used with a strut angle of 30 degrees, as described in the previous section. Lattice structures have repeating beams that have the same angle with the build platform and equal lengths. The beams have a square profile instead of a round cross section, as it helps to reduce the STL file size. Due to a close to circular weld pool during melting, the thin beams have an approximately circular cross section. STL files were exported from SolidWorks (SolidWorks Corporation, USA) and Magics (Materialise, Belgium) was used to prepare the build files for fabrication on the Arcam EBM S12 (Arcam, Sweden). Slicing of the structures was done at 0.1 mm layer thickness. A steel build substrate was heated to 750°C before the first layer of Ti-6Al-4V powder was melted using the process

conditions previously described. After the completion of each build the build chamber was cooled using Helium gas.

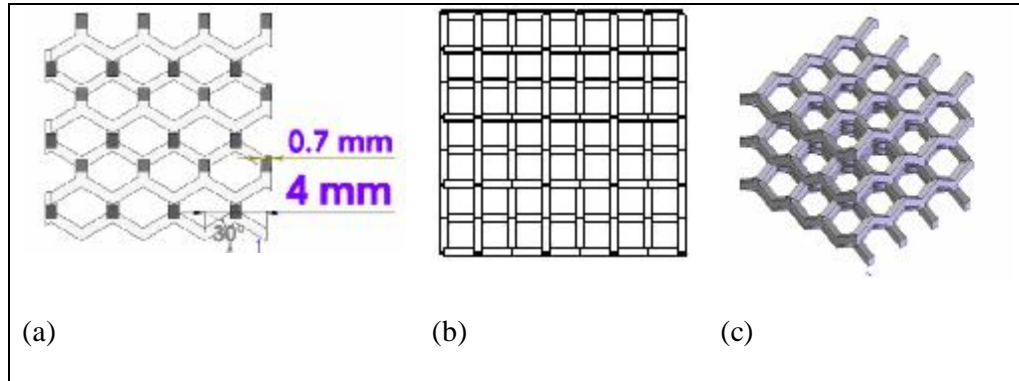


**Figure 25: a) Top view shows 0.7mm beam thickness, 4mm cell size, and build angle of 30° b) Front view ,c) Isometric View of Hexagonal Lattice Structure**

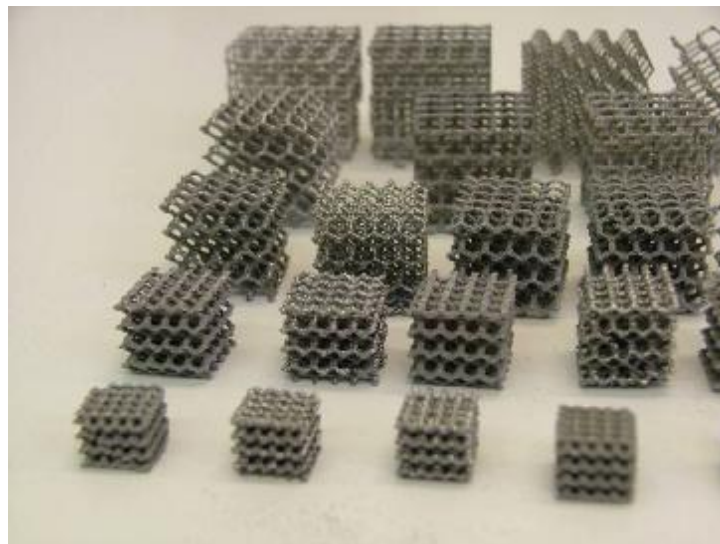


**Figure 26: Compression Specimens with 2mm (not tested),3mm (not tested),4 mm, 5 mm, and 6 mm Unit Cell Dimensions.**

### **2.3.2. Compression Test Procedure**

Material testing was conducted using an ATS 1605C universal tester. The specimens were compressed between steel plates at the rate of 5 mm/min. Number of cells on each side was more than 4. Sample size was three for compression testing. Three

specimens of each size were compressed in the build direction named XY in the testing protocols. Two specimens of each size were compressed in the perpendicular direction named Z in the testing protocols as seen in Figure 27. Each specimen was loaded until failure and the failure mode was recorded using the crosshead displacements. The compressive strength was calculated based on actual peak load for each specimen. The elastic modulus was calculated using the load-displacement data from the crosshead displacements.

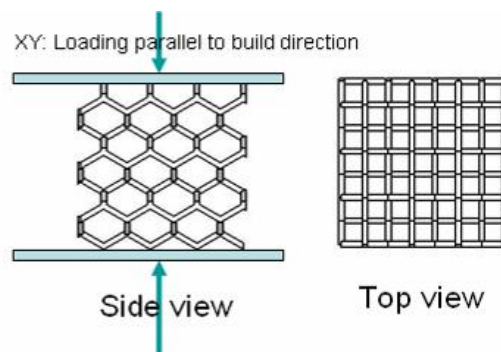


**Figure 27:** Compression test was done using parallels at each face for 4mm, 5mm and 6mm cell sizes

### **2.3.3. Flexural Test Procedure**

Three-point bend testing was conducted using the ATS 1605C universal tester with a load span of 177.8 mm. The length of the bending specimens was approximately 190 mm. The length to thickness ratio was approximately ten for all bending specimens. Sample size was more than 7 for each cell size. The flexural modulus was calculated according to the head-displacement reading from the bend tests. Specimens were tested in the direction parallel to the build direction.

Head displacements were used to calculate the flexural modulus based on the equation

$$E = \frac{(P/y)L^3}{48I}$$

, where  $E$  is modulus (MPa),  $P$  is load (N),  $y$  is deflection (mm),  $L$  is loading span (mm), and  $I$  is the bulk cross sectional moment of inertia ( $\text{mm}^4$ ).  $E$  was calculated for each sample. Each specimen's weight and cross section were used in the relative density calculation. Testing data was used to derive scaling equations for this structure for further references. Relative density was calculated based on the density of the structure over the solid material density. Density of the structures was calculated using the bounding box dimensions of the structure.

## **2.3.4. Experimental results**

### **2.3.4.1. Compression Tests**

Figure 26 shows a variety of non-stochastic cellular structures that were built in a single run on the EBM machine. The same hexagonal cell geometry was used in each case, but replications of structures having 4 mm, 5 mm, and 6 mm unit cell dimensions were built.

Figure 28 shows compression test results for five specimens with 4-mm unit cell dimensions. The XY1, XY2, and XY3 specimens were compressed in a direction parallel to the build direction see Figure 27. The Z1 and Z2 specimens were compressed perpendicular to the build direction. As can be seen from the data, parts loaded parallel to the build direction were stiffer and stronger, but required less work to failure. This trend was also observed for the 5-mm and 6-mm unit cell structures as seen in Figure 29 and Figure 30. Related results and strength/density ratios are given in Table 3.

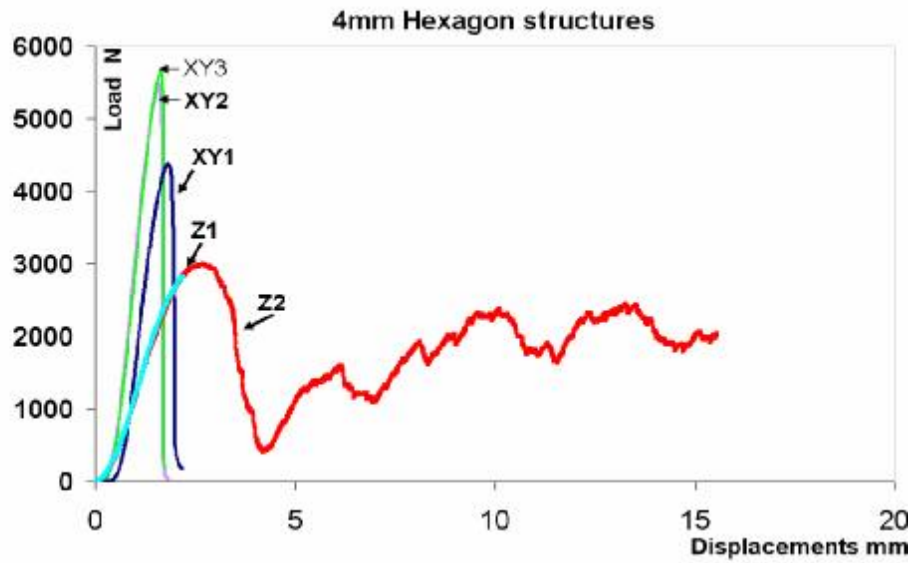


Figure 28: Compression Test Results for 4mm structures with maximum loading up to 5500N

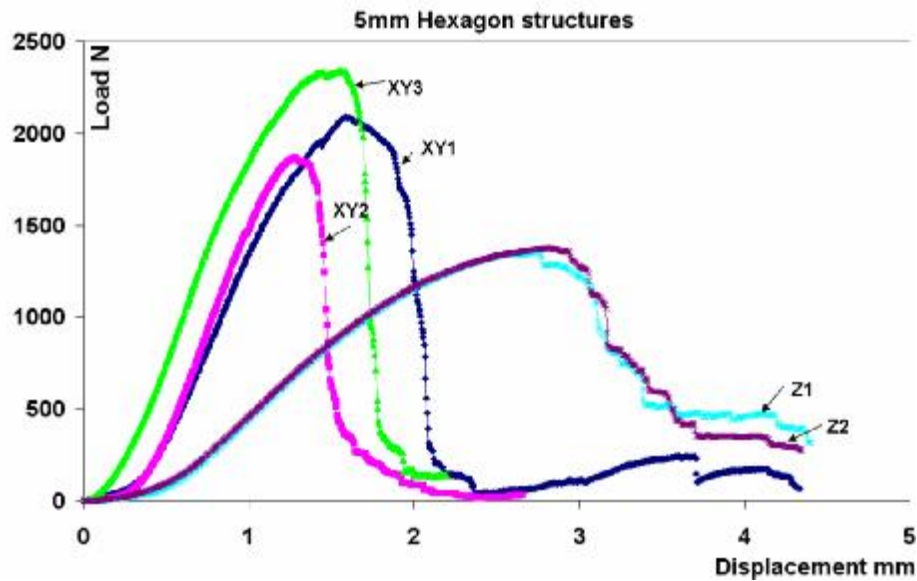


Figure 29: Compression Test Results for 5mm structures with maximum loading up to 2400 N

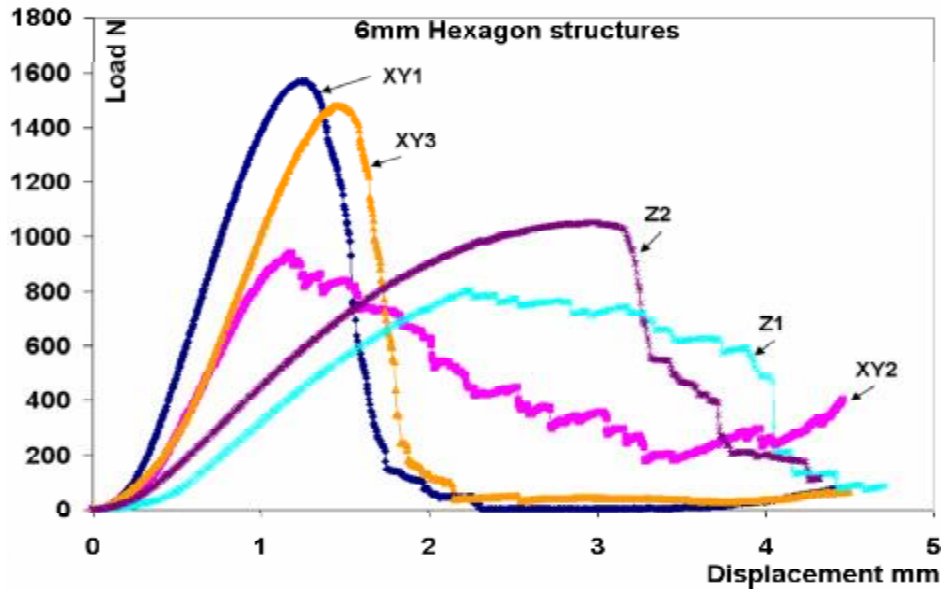


Figure 30: Compression Test Results for 6mm structures

Table 3: Summarizes compression test results for 4 mm, 5 mm and 6 mm structures.

Specimen (average of 3 specimens)	Peak Load (N)	Compressive Strength (MPa)	Strength (MPa)/ Density (g/cm <sup>3</sup> )	E (MPa)	Relative Density ( $\rho^* / \rho_s$ )
4mm XY	5172.95	8.78	17.68	211.27	11.2%,
4mm Z	3374.83	6.01	12.1	79.07	
5mm XY	2098.84	4.07	12.25	106.27	7.5%,
5mm Z	1375.28	2.45	7.37	30.21	
6mm XY	1686.41	2.28	9.69	53.3	5.3%
6mm Z	1275.35	2.21	9.41	25.66	

Gibson and Ashby (1988) have suggested scaling factors for estimating compressive strength and modulus of structures built with different cell densities.

Constants are calculated based on experimental results using:

$$S_c = C_1 * S_{c,s} \left(\frac{r}{r_s}\right)^{1.5} \quad (I)$$

where,  $\sigma_{c,s}$  is the bulk compressive yield strength,  $\rho$  is the density of the structure and  $\rho_s$  is the bulk density of the material.

For the bulk compressive yield strength of 870 MPa for Ti-6Al-4V, the constant  $C_1$  was calculated to be 0.25 with fitting equation to the testing data.

The standard modulus scaling formula

$$E = C_2 * E_s \left(\frac{r}{r_s}\right)^2 \quad (II)$$

was used where  $E_s$  is the bulk elastic modulus of Ti-6Al-4V (110 GPa). The constant  $C_2$  was found to be 0.1656. Figure 31(a and b) shows the relationship between observed and predicted values of the modulus, compressive strength and relative densities of the samples under study. Constants ( $C_1$  &  $C_2$ ) depend on the beam thickness, length and orientation of the beam with respect to the XY plane. These constants are dependent on the cell geometry, and they are calculated for future references. Actual test results are regular modulus and compressive strength calculations. Finite element models described in the next section were used to simulate the effect of different parameters.

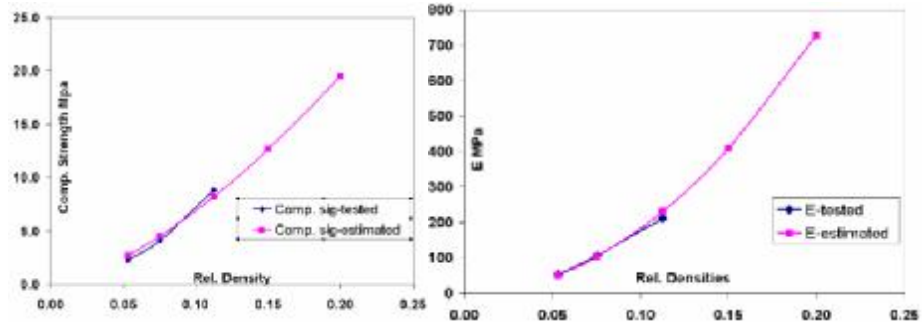


**Figure 31: Comparison of tested and estimated results A) Compressive strength as a function of relative structure density B) Elastic modulus (E) as a function of relative structure density**

### 2.3.4.2. Flexural Test Results

Four sets of bars were fabricated for use in the 3-point bend test as shown in Figure 39-a. A span of 177.8 mm was used for all the tests. The loading rate was 1 mm/min for all bend specimens.

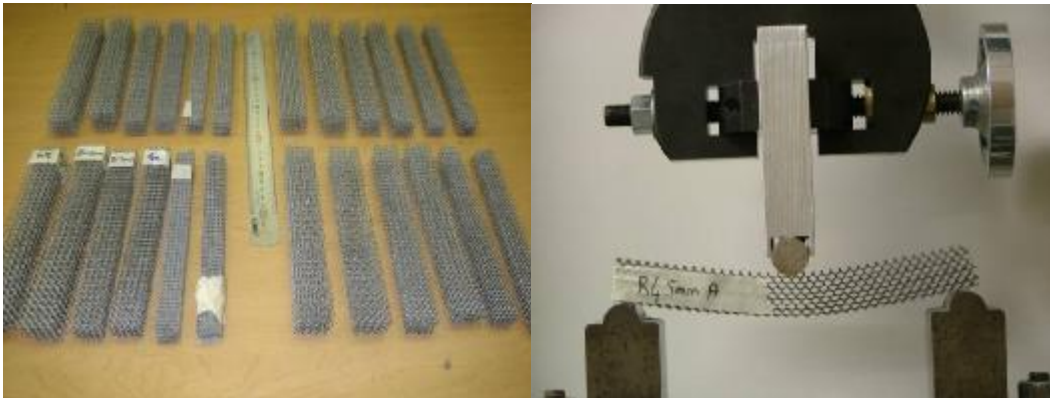


**Figure 32: a) two copies each of three different bend specimens with cell sizes of 4 mm, 5 mm and 6 mm b) Flexural testing**

The specimens had cell sizes of 4 mm, 5 mm, and 6 mm with an overall length of 190 mm. Machine build height was limited due to the powder availability, so cell numbers was less than seven cells. All sets of the specimens had been fabricated under the same vacuum conditions. The flexural modulus was calculated for each specimen and summarized in Table 4. Figure 27 shows test results for different builds. The average

elastic modulus and relative density are given for each specimen type in Table 4. It is calculated based on formula for bending calculations given in previous section.

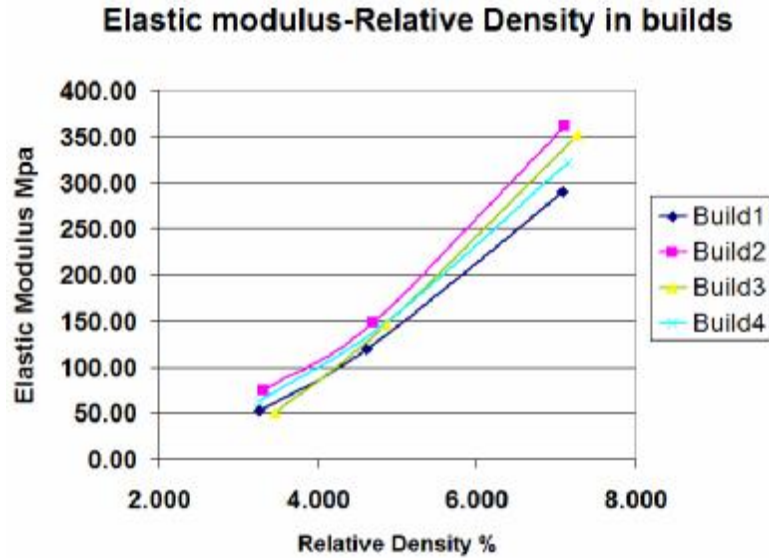


Figure 33: Elastic modulus (E) versus relative density for different builds of specimens. Each build has 2 copies of each unit size of long beams. Data points are average of each build sets for each cell sizes.

Table 4: Bending test results

Bending Samples (min 7 specimens for each cell size)	Flexural Modulus (MPa)	Relative Density (avg)
4mm long bars	336.84±31	7.1%
5mm long bars	139.99±14	4.7%
6mm long bars	61.26±10.4	3.2%

### 2.3.5. Finite element modeling

Test specimens were modeled in Ansys (Ansys, Inc) to compare physical compression test results with simulated values. Ansys 3D beam elements were used to model the struts with the same nodal connections and unit repetitions as were used in the

Solidworks models from which the physical parts were built. The bottom layer's nodal points of each structure were fixed in the model, and the top nodes were displaced 0.1 mm to simulate compression testing. Isotropic material properties were assigned using a Young's modulus of 110 GPa and a Poisson's ratio of 0.3 for each analysis. A square beam profile was used to match the initial CAD geometry. During Ansys simulation, the reaction forces were calculated at the bottom layer's nodes for the different beam thicknesses and unit cell sizes. The predicted modulus as a function of beam thickness for different unit cell sizes is shown in Figure 34b. The effect of change in beam thickness in different cell sizes is shown in Figure 34a.

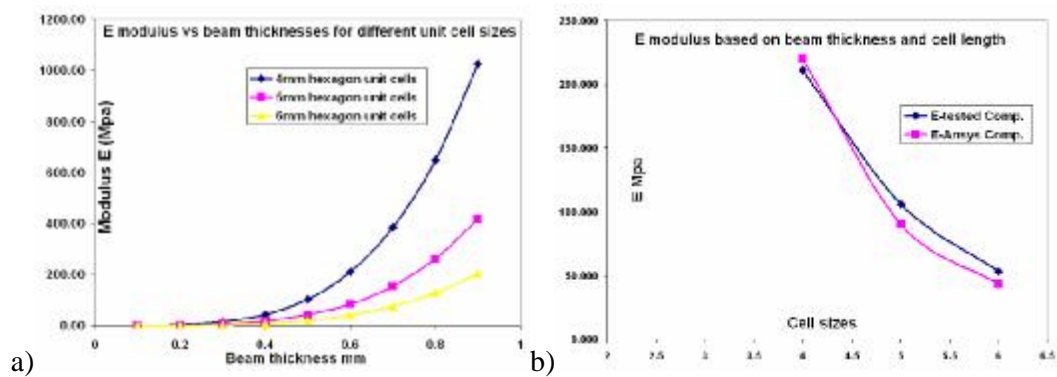
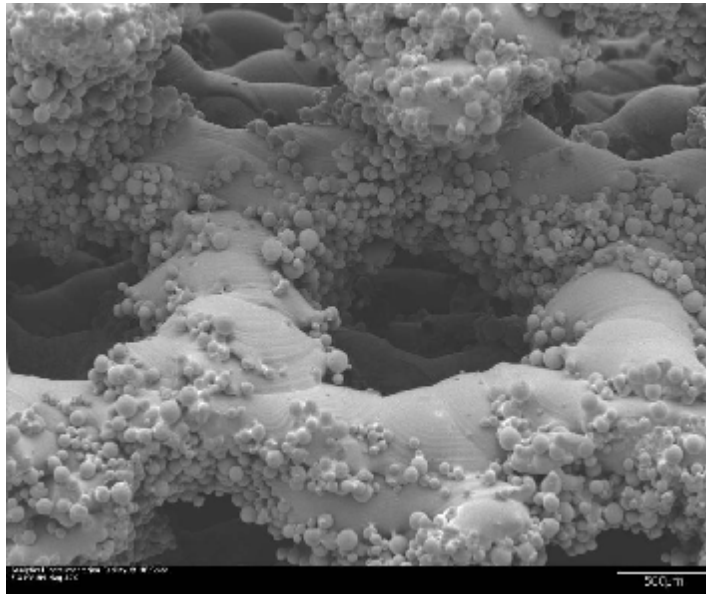


Figure 34: a) Simulated FEA results for different beam thickness of different cell sizes b) Comparison of ANSYS results and Testing results in scaling

### 2.3.6. Discussion

It is possible to predict the modulus of the lattice structures, but there are limitations in terms of the variation in the beam thicknesses. The FEA model suggests that there is a significant change in modulus for variations as small as 0.1mm in the beam thickness of the structure (refer to Figure 34a). The fabricated metal beams also exhibit a surface texture due to sintering and incomplete melting of the metal powder as shown in Figure 35 and Figure 36. These variations in the beam thickness make it difficult to predict mechanical properties for very thin beam structures. Variability in the modulus

between different builds for the same cell geometry and beam thickness has been reported in Figure 33. The EBM machine has a limited accuracy as its calibration is based on interpolation. Small variation in the beam is not very important for the solid section parts, but it is exaggerated in thin lattice structures.



**Figure 35: SEM picture of Lattice structure is showing the unmelted powder attached to the beams.**

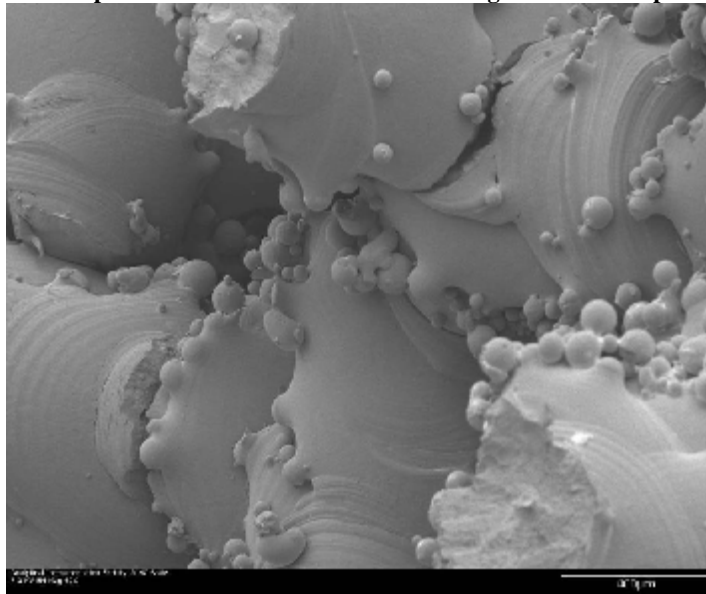


**Figure 36: SEM picture of the crushed lattice structure is shown with sintered Ti64 powder particles.**

### **2.3.7. Conclusions and Future Directions**

This section has reported on preliminary experiments involving the fabrication of titanium alloy non-stochastic lattice structures. It was determined that the smallest strut dimensions that can be fabricated without process optimization is approximately 0.7 mm in diameter. It is furthermore recommended that the strut angle relative to the horizontal build plane not be less than approximately 20° when using 0.7 mm diameter struts. At angles less than this, the connectivity between layers is low, leading to catastrophic drop in the strength of the structure.

This study covered a wide range of cell structures built with relative densities ranging from 5% to 11% that of solid Ti-6Al-4V. The relation of modulus and compressive properties with different densities, cell types and beam diameters was established. This would permit the design and scaling of the structures to suit specific mechanical properties. Ansys FEA models exhibited congruence with equivalent tests on physical specimens after applying a suitable scaling factor. In terms of future directions, the most obvious need is a more formal process optimization effort to improve strut quality and hence material properties. Part of this study could involve post processing operations such as heat treating to effectively "heal" some of the crack initiation sites. The development of functionally graded materials by employing control over the nature of the unit cell over a given geometry would be another direction of research in this field.

A problem for any of the powder-based (laser and e-beam) SFF approaches is powder removal. Most researchers build structures without skins. However, many real world components require covering foam structures with solid skins. Another future topic of study is to look at the material properties of structures built with solid skins that trap the unmelted powder surrounding the lattice. The density of the component will still be

lower than a solid part due to the fact that the unmelted powder has a lower density. A study in this area would involve the effect of uncompacted trapped powder on the strength, stiffness, weight of the structure and better understanding of any operation hazards during fracture.

## 2.4. Rhombic Structures

Other possible 3D lattice structures include cubes, truncated octahedrons, truncated cubes, truncated cuboctahedrons, triangular prisms, rectangular prisms, hexagonal prisms, octagonal prisms, and rhombic dodecahedras (Chua, Leong et al. 2003). The 12-faced rhombic structures were selected for space filling properties and geometric properties suitable for EBM mesh fabrication to use in hip stems. Dodecahedron structures were also used to model orthotropic properties of the bone (Kowalczyk 2006). Each strut of the rhombic dodecahedron unit cell was built in the same orientation with respect to the build plane at an angle of  $\Phi$  fixed at  $35.26^\circ$  based

on  $\tan f = \frac{1}{\sqrt{2}}$  as shown in Figure 37.

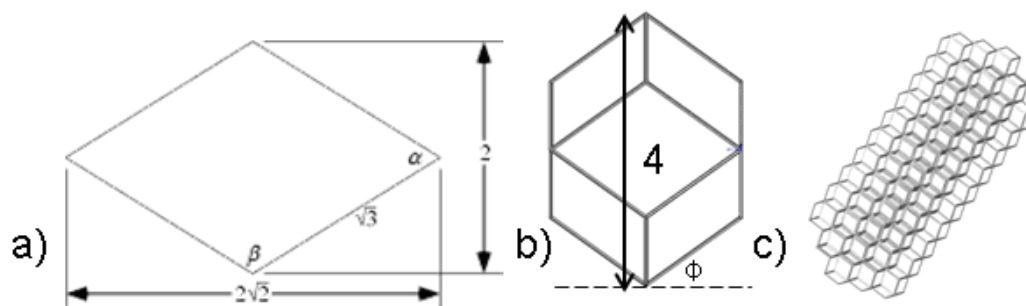
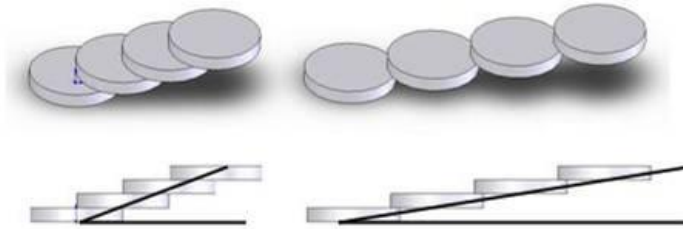


Figure 37: a) Relative dimensions of one face of the rhombic dodecahedron unit cell b) front view of the unit cell c) rectangular flexural test bar with rhombic dodecahedron unit cells

The strut length was equal for all edges of the unit cell. Structures having the same angular beam orientation and equal beam length are preferred to reduce the variability in

the Solid Freeform Fabrication (SFF) processes caused by layered manufacturing of mesh structures. Figure 38 shows the principle of building thin struts using the layered approach.



**Figure 38: Principal fabrication of thin struts using layered fabrication technology.**

In our case, the electron beam melts a dot in each layer. If the strut angle to the build plane is too small, there will be no or little overlap between the successive melted layers resulting in a very weak structure as discussed in previous section.

Unit cells were designed in the SolidWorks CAD package using beam segments with rectangular cross sections instead of circular cross sections. When beams with circular cross sections are used, the size and complexity of the resulting CAD model overwhelms the capabilities of most workstations when the number of unit cells exceeds a certain number. The use of rectangular cross sections drastically reduces the file size in SolidWorks thus allowing larger mesh structures to be modeled. Further, this dramatically reduces the STL-file size and subsequent computational requirements. When the STL-file is sliced, the square cross section of each strut is effectively a dot. When the electron beam melts the metal powder to form the struts, the minimum beam diameter is used and a small circular disc is produced as shown in Figure 38. Compression test and bend test specimens were modeled for different sizes of unit cells in SolidWorks, and were then transferred to Materialise's Magics software as STL files for slicing prior to fabrication on

the EBM machine. Relative densities of the structures were calculated based on the weight of the structure/volume/density of solid Ti-6Al-4V (4.42 g/cm<sup>3</sup>).

### 2.4.1. EBM Manufacturing

Rectangular Ti-6Al-4V compression test and bend test specimens with different densities, from 3.8% to 40%, were fabricated using the EBM process as shown in Figure 39.

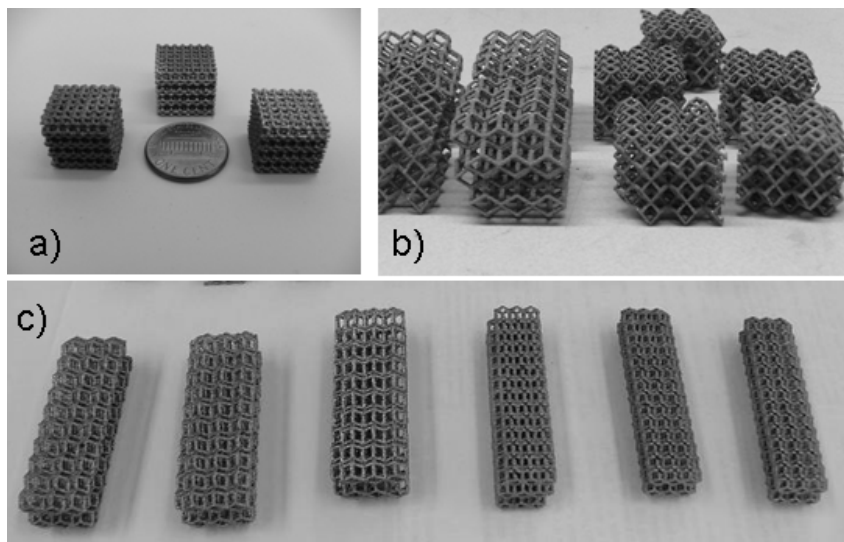


**Figure 39: Structures fabricated via Electron Beam Melting: a) Cubes with 40% relative density (60% porous) b) Cubes with relative densities of 8.0%, 5.0%, and 3.8% c) Bending specimens with 8 mm and 6 mm cell sizes (7.3% and 11.9% relative density)**

### 2.4.2. Testing

Material testing was conducted using an ATS 1605C universal tester. Compression tests on the cube specimens in Figure 39-(a-c) were conducted at a crosshead speed of 5.1 mm per minute. One set of compression samples was tested parallel to the build direction while a second set was tested perpendicular to the build direction. The overall area of the parts was used to calculate the compression strength and

modulus. A 3-point flexure test was used for the bending specimens as shown in Figure 40.

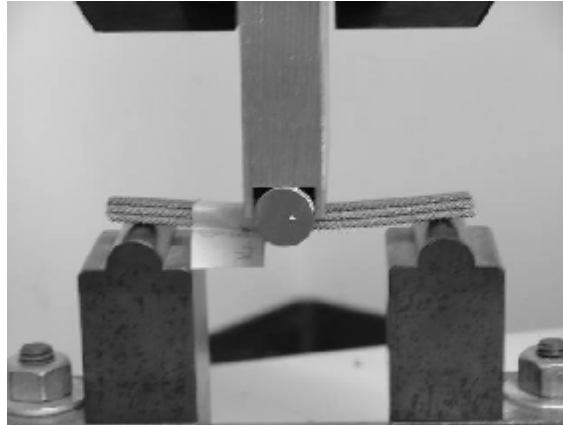


Figure 40: Three point flexure testing of rectangular mesh beam

### 2.4.3. Analysis and FEA

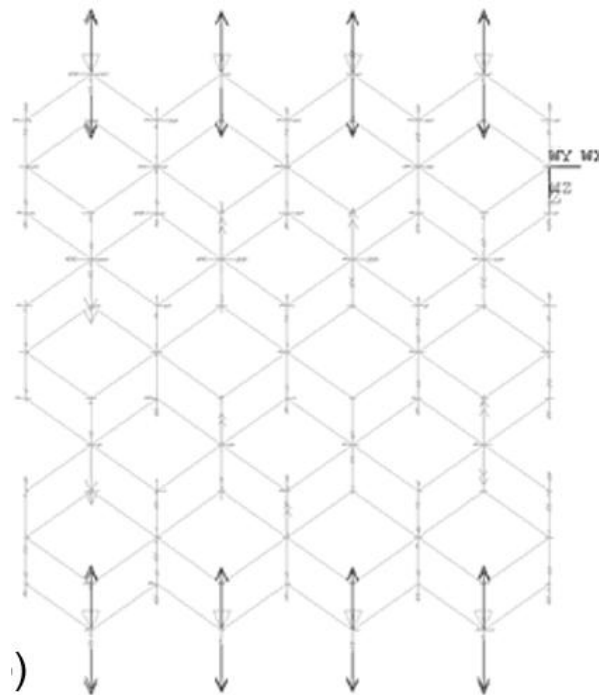


Figure 41: ANSYS simulated mesh structure

To compare the unit cell test results for the physical structures, scaling rules were modeled in ANSYS using 3D beam elements. Rhombic structures were created in ANSYS with 4 unit cells in X and Y and 3 unit cells in Z as shown in Figure 41. Bottom nodes were fixed in the Z-direction and top nodes were moved 0.1 mm downward to simulate compression testing in the plane parallel to the build orientation. Nodes at the left face were fixed in the Y-direction and nodes at the right face were moved 0.1 mm to the left to simulate compression testing in the plane perpendicular to the build orientation. Both compression test directions were simulated for 6 mm, 8 mm, 10 mm, and 12 mm cell sizes to show the density effect for different orientations. The cross sectional area of each beam was  $0.49 \text{ mm}^2$  with a square profile. A modulus of  $E = 110 \text{ GPa}$  and Poisson's ratio of 0.3 were assumed. Relative densities of the simulated structures were calculated based on their cross section and overall dimensions in ANSYS.

#### **2.4.4. Compression Testing**

Physical compression test results are given in Table 5 for 4 lattice densities. Specimens loaded parallel to the build direction are labeled with an "XY" orientation. Specimens loaded perpendicular to the build direction are labeled with a "Z" orientation. The 3 mm unit cell structures could not be tested until failure due to the load limit of the testing machine (5000 lbs). The cell height is taller in the XY orientation than the Z orientation due to the geometry of the structure as shown in Figure 37-b. As can be seen in Table 5, compressive strength in both the XY and Z direction decreases with increasing

cell sizes. This makes intuitive sense, as the structure's relative density decreases when the cell size increases.

**Table 5: Compression testing of rhombic structures with cell sizes from 3 mm to 12 mm.**

<b>Structures (Cell Size-Orientation-Sample#)</b>	<b>Peak Load (N)</b>	<b>Relative Density</b>	<b>Compressive Strength (MPa)</b>	<b>Compressive Strength/Density ratio (min) MPa/(gr/cm3) Ti6Al4V(solid)=4.43gr/cm3</b>
3mm- XY-#1	18777.23	0.41	85.72995**	47.20
3mm- XY-#2	19530.29	0.41	91.34936**	50.29
3mm- XY-#3	19324.38	0.41	89.9208**	49.51
3mm- Z-#1*	18717.37	0.41	91.7393**	50.51
3mm- Z-#2*	18879.29	0.41	94.04639**	51.78
3mm- Z-#3*	19132.2	0.41	94.93092**	52.27
8mm- XY-#1	1682.04	0.08	2.977589	8.40
8mm- XY-#2	1799.76	0.08	3.18598	8.99
8mm- XY-#3	1661.27	0.08	2.940821	8.30
8mm- Z-#1	1990.24	0.08	2.890102	8.15
8mm- Z-#2	2131.88	0.08	3.095783	8.74
10mm- XY-#1	1197.87	0.05	1.405769	6.35
10mm- XY-#2	1160.47	0.05	1.361878	6.15
10mm- XY-#3	1066.3	0.05	1.251364	5.65
10mm- Z-#1	713.47	0.05	0.84711	3.82
12mm- XY-#1	976.17	0.04	0.818962	4.62
12mm- XY-#2	1010.66	0.04	0.847898	4.78

\* Same sample tested also for Z orientation

\*\* Not peak strength (Loading limitation)

A graph of compressive strengths for tests in the XY orientation at different relative densities is shown in Figure 42a. The compressive scaling equation is fitted for test data according to the formula

$$S_c = C_1 * S_{c,s} \left( \frac{P}{P_s} \right)^{1.5}$$

, where  $C_1 = 0.341$  and  $S_{c,s} = 897$  MPa.  $C_1$  was calculated from testing values for future references. It may not be correct if machine calibration or machine settings are different. Structures will have different properties under small electron beam melting parameters.

A comparison of the modulus in the XY and Z direction was made using ANSYS as shown in Figure 42-b.

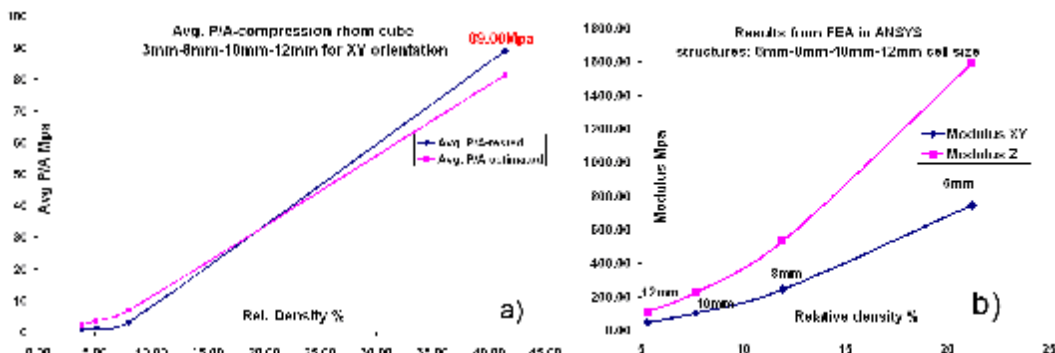


**Figure 42: a) Average compression strength versus relative density for tested and estimated mesh structures b) Ansys simulated results for compression stiffness versus relative density in XY orientation and Z orientation.**

In general, the structures are stiffer in the Z-direction than the XY-direction, and the difference increases with decreasing cell size. Results of average tested modulus (MPa) for 8 mm, 10 mm, and 12 mm structures are compared to the predicted results from ANSYS in Table 6. The actual and predicted modulus values differed by nearly a

factor of 4. In the FEA model, struts are assumed to be smooth with cross sectional areas of  $0.49 \text{ mm}^2$ . The actual struts have a rough texture with thicknesses that range from 0.3 to 0.7 mm. These results can be used to modify the models of the lattice structures so that the physical behavior of the as-fabricated structures is predictable.

**Table 6: Comparison of tested structures and simulated structures with  $0.49 \text{ mm}^2$  square profile beams.**

Sample	Tested E MPa (XY orientation)	Tested E MPa (Z orientation)	Ansys (XY)	Ratio -XY Ansys/Test	Ansys (Z)	Ratio-Z Ansys/Test
6mm	-	-	747.43	-	1592.43	
8mm	60	78.81	241.30	4.02	532.30	6.75
10mm	25	23.63	99.79	3.99	223.88	9.47
12mm	12	-	48.38	4.03	109.57	-

#### 2.4.5. Flexure Testing

The results from flexure tests of 3 mm unit cell specimens are reported in Figure 43. The average bending strength was approximately 150 MPa which is higher than porous tantalum at 110 MPa (Zardiackas, Parsell et al. 2001). The 3 mm unit cell samples showed a linear load-displacement relationship with an average modulus of 12 GPa. The average modulus for 6mm and 8mm structures in the XY orientation were 349.5 MPa and 47 MPa respectively.

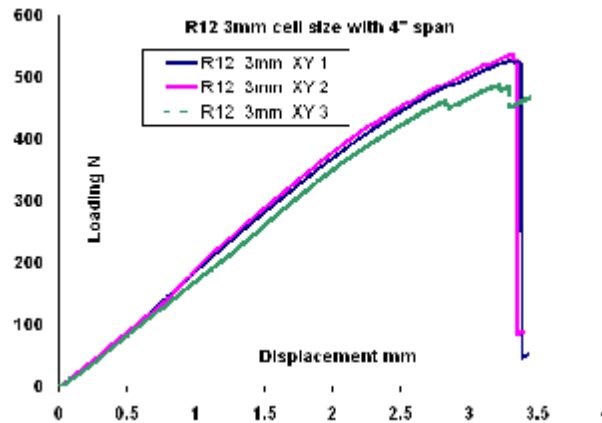


Figure 43: Bending test results for specimens with unit cell size of 3 mm and 40% relative density.

Table 7: Bending test results for 3mm, 6mm, and 8 mm structures

Specimen (cell size-orientation-sample #)	Peak load N	E MPa	My/I MPa	Relative Density %
3mm XY #1	528	11990	151	39.8
3mm XY #2	537	12749	154	39.5
3mm XY #3	486	11291	139	40.0
6mm XY #1	471	261	10	11.9
6mm XY #2	688	438	15	11.9
6mm Z #1	293	133	6	11.9
8mm XY #1	183	47	2	7.3
8mm Z #1	434	55	4	7.3
8mm Z #2	376	47	3	7.3

#### 2.4.6. Discussion and Conclusions

Direct metal fabrication technologies such as Electron Beam Melting show considerable promise for the fabrication of custom orthopedic implants with tailored

material properties. However, the processes have limitations that must be considered during the design of such implants. Building non-stochastic lattice structures is possible, however the orientation of the lattice struts during the fabrication is important. The beam elements must be oriented such that the inclination is within a certain range. While FEA models generally assume struts with smooth surfaces and constant cross sections, the fabricated struts have textured surfaces with slightly varying cross sections. These differences must be reflected during the design of implants through use of safety factors or other methods. By changing the unit cell size, a predictable compressive and bend strength can be achieved with a predictable modulus. By using such non-stochastic mesh structures, components with tailored mechanical properties can be designed and fabricated.

The non-stochastic mesh structures have been used to design a hip stem with a lower bend modulus aimed at lowering stress shielding and uneven bone remodeling. Related topics are discussed in design chapters.

An important future research topic is fatigue testing of these non-stochastic mesh structures to ensure that the non-stochastic mesh structures will perform equally well over time. The performance of the non-stochastic mesh structures can be further improved using design optimization algorithms based on a specific loading scenario. Distribution of the solid regions of the implant can be calculated based on topology optimization that minimizes compliance for a given material volume (Sigmund 1995). Manual optimization studies conducted on such complex 3 dimensional structures is a computational and time consuming task that would not necessarily be feasible on a case by case basis. Further research and development on semi-automated design optimization procedures is therefore needed. A functionally gradient design approach is being considered as well where the

stem is fully dense at the core and is gradually transitioned into a mesh structure. Such a structure can more easily be designed and verified using FEA to ensure appropriate bend stiffness as opposed to using optimization. Further, the actual shape and size of the stem can be custom designed to better fit a specific patient based upon a model of the femur derived from a CT-scan. Such a design would be more time consuming and more expensive than a standard implant design, yet the potential for increasing the longevity of the implant could more than make up for the additional cost. Another advantage of fabricating a hip stem using EBM technology is that the porous bone ingrowth surfaces can be built in at the same time, thus saving several fabrication steps. If bone ingrowth is not desired along the entire stem, a thin skin of titanium can be added to those areas and later on polished during the finishing step to prevent bone ingrowth.

## **2.5. Melting effects on mesh structures**

It was observed that mesh structures are showing variation between different builds for the same build files. This short section discusses the effects of changing the mesh melting parameters for the same structure geometry. It also shows the effect of adding supporting beams to the meshes to increase their strength.

### **2.5.1. Structure Design**

Rhombic dodecahedron structures were designed with 4 cells in the xy and 3 cells in the z direction. The beam thickness was 0.4mm for the mesh structures. They have a square profile to reduce the STL file size for further file preparation. Additional beams were added to the meshes to investigate the improvements in mechanical properties for different supports. The extra beams used at different orientations have a cross section of

0.8mm thickness. Each set has four different structures as shown in Figure 44. The first mesh structure has four body diagonal beams, the second structure has vertical beams which pass through the unit cells, the third structure has 8 face diagonal beams, and the fourth structure was the control without any extra support. .

### 2.5.2. Manufacturing

Three sets of structures, a total of 12 specimens, were manufactured on the same build plate. Melting parameters were assigned using different processing themes, see Table 8. Ti6Al4V powder was used for all the samples. Preheating parameters were set to 19 repetitions per layer, focus offset was set to 35mA, line order was set to 1.1mm at 20 intervals, beam current varied from 1 to 18mA and all other parameters were used at the default Ti6Al4V parameters.

**Table 8: Melting parameters for 3 sets of mesh structure samples**

Samples	Melting Theme	Parameters	
		Speed mm/sec	Current mA
Mesh set 1 (P1)	Melt file	180	2
Mesh set 2 (P2)	Preheat2	180	3
Mesh set 3 (P3)	Postheat2	100	3

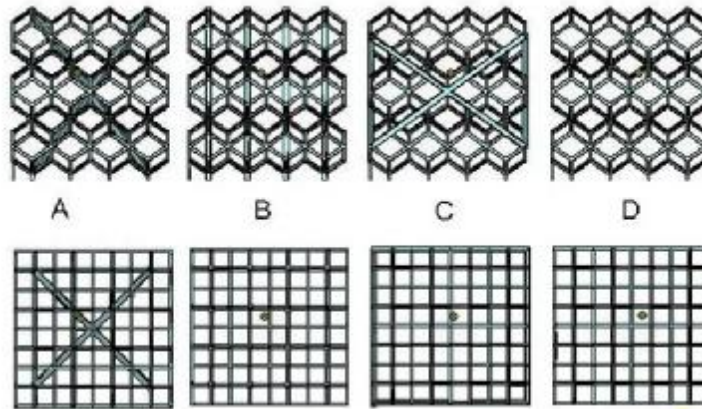


**Figure 44: Top and front views of the sample a) mesh with extra 3D diagonal beams b) mesh with extra vertical beams c) extra 2D side crosses d) control structure without supports**

### **2.5.3. Mechanical testing**

The same testing set up was used as in previous crush testing and each specimen was placed between steel parallel plates and crushed at 1mm/min with the ATS 1605 universal testing machine in a random order. Some specimens could not be tested to the failure due to the loading limitation of the testing machine at 5,000 lbs.

### **2.5.4. Results and Discussion**

The average of the max force on specimen type 2, 3 and 4 using the first processing conditions ( P1) was 4,403N. It increased to 10,305N using the second processing conditions (P2) and almost doubled again using the third processing conditions (P3) with a total of 19,063N as seen in the figures 48 to 50.

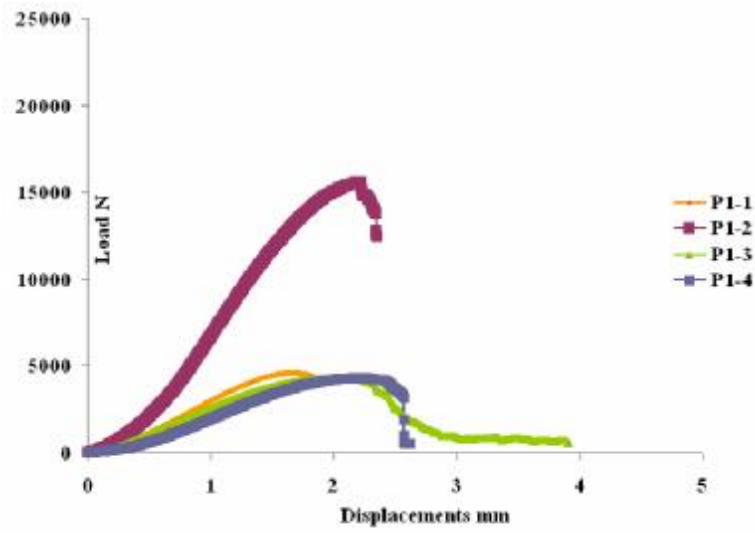


Figure 45: Load versus displacement data of Set 1 sample are shown in the figure. P1-1 is referring to sample A and numbering is consistent with the given sample figure.

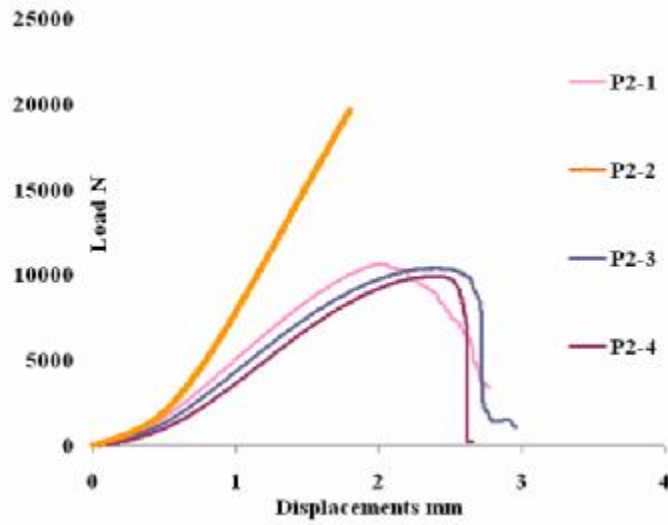


Figure 46: P2-1, Set 2 sample, is referring to sample A and numbering is consistent with the given sample figure.

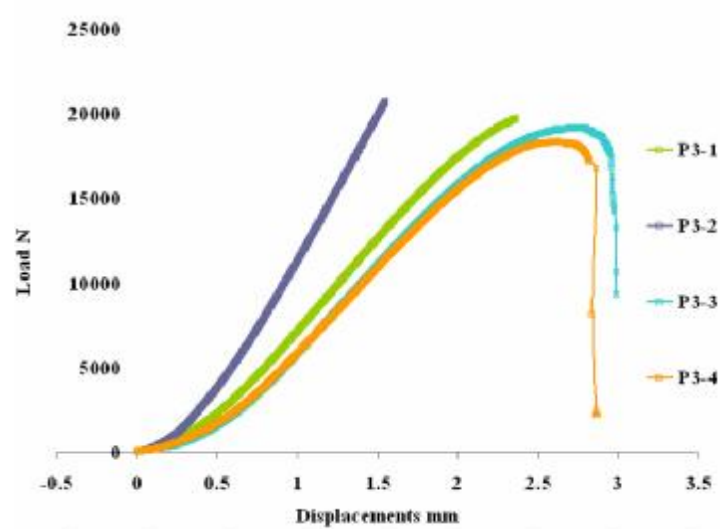


Figure 47: P3-1, Set 3 sample, is referring to sample A and numbering is consistent with the given sample figure.

The structures were showing better plasticity compare to the original mesh structures shown in the previous section. The additional supports were changing the failure mode and for type C they were crushing at the corners instead of the diagonal (2D surface supports). Type A was crushing when the 3D body diagonal supports failed. Type B has vertical supports and they could withstand much more load before breaking. It is important to remember that the loading direction was vertical. However, earlier lattice structures failed following a shear line close to  $45^\circ$  and the control specimens without additional supports were crushing at the shear line similar to earlier results. Additional supports changed the failure mode and the maximum failure load significantly. The beam thicknesses were not affected that much by the different melting parameters, but it was enough to show a significant difference in stiffness and yield load (see Table 9). In earlier sections, the effect of beam thickness on the modulus was shown and this short test confirms the experimental results as well. In all 3 sets, support type B showed

consistently higher stiffness compare to the other samples. Support type A, C, and the control type D all have similar stiffness and yield curves within each sets.

Elastic modulus of the same topology can be compared with

$$\frac{E^*}{E_s} = C_1 \left(\frac{r^*}{r_s}\right)^2 \text{ and also } E = C_3 * E_s * \left(\frac{t}{l}\right)^4$$

,where t is the thickness and l is the length of the unit cells. Max force over these structures may be used to calculate an improvement ratio over Set-1 (P1) and compare with the difference in beam thickness. If the beam thickness ratio is more than the force ratio, it may be stated that the expected change in modulus was not observed and quality of the structure did not improve. If beam quality is improved, the structure will show a much better ratio than the thickness ratio as shown in Table 9. Specimens in Set-3 showed much better improvement than expected with an increase in thickness. However, Set-2 has a similar force ratio and thickness ratio. It also proves that structure quality can be improved with changing the parameters.

**Table 9: Beam thicknesses and comparison to the max force**

Specimen	Average Beam Thickness (mm)	Average of the Sets	Thickness Ratio (TR)	TR^4	Max Force (N) over Type 2,3,4	Force Ratio
P1-1	0.821	0.851	1.0000	1.0000	4403	1
P1-2	0.889					
P1-3	0.847					
P1-4	0.847					
P2-1	1.054	1.021	1.2002	2.0753	10305	2.34045
P2-2	1.058					
P2-3	0.965					
P2-4	1.008					
P3-1	1.016	1.109	1.3035	2.8868	19063	4.329548
P3-2	1.084					
P3-3	1.151					
P3-4	1.185					

### **3. APPLICATIONS OF STRUCTURAL OPTIMIZATION**

In the past Finite Element Analysis (FEA) has been mainly used in the design of the outer shape of implants. It has also been useful in modeling the interaction between the implant and the bone. Different optimization methods have been used in the designing of structures with prescribed mechanical properties. Topology optimization has been used to define the structural layout for given loads and material properties. The shape parameters may also be adjusted after setting the topology. A review of topology optimization and also beam-based structural optimization will be discussed in this section.

Shape and topology optimization have recently gained interest due to significant industrial applications and importance (Rozvany, Bendsoe et al. 1995). Structural optimization has been used to improve the geometry based on an objective function and a set of constraints.

#### **3.1. Topology Optimization**

The topology optimization method was mainly developed by Bendsoe and Kikuchi in 1988, and Sigmund extended their work to design material microstructures (Bendsoe and Kikuchi 1988; Sigmund 1994; Sigmund 2000). The material was considered as a 3D image and the image model was used as a fixed design domain. Topology optimization involves the determination of features and the connectivity of the domain and it derives the layout of the structure in that limited domain. Given parameters are generally loading, support conditions, volume of the structure and constraints about the design. The outputs are size, shape, and connectivity of the structure. In the distribution of material method, the structure is modeled similarly to a black and white

rendering of an image. Integer variables are replaced by continuous variables and penalty functions or filters change the solution to 0 or 1, which means there is material or there is no material at each pixel (unit). Different penalty functions should be investigated to determine the effect on the results. Interpolation methods have been used to convert the problem into a large scale sizing problem on a fixed domain. Computational procedure for the Power Law method consists of the following steps:

- ✓ Choose a reference domain
- ✓ Set the ratio of solid to void volume
- ✓ Construct finite element mesh for the domain
- ✓ Distribute material homogenously
- ✓ Compute initial displacements and strains
- ✓ Compute compliance of this design. Check stopping criteria. It may be based on improvement or optimality conditions.
- ✓ Update variables
  - ∅ Updating variables and performing necessary iterations can be different for each solver. Some heuristics can be used, for example, multiple agents at the same time and update the variables according to the global best and personal best of agent results.
- ✓ Repeat steps.
- ✓ Transfer material distribution values to CAD model with smoothing functions.
- ✓ The final answer from the topology design may not be useful as is and further post-processing is necessary to add different results together or apply further filtering.

Minimum compliance design is the general set up for the method. It is a design to obtain a maximum global stiffness under simple constraints. Material is distributed to the design domain and iterations are calculated until no marginal improvement is achieved or it is satisfying the optimality conditions. A 0 or 1 discrete variable problem is generally replaced with a continuous variable problem. The simple isotropic penalty method (SIMP) is one possible way to apply the proportional stiffness and process the iterations with continuous variables. Stiffness in discrete set up is  $E_{ijkl} = hE_{ijkl}^o$ , where  $h=0$  if not material,  $h=1$  if there is a material. In proportional stiffness setup:

$E_{ijkl}(x) = p(x)^{\text{penalty}} \bar{E}_{ijkl}$ , where  $E_{ijkl}$  rigidity tensor and  $p(x)$  shows the density from 0 to 1, and  $\text{penalty} > 1$ . The penalization factor in the SIMP approach is typically set to 3 to get solid and void regions. Details of the basic algorithm can be found in Bendsoe's book (Bendsoe and Sigmund 2003). Iteration heuristic is fast and efficient for these types of problems (volume reduction).

Sigmund has published a simple version of the topology optimization code, 99 lines, as a starting material and it is written in Matlab (Sigmund 2001). Online web topology programs are also available at his group's website<sup>4</sup>. Reported complications are related to topology optimization mesh dependency, and checkerboard problems that break the connections. Several methods have been developed to avoid those issues. Other methods of solving optimization problems of complex geometries such as genetic algorithms (GA), method of moving asymptotes (MMA), particle swarm optimization

---

<sup>4</sup> <http://www.topopt.dtu.dk/>

(PSO), simulated annealing (SA), and sequential convex programming (SCP), will be discussed in the next sections.

Hollister et al. used the image based homogenization method to design scaffold microstructures (Hollister, Maddox et al. 2002). The relation between the microstructure and the stiffness was computed by using homogenization theory. Constraints were added for cell or gene delivery with a minimum porosity threshold. Stiffness and porosity were the two main concerns in their study. Two objective functions were defined and solved using the Matlab nonlinear optimization function. Constraints were defined for the porosity and the modulus of the scaffold. The topology was represented as a voxel dataset created from a MRI or a CT scan. The voxel design was converted into STL format and molds were done for casting the Hydroxyapatite scaffold as shown in Figure 48. The Scaffolds of the mandibular condyle were well matched to the trabecular bone properties.

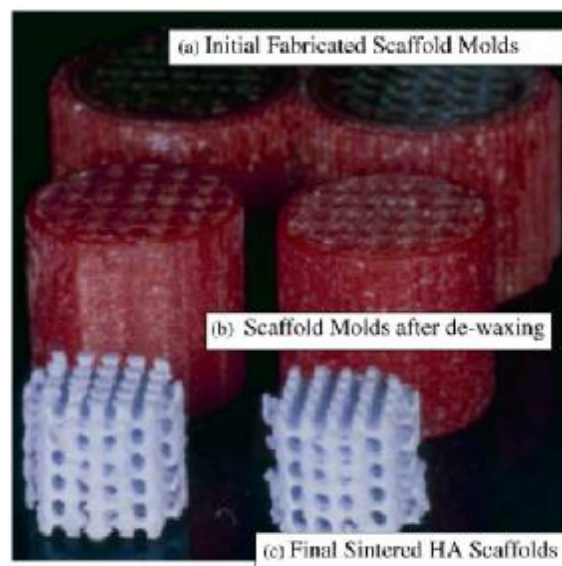


**Figure 48: Molds and sintered final parts. (Hollister, Maddox et al. 2002) with permission from Elsevier.**

Lin et al. showed that structures can be designed to match anisotropic properties of human trabecular bone with different porosities (Lin, Kikuchi et al. 2004). An integrated topology optimization design method was used with a large-scale voxel based solver for designing 3D microstructures. This was a general layout optimization problem. The material density was distributed within the unit cell to match the effective stiffness tensor of a scaffold with a given porosity level. The problem was solved with inner and outer loop solvers. After the inner loop converged in low resolution, it passed it to the outer loop and was solved at a higher resolution. Checkerboard problems were also reported and a smoothing filter was used to solve this problem. Inner structure connectivity was achieved by using the visualization toolkit image processing library (The Visualization Toolkit User's Guide, Kitware ,Inc.). The final microstructure topology was converted to STL format and then prototyped with 3D inkjet printing. Trabecular tissue, 3D structure with negative poisson's ratio, and other tissues were targeted and produced effectively. Trabecular tissue was assumed isotropic and its elastic constants were found for a given porosity level. It has been reported that the bulk material stiffness properties limit the achievable porosity and targeted stiffness level for an optimized structure. For example, it may not be possible to achieve a 10GPa stiffness structure and porosity higher than 50% with a 20GPa bulk material. Different constraints resulted in different structures as can be seen in Figure 49 and Figure 50.

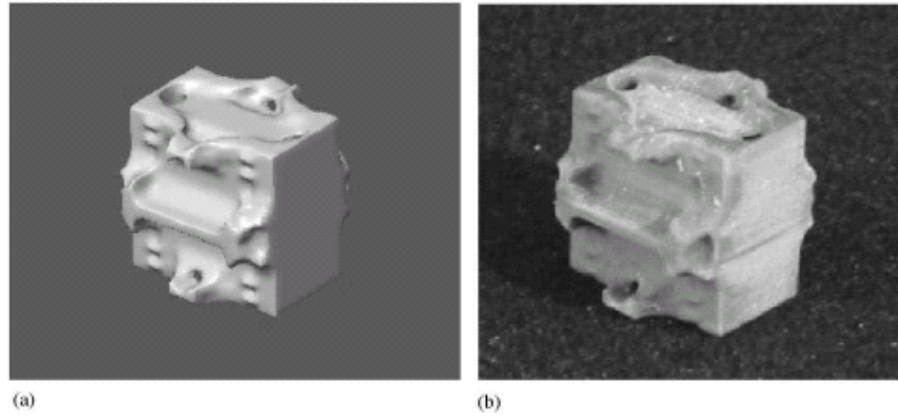


**Figure 49: Porosity level 49% for mandibular condyle (Lin, Kikuchi et al. 2004) reprinted with permission from Elsevier.**

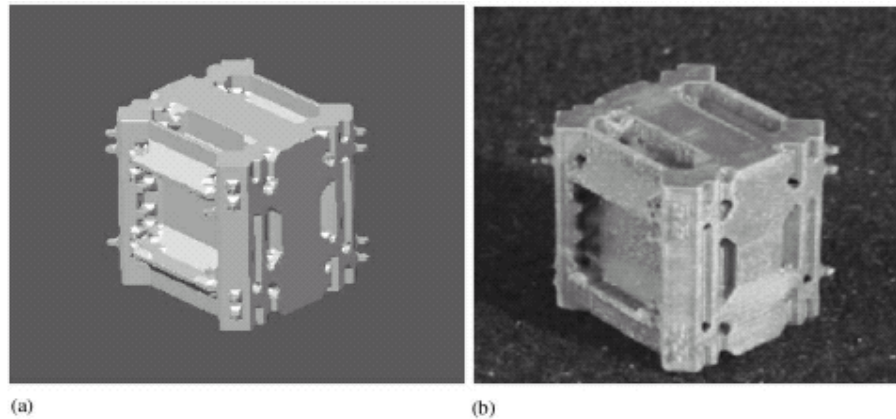


**Figure 50: Porosity level 35% for mandibular condyle (Lin, Kikuchi et al. 2004) reprinted with permission from Elsevier.**

Hollister showed that 3D polycaprolactone (PCL) scaffolds can be designed with conditions for cell migration, mass transport (that is permeability and diffusion) properties, and linear elastic properties (Hollister 2005). The Scaffold exterior was designed with additional surgical fixation elements and the microstructure was created using topology optimization. Boolean operations were used to integrate the microstructure design with the model of the anatomical defect. The final fabricated scaffold had a good fit to the anatomic reconstruction site. Selective laser sintering was

used to fabricate the scaffolds. It was reported to perform well with improved cell migration and tissue ingrowth.

Buhl extended the topology optimization to include support conditions (Buhl 2002). The support conditions in the standard topology optimization settings are defined on the outer edges of the part. Supports were allowed inside the structure. If they are created everywhere, the structure will be the stiffest structure for a compliant minimization problem. Each node has a horizontal and a vertical spring to create a new support model. A cost vector was added to calculate the total cost of additional supports in different locations. The unit cost of each support at different regions was a parameter to the model. Gradient cost functions were possible. In these settings, additional supports inside the structure can be allowed and adjusted with a cost function and a total cost limit of all supports. Limiting conditions were added to prevent some obvious local solutions. Support generation inside the structure was used for compliant structure generation. The displacement was maximized at the defined points. The checkerboard problem (that is a creation of disconnected cells similar to the black and white fields of a checkerboard) was also discussed in their study. Microscopic compliant mechanisms were designed and solved by the Method of Moving Asymptotes (MMA). Structures were changed greatly with the change in cost of the supports. A micro gripper mechanism was designed based on a design domain with support areas as shown in Figure 51.

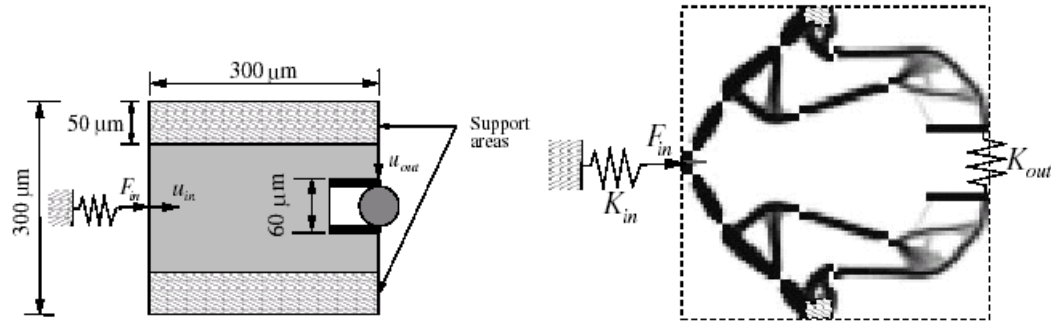


**Figure 51: Design domain and resulted optimal topology with support design method, (Buhl 2002) reprinted with permission from Elsevier.**

Lopes et al. used topology optimization to design rotational parts for a generator under self-weight and inertial forces (Lopes, Stump et al. 2005). Optimality criteria were applied and ANSYS was used with the parametric design language. A SIMP (simple isotropic material with penalty) model was used to parameterize the model. In the SIMP approach, the material tensor is written with a penalization factor over density parameter for each element. It is a generic method of solving the density of each element. Design of hydro generators was done using different volume constraints.

Jang applied design space adjustments and refinement methods for large scale topology optimization problems (Jang and Kwak 2005). The design space was reduced and expanded by level refinements, which reduced the number of elements needed for convergence. Bone growth was simulated for a healing defect and the simulations showed that bone growth filled the defect.

Huang et al. applied topology optimization to design micro compliant mechanisms (Huang and Lan 2006). Gradients of the strain energy and mutual strain energy were used to solve the optimization problem. Sequential linear programming (SLP) was used with the first term of the Taylor series expansion. For a given initial design variable, ANSYS

was used to get the strain energy and the mutual strain energy, and then Matlab was used to solve the problem. Iterations continued between Matlab and ANSYS until convergence was achieved. The 3D micro compliant amplifier reached convergence after approximately 100 iterations. The design was fabricated and tested as shown in Figure 52.

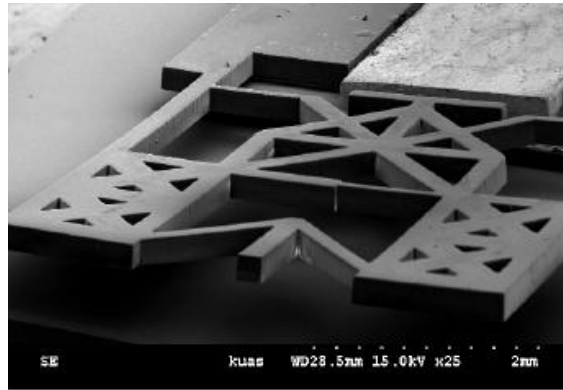


**Figure 52: SEM photo of 3D compliant mechanism and experimental measurement set up, (Huang and Lan 2006) with permission from IOP publishing.**

### **3.1.1. Results from topology optimization**

The homogenization method was applied for a limited number of examples. The ANSYS topology optimization module was used to solve the example models, but connectivity issues between the voxel units were a problem. Examples are shown below for 2D and 3D cases. The boundary of the first structure was defined and meshed with planar elements. The left side was fixed as shown in Figure 53. Simple volume constraints are used to reduce the total material volume. The volume was restricted to 50% for the first case and to 75% for the second case. The figure shows the changes in the element densities. The default objective was to increase the stiffness. An ANSYS topology optimization algorithm changed the density of each element to satisfy the volume constraint at each iteration.

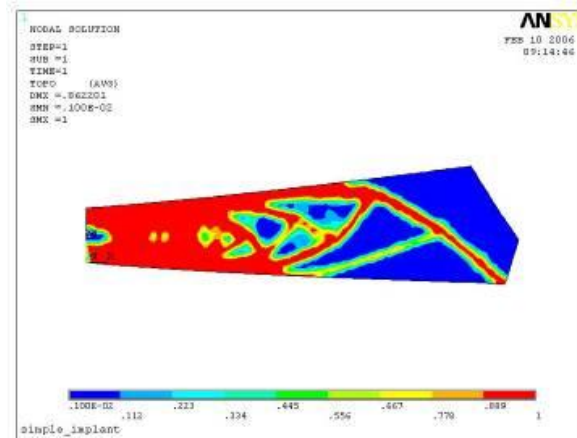


Figure 53: Left side of the material boundary was fixed and loading was at right bottom corner in -Fx and Fy direction. Volume reduction is constrained to 50% with 60 iterations.

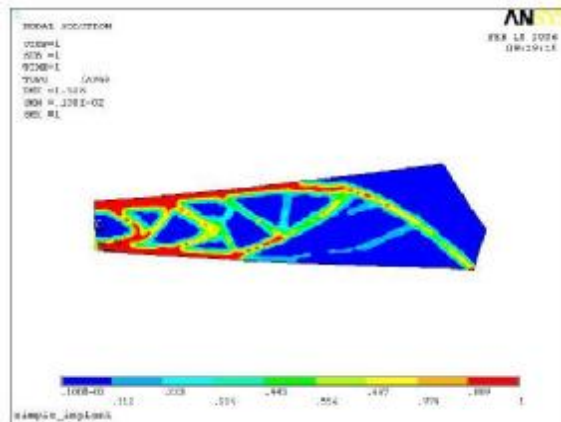


Figure 54: Volume reduction is constrained to 75% with 20 iterations.

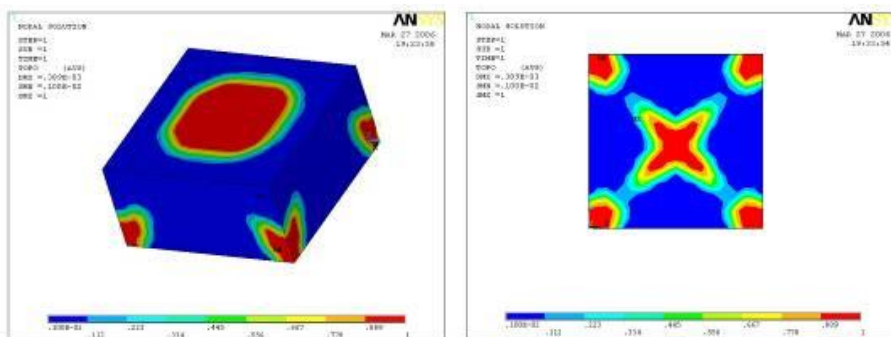
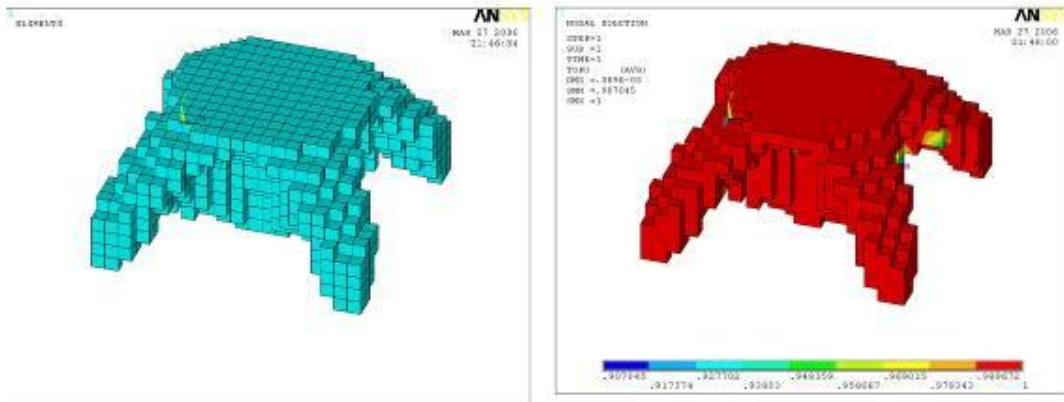
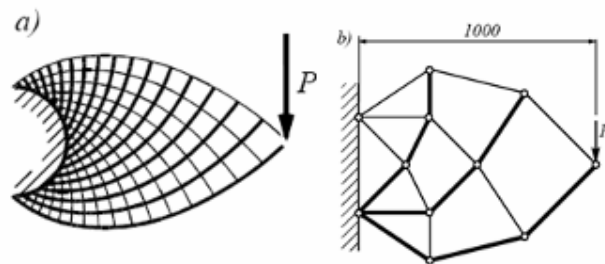


Figure 55: 3D volume topology optimization example. Force is applied at the bottom corners. Structure volume reduced to 50% of initial boundary volume. Left are density readings in the boundary. Right is one slice showing the cross section density.



**Figure 56: Selected elements based on density of 0.9. Zero density means void.**

A Mitchell type structure was used to test the process of creating structures from ANSYS topology optimization to real EBM parts.



**Figure 57: Mitchell type test part original and simplified**

The part domain is defined to set up a simple problem as show in the Figure 58. The rectangular area and the half circle were combined to define the part domain. The right side is fixed and a downward force is applied at the left side. The desired volume reduction is set to 85%.

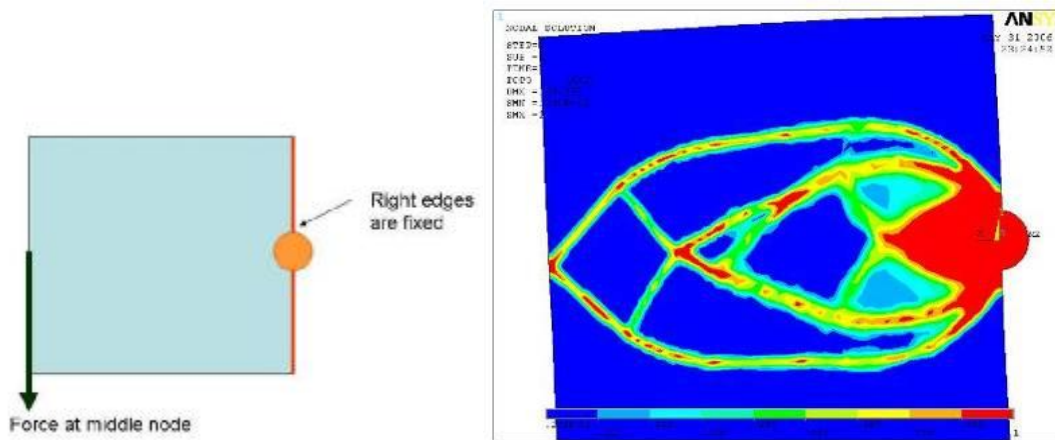


Figure 58: Original structure and final structure with element densities in the topology optimization modules (ANSYS).

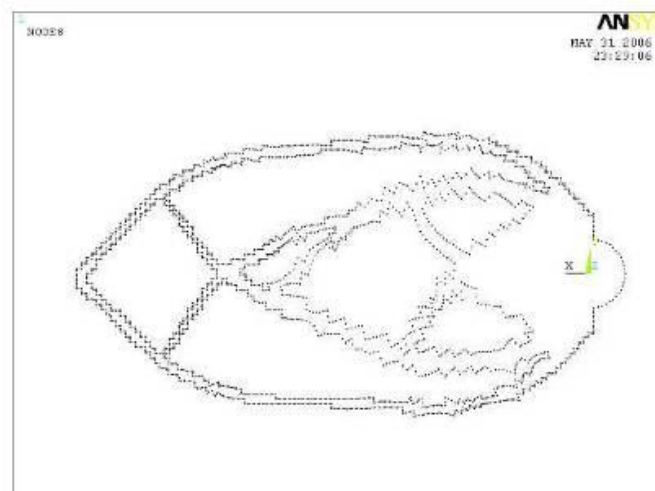


Figure 59: Outside nodes of the selected elements which have densities between 0.4 and 1.

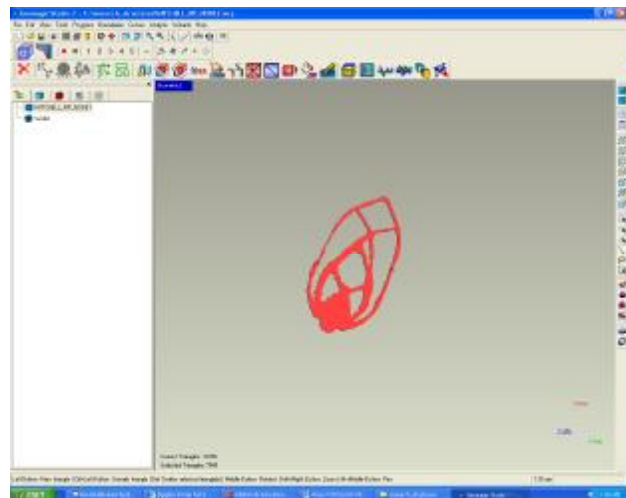
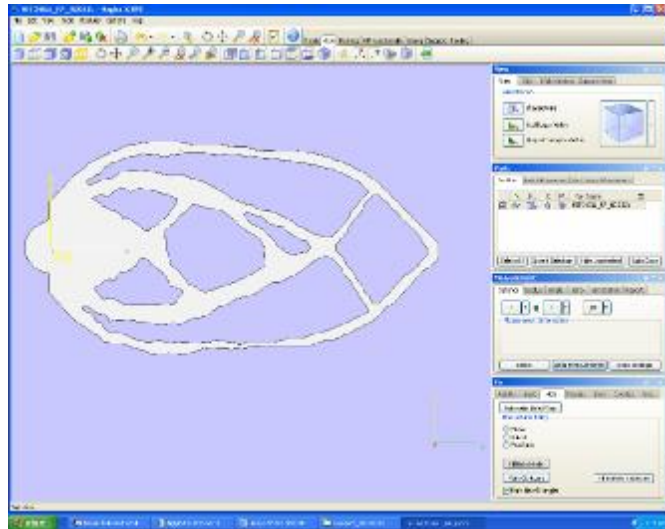
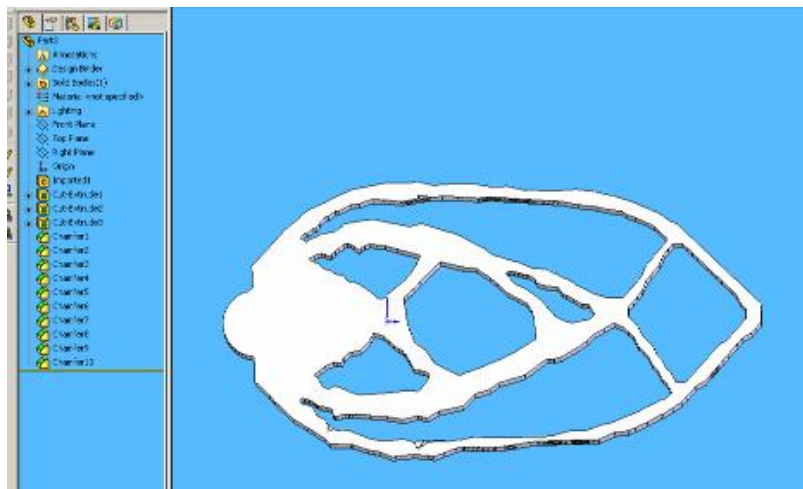


Figure 60: Geomagic point processing to make surfaces for this 2D part.



**Figure 61: Magics stl file fixing for RP process.**

Feature recognition in SolidWorks was used to create SolidWorks features from the STL file.



**Figure 62: Some of the features are recognized in SolidWorks**



**Figure 63: Final Mitchell structure made from Ti6Al4V powder using the EBM S12.**

An initial attempt at designing and building this structure using the EBM has been successful as shown in Figure 63. Additional post processing of the optimized file would be necessary to create a structure with integrity.

### **3.2. Mesh based optimization**

Many researchers have only considered the truss based optimization in 2D cases without considering the possibility of manufacturing the structures. Truss or beam based structures for optimization are defined to fill the part volume. During the optimization process, the nodes for the trusses or beams are moved and/or the thickness of the struts are changed to satisfy the constraints. The objective function could be to minimize the weight of a structure while maintaining a specified stiffness, specified displacements, or a maximum stress (Kirsh 1989; Rozvany, Zhou et al. 1992; Bendsoe 1995). There are many important papers which discuss different formulations, different cases, and algorithms for solving optimization problems (Kirsh 1989; Bendsoe, Ben-Tal et al. 1994; Cheng 1995; Rozvany 1996). Simple cases are formulated as linear programming problems and solved

with truss elements having only axial loading and no bending. Different formulations have also been used to achieve improved solutions. Cheng discusses the difficulties in formulating the structures and talks about the discontinuity issues (Cheng 1995). Customized procedures have also been used in structural optimization (Wang, Zhang et al. 2002). With more complicated constraints and multiple loading cases, approximate formulations or nonlinear programming have been used (Kirsh 1989). Some of the optimization algorithms are briefly discussed in the next section.

### **3.2.1. Updating Iterations: Optimization Methods**

The Method of Moving Asymptotes (MMA) is the most frequently used method in structural optimization problems (Bendsoe and Sigmund 2003). Svanberg suggested the method of moving asymptotes for structural optimization (Svanberg 1987). It is similar to Sequential Linear programming (SLP) and sequential quadratic programming (SQP) for solving smooth, nonlinear optimization problems. It creates convex approximate subproblems for each iteration and solves them by using a dual method or by an interior point algorithm. The solution to the subproblem is used to update the variables. Svanberg provides the algorithm upon request and it can be used in Matlab for different problem formulations.

Material cloud methods, Genetic Algorithms, Particle Swarm optimization, and Simulated Annealing are other methods to solve optimization iterations. Standard nonlinear optimization algorithms are provided in the Matlab toolbox.

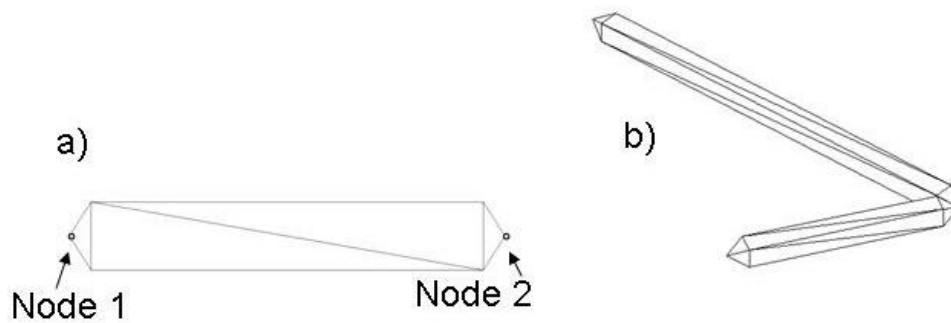
### **3.3. Optimized Mesh Structures**

Mesh based optimization was preferred over the homogenization approach because of better control and better produced parts.

#### **3.3.1. Design of structures**

Truss structures are very popular when designing lightweight structures with high stiffness. A non-stochastic mesh structure can also be considered to be a truss structure. When using Finite Element Analysis (FEA) to evaluate a truss structure, simple truss or beam elements can be used which allows for a more computationally efficient analysis. A truss element is a two- or three-dimensional element with two nodes that can only carry an axial load and has two or three degrees of freedom per node. A beam element also has two nodes and can be either a two- or three-dimensional element with three or six degrees of freedom per node, but the beam elements take into consideration bending as well. A three dimensional beam element allows each node to translate and rotate with respect to the X, Y, and Z axes. To perform an FEA on a truss structure, each truss is typically converted to a line element with two nodes in order to simplify the analysis. If optimization is used to improve a truss structure, the original structure can be designed using truss or beam elements directly. Once the optimization is completed, the two dimensional elements are converted into a structure with three-dimensional solid features to enable fabrication. For this research, MATLAB code was developed to convert the optimized structures into STL-files. Each truss or beam element has two nodes, each of which is connected to adjacent elements with the same node coordinates. With the node coordinates as apexes, a rectangular pyramid is created with a predefined height and base area. Four additional nodes are created, one in each corner of the pyramid base. The two

pyramids are connected with a rectangular prism, and a three-dimensional beam is created using a total of ten nodes. Beams with rectangular cross sections are used in order to greatly reduce the STL-file size for large structures. The cross section can be changed, however, as well as the cross sectional area. To finally generate the STL-file, each beam is divided into 16 triangular facets - eight for the rectangular prism and four each for the pyramids (Figure 64). The information for the triangular mesh is stored using the standard STL (ASCII) file format. To ensure that all the rectangular beams are interconnected, small cubes are added around each end node.



(a) Beam based on the two end nodes

(b) Two 3D beams connected at the end nodes

**Figure 64: a) 10 vertices are defined for each beam and 2 of them are actual nodal points. b) Two beams are shown without additional cube at intersection.**

Magics by Materialise (Belgium) was used to further enhance the STL-files prior to fabrication. Figure 65(a) shows a two dimensional truss beam that was modeled from simple truss elements and converted into an STL-file using MATLAB. The merge function in Magics was used to simplify the elements in each intersection, forming a more uniform structure (Figure 65b).

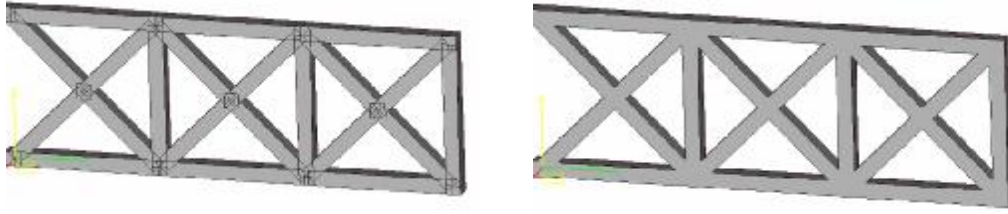


**Figure 65: a) Original STL-file of two dimensional truss beams constructed from FEA truss elements  
b) stl-file of simplified two dimensional truss beam**

Several two- and three-dimensional truss or mesh structures were designed using the above described process and converted into STL-files. The original designs were then optimized as described in the next section.

### 3.3.2. Optimization of structures

Truss elements and beam elements are used for shape and size optimization. Both unconstrained and constrained structural optimization examples are given below for different cases. Finite element analysis (FEA) was done in MATLAB, and the optimization toolbox was used for optimization iterations. Elements and nodes have been described for each structure, and constraints and forces are stored for each node's degrees of freedom. The basic FEA equations for beams are:

$$\{f\} = [K]\{D\}. \quad (1)$$

$$\{D\} = [K_{red}]^{-1}\{f\} \quad (2)$$

$$s_x^e = F_x^e / A^e \quad (3)$$

$$s_z^e = \frac{M_y^e * t_z^e}{2I_y^e} \quad (4)$$

$$s_y^e = \frac{M_z^e * t_y^e}{2I_z^e} \quad (5)$$

Here  $K$  is the global stiffness,  $D$  is the displacement,  $K_{red}$  is the reduced global stiffness matrix after applying boundary conditions,  $\sigma_x^e$  is the axial stress in element  $e$ ,  $\sigma_z^e$  and  $\sigma_y^e$  are bending stresses,  $M$  is the bending moment,  $t$  is the thickness,  $I$  is the moment of inertia, and  $F^e$  is the force in element  $e$  (Cook, Malkus et al. 2002). Element stiffness matrices are assembled into the global stiffness matrix after applying global coordinate transformations. Force and displacement components are linked by stiffness equations in global coordinates for all elements in equation (1). Displacement boundary conditions are used to modify the global stiffness matrix, and then displacements are calculated according to equation (2). The compliance of the structure is referred to as  $f^T D$ , where  $f$  is the force and  $D$  is the displacement. The axial stress for element  $e$  is calculated in equation (3), and bending stresses for beam elements are calculated in (4) and (5). Elements are assumed to have a square profile, and the volume is calculated as  $t^2 * l$ , where  $t$  is the beam thickness, and  $l$  is the length of the element.

The optimization objective is set to minimize the compliance for most examples under a single or multiple constraints. The basic formulation is

$$\begin{aligned} \text{Min } f^T D, \text{ subject to } f &= [K]D, \\ \sum_e V^e &\leq V \end{aligned} \quad (6)$$

, where  $V^e$  is the element volume and  $V$  is the volume threshold. The design variable is the node coordinates in all of the examples, and the beam thicknesses for one of the examples in this section.

The unconstrained optimization function in MATLAB based on Quasi-Newton line search was used to solve examples 1 and 2 described in the following section

(Papalambros and Wilde 2000). By using the Quasi-Newton line search method to update the Hessian matrices, an optimal solution can be found in less iteration. The Sequential Quadratic Programming (SQP) method was used to solve the examples with multiple constraints. It formulates Quadratic Programming (QP) subproblems based on approximations of the Lagrangian functions (Papalambros and Wilde 2000). It follows three main steps:

- ✓ Updating of Hessian matrix of Lagrangian function
- ✓ QP solution
- ✓ Line search and merit function calculation

SQP uses gradient information for each iteration calculated using finite differencing. Only related nodes and elements are recalculated, and the global stiffness matrix is updated only for the changing elements during the finite differencing instead of a full matrix recalculation. A list of moving nodes is constructed according to the loading, boundary conditions and non-moving nodes. Node points are moved in the search space using the given optimization method, and the program iterates through different solutions until convergence according to the optimization function. Full matrix calculations are done only in each major iteration. In the 3D cube with shear loading example, node movement and beam sizing cycles were performed to reduce material volume within the constraints. The program converged after completing beam sizing iterations that satisfied the constraints.

#### **3.3.2.1. Design optimization of a 2D cantilever**

The 2D cantilever problem has often been used as an example in structural optimization. The initial structure with loading at node 9 in the Y-direction and



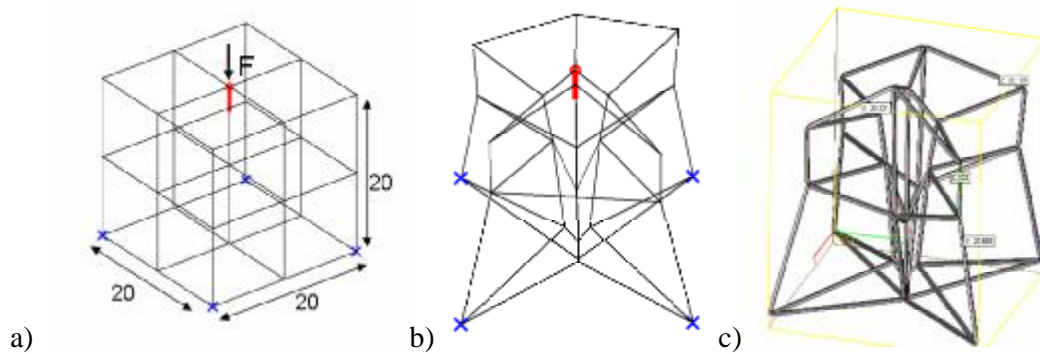


**Figure 67: a) Original 3D grid with dimensions of 20 x 20 x 20 mm b) Analysis output structure in 3D beams c) Output structure as STL-file format.**

### 3.3.2.3. 3D cube loaded in shear using variable beam thicknesses

The same 3D grid configuration was used to maximize the stiffness of the structure under a shear load of  $F=100$  N as shown in Figure 68(a). Axial stresses in the beams were constrained to  $\pm 500$  MPa. The output volume was constrained to be less than 60% of the initial structure volume. The lower limit for beam thickness was 0.6 mm and the upper limit was 2 mm. The initial beam thicknesses were 1 mm with a square profile. The Young's modulus was set to 1 MPa, and the Poisson's ratio was set to 0.3. Five nodes as indicated in Figure 68(a) are geometrically constrained. The optimization cycle was initiated by moving the unconstrained nodes and calculating the stiffness while complying with the constraints. The iteration cycle continued until no further improvement of the objective function was achieved while complying with the constraints. Then the beam thicknesses were altered until no further improvement in stiffness was achieved while complying with the constraints. Node movement cycles were completed in 35 iterations, and the beam sizing was completed in 10 iterations. The solution was assumed to have reached convergence when the relative change in the objective function was less than  $10^{-6}$  for three consecutive iterations.

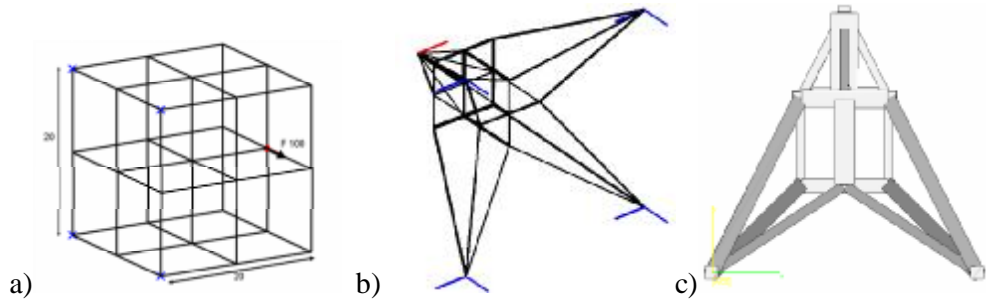


**Figure 68: a) 3D grid with the dimensions 20X20X20 mm b) Solution output structure in beam elements c) Output structure as STL-file format (Figures are not at same scale)**

The volume of the optimized structure was reduced from  $540 \text{ mm}^3$  to  $323 \text{ mm}^3$ , which was less than 60% of the initial volume. The compliance of the structure decreased from 5.65 to 0.706.

#### **3.3.2.4. 3D Rhombic lattice structure optimization**

In this example, mesh structures were optimized to simultaneously increase the stiffness and reduce the volume. The example has 2 rhombic unit cells in the X, Y, and Z directions as shown in Figure 69 (a and b). The beam thicknesses were set to 0.3 mm, and 3D beam elements were used for the analysis. The bottom nodes were fixed in all directions, and the top nodes were fixed in the X and Y directions while being subjected to a 100 N load in the Z direction. The geometric boundary of the structure was not limited. Node movements were done in the X, Y and Z directions using SQP in the MATLAB optimization toolbox. There were 160 beams and 78 nodes in the structure, and the total number of variables for the optimization was 210. This corresponds to 70 nodes each with 3 degrees of freedom. The iterations started at an infeasible point due to the volume constraint violation and continued until this constraint was satisfied or reached the predetermined maximum number of iterations.

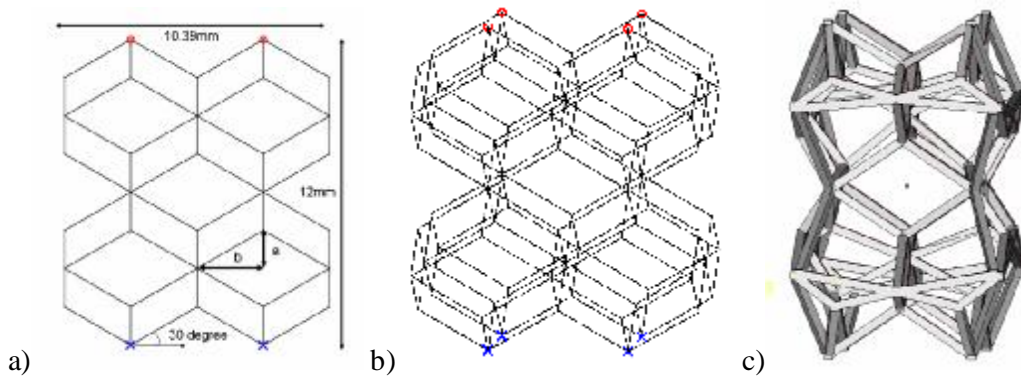


**Figure 69:** a) Overall dimensions of the structure are 12 mm in Z and 10.4 mm in X and Y, where  $a=1.5$  and  $b=a/\tan(30)$ , b) Input 3D lattice structure in MATLAB, c) Output 3D lattice structure in the STL-format

After 200 iterations, the volume violation approached zero ( $0.0008651 \text{ mm}^3$ ) resulting in the structure shown in Figure 69c. The initial compliance of 1425.29 was reduced to 115.25, and the volume was reduced by 20% as shown in Figure 70.

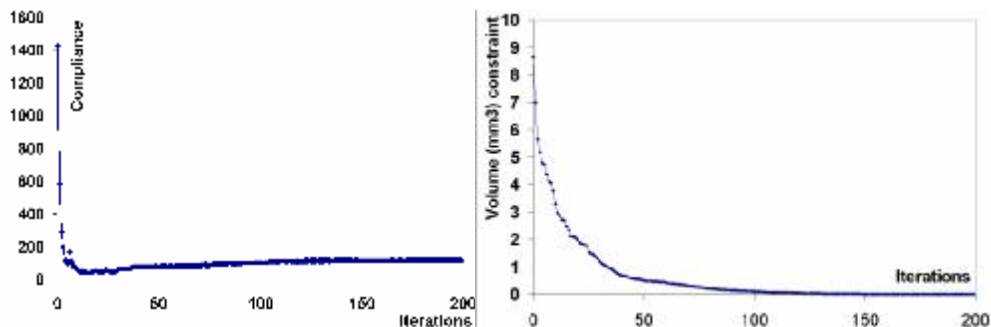


**Figure 70:** Compliance and constraint history of rhombic structures for 200 iterations

### 3.3.2.5. Hip stem

For this example, a hip implant cross section was meshed with triangular elements in ANSYS, and the vertex nodes were used to create the beam elements in MATLAB for FEA (Figure 71a). To demonstrate the possibility of optimizing a hip stem based on loading and boundary conditions, a 2D example is shown. The ultimate goal would be to match the bend stiffness of the stem to the bend stiffness of the proximal femur without

changing the original outer shape. Boundary nodes, loading nodes, and constrained nodes were restricted from movement. In this simple example, the free nodes were moved in the X and Y directions. A force of 100N was applied at the head of the stem. To be consistent with the previous examples the objective function was defined to minimize the compliance of the stem without moving boundary nodes. The compliance of the stem was reduced from 4.883 to 2.187 (Figure 71b). The original structure had a volume of 921 mm<sup>3</sup> (Figure 71c) while the optimized structure had a volume of 814 mm<sup>3</sup> (Figure 71d).

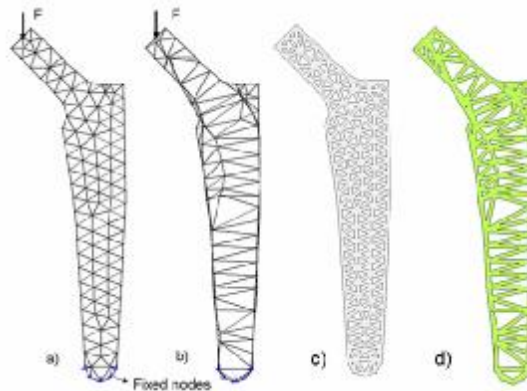


**Figure 71:** a) 2d cross sections for initial implant mesh b) after node movement cycle in 2d beam plots c) initial structure in Magics, and d) output structure in Magics

### 3.3.3. Fabrication of structures

In order to validate the optimization models, physical models were fabricated using the Stereolithography (SLA) and the Electron Beam Melting (EBM) processes. For this project, an SLA 190 was used to build the test structures using Somos 11110 resin (Figure 72 a). Metal Ti-6Al-4V structures were built using an Arcam EBM S12 machine. This titanium alloy is commonly used for both medical and aerospace applications. However, several commercial and experimental materials are also available for the process (Cormier, Harrysson et al. 2004; Cormier, West et al. 2005).

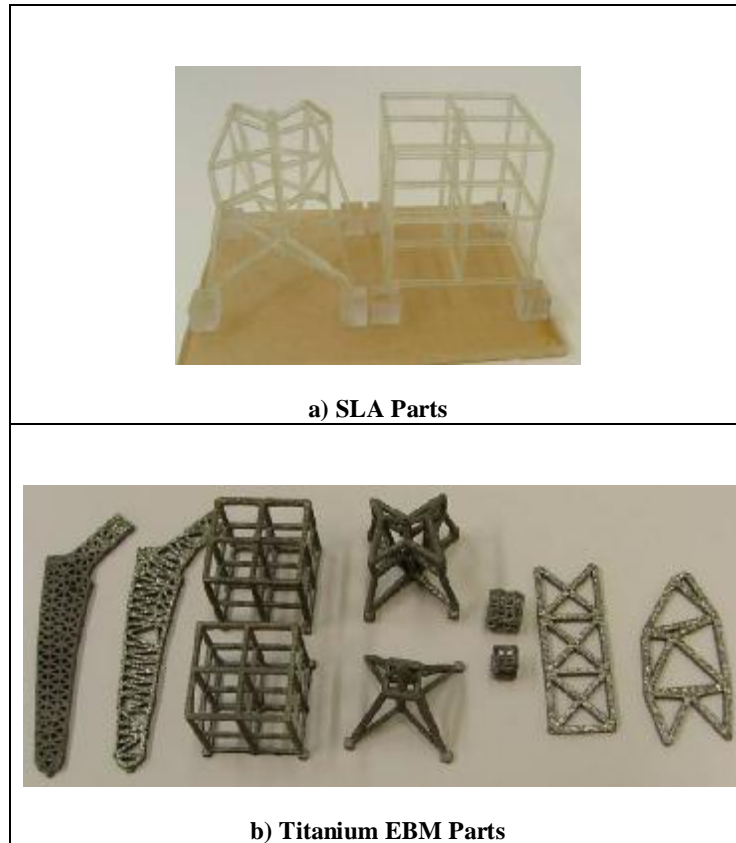


**Figure 72: Optimized and original structures fabricated using an SLA 190 and EBM**

### **3.3.4. Testing of structures**

Stiffness/compliance values for the structures produced via the SLA and EBM processes were measured using an ATS 1605C universal testing machine. For the SLA structures, a 113.4 Kg (250 lbs) load cell was used with a crosshead rate of 1.27 mm/min (0.05 in/min). The metal structures were tested at the same crosshead rate, but with a 2268 kg (5,000 lb) load cell. As shown in Figure 67(a), the grids designed for compression were loaded solely at the top center node. The grids designed for shear loading were loaded at the center node as shown in Figure 68(b). Stiffness/compliance values for the original and optimized rhombic structures were obtained using the same testing machine. The crosshead rate was 0.254 mm/min (0.01 in/min). The load was distributed over the top surface of the cell structures using steel parallel plates.

As can be seen in Figure 73, Figure 74, and Figure 75 the optimized structures show an increase in stiffness over the original 2D and 3D structures. The EBM fabricated structures had beam thicknesses that were different from the CAD-models so FEA ratios were recalculated based upon the actual EBM beam thicknesses. Results are compared in Table 10.

**Table 10: Compliance ratios in testing and FEA for updated coordinates and thicknesses**

Structure	Measured Ratio	FEA Ratio
2D grid; EBM	1.42	<b>1.40</b>
Cube grid 1 compression, EBM	2.52	<b>3.7</b>
Cube grid 1 compression, SLA	7.02	<b>6.24</b>
Cube grid 2 shear, EBM	3.73	<b>7.99</b>
3D Rhombic Meshes	1.71	<b>4.44</b>

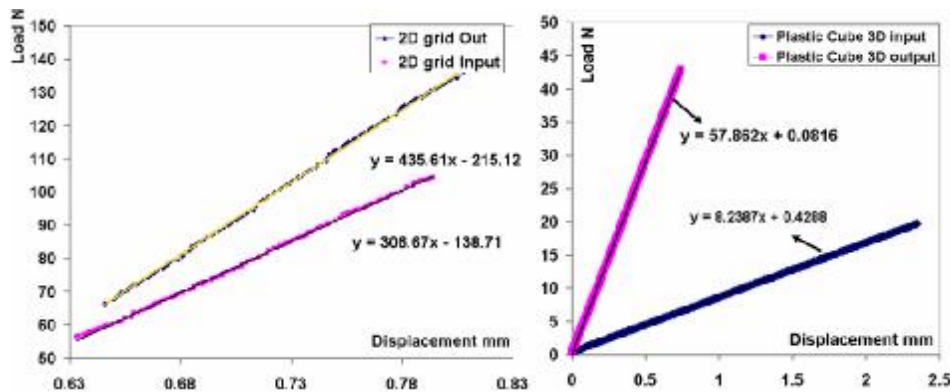


Figure 73: a) 2D grid, EBM part, original versus optimized structure is shown optimized/original stiffness ratio 1.42 b) Plastic 3D grid optimized/original stiffness ratio 7.02

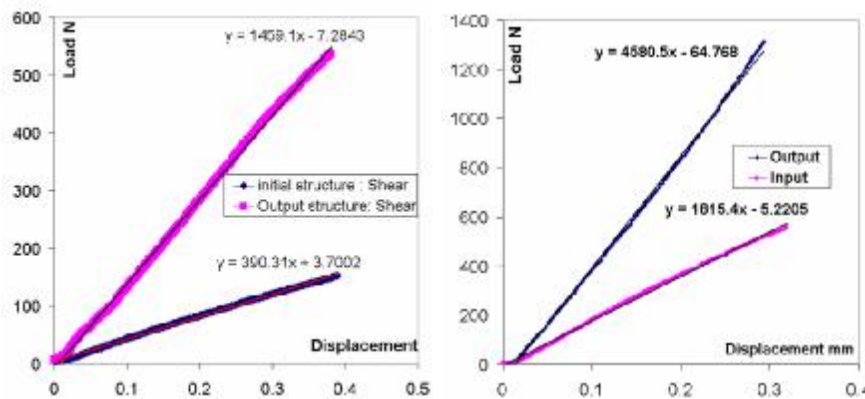
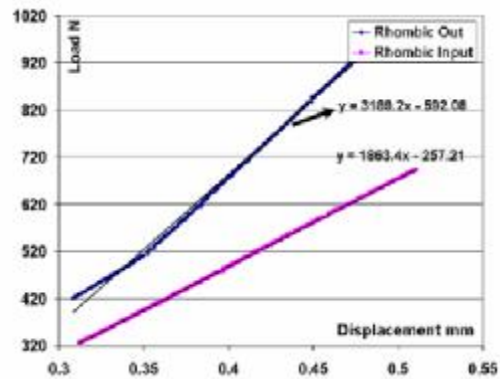


Figure 74: a) Cube grid 2, EBM part, for loading in x direction (shear) ratio is  $1459.1/390.31=3.73$ . b) Cube grid 1, EBM part, in compression loading ratio is 2.52 (beams are ~2mm)



**Figure 75: Load and displacement after structures contacted the loading plates entirely. Optimized over original stiffness ratio is 1.71.**

### 3.3.5. Discussion

Most structural optimization research in the past has been carried out using 2 dimensional example structures due to the limitations set by the available computing power. Optimization of 3-dimensional structures can efficiently be done using beam elements, and the resulting structures can be converted into solid structures using the previously described approach. Topology optimization might seem to be more suitable for 3-dimensional structures but it is difficult to guarantee the integrity of fabricated structures using a layered approach. When using topology optimization, the resulting structure is often very similar to a truss structure or something that can be approximated by one. The simplicity of the beam elements makes it possible to efficiently use them to optimize the geometry of large and complex structures. Multiple objectives often need to be satisfied while complying with a set of both geometrical and physical constraints. Future work would include the development of programs to handle such complex 3D structures as hip stems.

Most layered manufacturing technologies suffer from anisotropic material properties. Many such technologies exhibit lower strength in the Z-direction than in the

X- and Y-directions. This is not the case with the EBM process due to the full melting of each layer. However, when thin beams are built at an angle, each layer of that beam consists of a relatively small cross-section that is slightly shifted from one layer to the next (Figure 76). If the angle between the build plane and the beam is too small, the overlap between each layer is minimal and the strength of the structure becomes highly compromised. When optimized beam structures are fabricated using the EBM process, it is therefore to be expected that the structures will have lower strength than what the FEA predicts. Part of the present research effort aims to quantify properties of extremely thin layered structures and to enhance the process for such geometries.

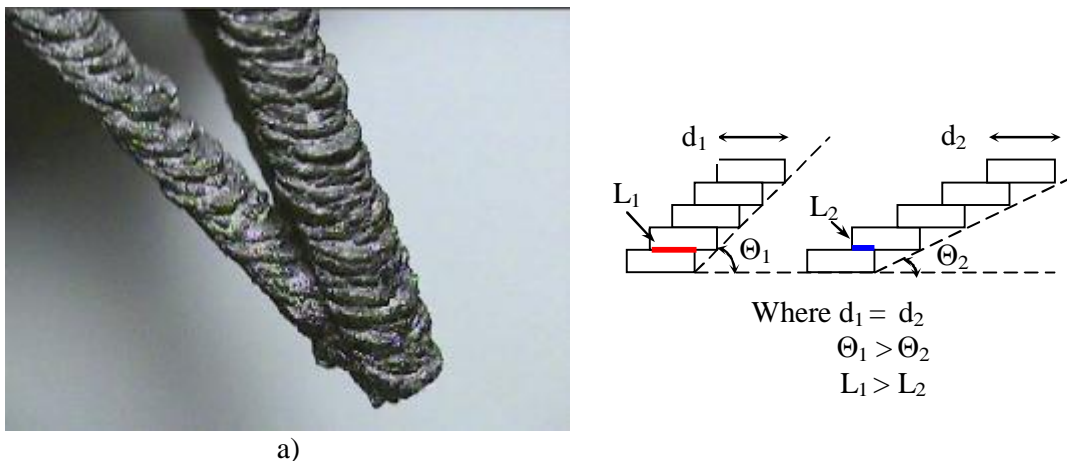


**Figure 76: a) A thin low angled beam structure fabricated using the EBM technology b) effect of low build angle on thin beam structures structure**

The overall feature size of the 3D rhombic mesh structures was too small to completely replicate the details with the EBM process, and the test results differed from the calculated FEA ratios. When beam intersections were merged in Magics, the overall stiffness changed due to the reduction in node movement. There is a difference between the actual dimensions of the fabricated EBM structures and the CAD structures. In addition, the thicknesses of the beams are somewhat dependent on their orientation in the

build space which will also affect the structural stiffness. To fully evaluate the differences between the FEA results and the actual results, a larger number of samples need to be included.

### **3.3.6. Conclusion**

Preliminary examples of 2D and 3D shape and size optimization have been shown in this section. Structures were designed using beams or trusses to represent the design volume with fewer elements. A Quasi-Newton method was used to optimize unconstrained structures and Sequential Quadratic Programming was used for multiple constraint optimizations. The results were converted to STL-file format and fabricated using SLA and EBM technologies. The structures were tested and the results were compared to the updated FEA models. The results presented here can be used to develop scaling factors for future structures, but testing of larger sample groups will be needed. For future work, a full 3D optimization of hip stems will be conducted, fabricated and tested.

## **4. DESIGN AND FABRICATION OF HIP STEMS**

A significant body of research has focused on improving the durability of hip implants. New materials have been studied to reduce the wear rates. Cementless implants have been used to reduce implant loosening. Alternative implant designs have also been considered to produce more effective stems with less micromotion in the short term and less stress shielding in the long term. Composite stems have been used and one of them has been recently approved by the FDA. Modeling has also been used to assess the performance of the implants. The hip implant systems section below provides background information about hip implants and includes examples of studies in different areas of hip implant systems.

### **4.1. Hip implant Systems**

Hip implants are used to control hip pain resulting from primary or secondary hip disease, including cartilage wear, bone spurs impinging on bone surfaces, and thickened hip joint capsule. Hip implants are not the only therapeutic option in chronic hip pain. A more natural option is cartilage replacement. However, cartilage replacement is still in its infancy. Tissue engineering has been used, but cell selection, scaffold design, and biological stimulation are the current challenges of cartilage replacement. Success of the cartilage replacement depends on improvements in tissue engineering (Kuo, Li et al. 2006). Surface replacement options were tried before and are popular again in some special situations. Drugs are used to control pain adequately, improve function, and reduce disability, when applicable. Acetaminophen is frequently used for symptomatic OA with mild to moderate pain. Nonsteroidal antiinflammatory drugs (NSAIDs) are more

effective in the case of moderate-severe pain, but they have an increased risk of adverse effects (Sarzi-Puttini, Cimmino et al. 2005). Hip implants are made using a variety of materials that have been developed to improve the stability and durability of the implant. However, all the materials used in a total hip replacement have four characteristics in common: biocompatibility, resistance to corrosion, degradation, and wear, and they meet the highest standards of fabrication and quality control at a reasonable cost. Implant systems can be analyzed according to the type of materials. Hard bearing surfaces have been researched with different combinations for total joint replacements such as ceramic-on-ceramic, metal-on-metal, metal-on-plastic, and ceramic-on-plastic. Reported clinical wear rates for different combinations are included in Table 11.

**Table 11: Material combinations and wear rates. SOURCE : (Semlitsch and Willert 1997)**

Femoral Head	Acetabular cup	Wear Rate ( $\mu\text{m}$ )/year
Metal	UHMWPE	100-300
Ceramic	UHMWPE	50-150
Metal	Metal	2-20
Ceramic	Ceramic	2-20

Development and testing of new materials are costly due to the trials needed to prove the effectiveness and safety of the system. New materials and combinations, however, are introduced in the marketplace with a lag time of 5 to 10 years between basic research and commercialization.

Cementless implant systems have also been studied to avoid the implant loosening problems. With cemented implants, acrylic cement provides flexibility in the fixation of the implant for different shapes of the femora. Cemented implants also allow faster

rehabilitation in contrast to cementless implants. A stable interface between the prosthesis and the cement and a solid mechanical bond between the cement and the bone are important factors for cemented fixation. Cracks (fatigue fractures) in the cement that may occur over time can cause the prosthetic stem to loosen and become unstable. Small wear and cement particles absorbed by cells around the bone cement interfaces may also initiate an inflammatory response from the body, which tries to remove the cement. With this inflammatory response, cells may resorb varying amounts of bone around the cement surfaces. This process is named osteolysis. Implant failure occurs with the continuation of bone loss around the bone-stem or bone-cup interfaces. Cemented THR is more stable in patients over age 60, who are less likely to place high stresses on the cement which can lead to fatigue fractures. Another advantage of the cemented technique is the ability to incorporate antibiotics into the cement during revision surgery of the following periprosthetic infection (Nelson 2002). Fixation of implants with cement is still popular with successful long term results. Callaghan et al. reported follow up studies at 25 years of Charnley total hip arthroplasties performed with cement (Callaghan, Albright et al. 2000). The overall success rate was high and 90% had retained the original implants. Fourteen revision surgeries had been performed among 62 hips of patients who were alive more than 25 years postoperatively. Three of the revision surgeries were done because of loosening with infection and eleven of them were done due to aseptic loosening. High shear and compressive stresses may result in failure at bone-cement-stem interfaces. Ramaniraka et al. evaluated the micromovement and stress levels at the bone-cement interfaces for titanium and a cobalt-chromium stems (Ramaniraka, Rakotomanana et al. 2000). For a range of cement thicknesses, micromovements were measured at the bone-cement interface. It is shown that the thickness of cement affects stress levels and micro

movements. A 2-mm-thick cement layer was observed to increase shear stress proximally and increased micromovement over the interface. Both implant types had high slipping and high proximal shear stress. High slipping results in the generation of cemented debris which leads to osteolysis (Willert, Bertram et al. 1990).

Cementless fixation has been suggested because cement has been reported to be the cause of aseptic loosening (El-Warrak, Olmstead et al. 2004). Cementless implants are textured or coated with different porous materials for bone ingrowth. Because they depend on the new bone growth for stability, cementless implants require a longer healing time than cemented replacements. Intimate contact between the component and bone is crucial to permit bone ingrowth. New bone growth cannot bridge gaps wider than 1 to 2 mm. A 6- to 12-week period of protected weight bearing (using crutches or a walker) is needed to give the bone time to grow onto and into to the implant. This protected weight bearing helps to ensure there is no excessive movement between the implant and bone, so bone ingrowth can occur. Cementless stems can loosen if a strong bond between bone and stem is not achieved. Although some surgeons are now using cementless devices for all patients, cementless THR is most often recommended for younger (under 50 years of age), more active patients, and patients with good bone quality where bone ingrowth into the components can be predictably achieved.

Quality of initial fit is important in cementless implants. Micromotion most often results in failure. Engh et al. evaluated 307 patients after two years and 89 patients after five years for porous coated hip replacement (Engh, Bobyn et al. 1987). Eleven retrieved specimens showed bone ingrowth and fibrous tissue fixation. In the clinical study, 259 cases (84%) had fixation by bone ingrowth, 42 cases (13%) had stable ingrowth with fibrous tissue, and 7 cases (2%) were determined to be unstable. It was concluded that a

tight fit at the isthmus of the femur is necessary to have better bone fixation. They suggested that if the stem fills the medullary canal, that the prognosis will be good for bone ingrowth. A good press fit was also observed to decrease the pain. Radiographically, 88% of the cases showed little stress shielding with small diameter stems. They also reported that larger diameter stems are most likely to cause more bone loss by stress shielding in an another study (Engh and Bobyn 1988). Ramamurti et al. studied factors affecting the bone ingrowth (Ramamurti, Orr et al. 1997). Stability of the bone implant interface was considered to be affected by motion of the implant, friction, degree of press fit, and modulus of the surrounding bone-stem interface. Nonlinear and linear finite element models were used to simulate the post-surgical conditions. Different coefficients of friction, press fit, and modulus parameters were used in the analysis. Displacement of the implant at the interface was changed to observe the relative slip at the bone-implant interface. For slight press-fit conditions, relative implant slippage was observed below 20 microns of implant displacement. For higher friction parameters and higher degrees of press-fit conditions, no slip was observed during implant displacements as much as 100 microns.

Wear and implant bone interfaces are important factors in the long-term success rate of the THR. Stress shielding is also important in bone resorption and each of those may cause the eventual loosening of the implant, which means painful hip replacement surgery with low success rate (Gruen, McNeic et al. 1979). Bone adapts to mechanical conditions by adding bone mass as a result of loading and resorption as a result of unloading. This suggests that the body senses changes in sustained mechanical load patterns and adapts itself to carrying loads in a most efficient way relying on minimal

bone mass. However, bone resorption is poorly understood at the cellular level. Our current knowledge of bone remodeling incompletely explains stress shielding.

## **4.2. Bone remodeling**

Bone is a living tissue. Remodeling mechanisms restore the micro damage of bone surfaces and allow the bone to adapt to changes in loading patterns. Remodeling maintains the overall strength and prevents early deterioration. There are three types of cells that are found only in the bone: osteoclasts, osteoblasts and osteocytes. '*Osteo*' means bone in Greek. Bone resorption and bone formation are linked and occur in the body as part of the remodeling process (Klein-Nulend, Bacabac et al. 2005).

Osteoclasts are large multi-nucleated cells, typically 20 to 100  $\mu\text{m}$  in diameter. They are formed by the fusion of the mononuclear progenitors of the macrophage family (Teitelbaum 2000). These cells are responsible for bone loss. They are found on the surface of the bone next to dissolving bone. Osteoblasts are nucleated cells that produce new bone. They also come from the bone marrow. They work in groups to build bone. They produce a bone-like material named "osteoid" that is made of bone collagen and other proteins. Then, they control calcium and mineral deposition. Inactive osteoblasts become flat and line the surface of the bone. These old osteoblasts are named lining cells. They regulate displacement of calcium into and out of the bone, and they respond to hormones by making special proteins that activate the osteoclasts. Lining cells also appear to control the regulation of the bone fluids (Miller, de Saint-Georges et al. 1989). Ducky et al. reviewed the osteoblast differentiation and functions in detail (Ducky, Schinke et al. 2000).

Osteocytes are cells inside the bone. They also come from osteoblasts. They are connected to the other osteocytes with long ramifications. Osteocytes react to loads or cracks in the bone and help to direct osteoclasts. Osteocytes are believed to play an important role in transporting minerals and sensing mechanical stimuli (Cowin, Moss-Salentijn et al. 1991). Different aspects of the bone remodeling process have been studied such as cell-to-cell interactions (Stains and Civitelli 2005), phenomenological models (Moroz, Crane et al. 2006), mechanobiology of the bone tissue (Klein-Nulend, Bacabac et al. 2005), effects of genetics, osteocytes, and interstitial fluid flow in mediating disuse (Suva, Gaddy et al. 2005). Models have been used to simulate bone for different situations. A short review of bone remodeling is necessary to discuss future work related to this thesis.

#### **4.2.1. Bone Remodeling Models**

Mathematical models of bone remodeling are of great interest to future research work. Lemaire et al. proposed a mathematical model explaining the interactions between osteoblasts and osteoclasts, two cell types specialized in the maintenance of bone integrity (Lemaire, Tobin et al. 2004). Fernandes et al. developed a microstructural model of the bone ingrowth process with the ability to modify the contact conditions during the remodeling process (Fernandes, Folgado et al. 2002). A global optimization criterion was used with a contact formulation as a method to detect bone ingrowth. Trabecular bone was modeled with repeating prismatic cells. A homogenization method, which will be discussed below in the microstructure design section, was used to compute elastic properties. The structural stiffness and metabolic cost were optimized. The necessary conditions are derived using Lagrange equations and modified at each iteration based on

displacements at the bone-stem interface. This is tested for different coating extents and locations on the stem. Initial conditions were friction contact if the surface is coated and zero friction otherwise. Fifty microns was determined as a threshold value to decide if the displacements were small enough for a bonded contact instead of a friction contact. The results showed that bone ingrowth occurred over 20% of the coated surface, a result similar to clinical observations.

Huiskes et al. developed a mathematical model for bone remodeling considering the mechanic and biological activities (Huiskes, Ruimerman et al. 2000). It was a very detailed study of biological level interactions. Ruimerman et al. developed 3D FEA models and used them to simulate the development of trabecular bone (Ruimerman, Hilbers et al. 2005). They have reported mechanisms that result in optimal stress transfer. Trabecular thickness was decreased with a reduction in load.

In many studies, bone has been considered to be optimal under the given loading conditions. However, responses are slow to have the exact optimal structure. Bagge et al. considered bone adaptation as an optimization process and formulated a remodeling rate equation including a delay in adaptation and anisotropic material properties (Bagge 2000). The architecture of cancellous bone was designed with cubic microstructures. The optimization problem of minimizing the total bone strain energy was solved using the optimality criteria method in multiple loading. The loading memory was used to reflect the delay in the adaptation process. Change in the bone structure was limited at a 7.6%/yr bone turnover rate (i.e., total bone loss of 100% in 13 years). Optimization was started in a uniform relative volume distribution. A compact shaft and a more porous structure of cancellous bone were observed in loaded areas.

Bone remodeling has also been studied with different methods. Kroger et al. studied periprosthetic bone loss and regional bone turnover in uncemented total hip arthroplasty by using high resolution single photon emission tomography and dual-energy X-ray absorptiometry (Kroger, Vanninen et al. 1997). Bone loss has been observed in the lesser trochanter region, near the femur head, and it was related to the bone remodeling due to the new stress distribution. It is possible to use mathematical models in the stress analysis of custom designed implants.

### **4.3. Designs to prevent stress shielding**

Insertion of a relatively stiff titanium or Co-Cr stem generally changes the loading pattern around the bone. Engh et al. reported that thick stems resulted in a five fold increase in incidence of bone resorption compared to thin stems (Engh and Bobyn 1988). Huiskes et al. reported that flexible materials reduce stress shielding and bone resorption, however, they increase interface stresses between the implant and bone (Huiskes, Weinans et al. 1992). The reduction in the loss of cortical bone mass with reduced stem stiffness has been shown in several animal studies (Maistrelli, Fornasier et al. 1991; Bobyn, Mortimer et al. 1992; Turner, Sumner et al. 1997). Different designs and manufacturing techniques have been used to address the issue of stress shielding by considering flexibility and interface properties.

#### **4.3.1. Different geometric designs**

Surface replacements were used in the 1980s but failed in design. New types of stemless prostheses were designed in the 1990s (Munting and Verhelpen 1995; Shih,

Chen et al. 1997). Tai et al. created 3D finite element models for intact femur, cervico-trochanteric implanted femur (stemless implant) and porous-coated anatomic implanted femur as seen in Figure 77 and Figure 78 (Tai, Shih et al. 2003). Analysis was performed for a loading condition simulating a single-legged stance. The Von Mises stress distributions of each model were analyzed and compared. Convergence tests were performed for different numbers of elements and nodes as seen in the Figure 78.

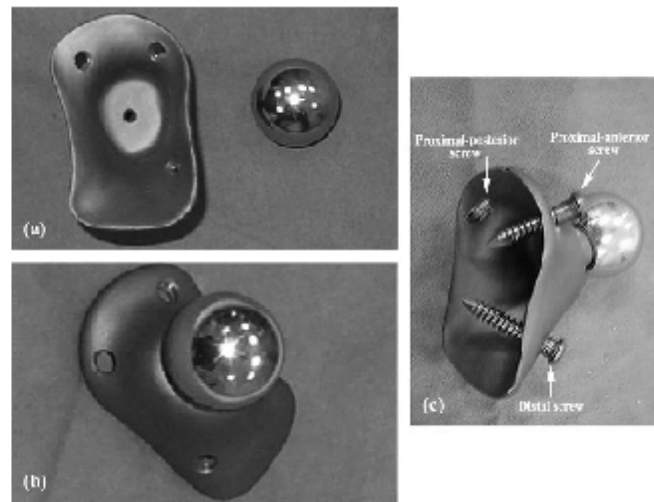


**Figure 77:** A cervico-trochanteric prosthesis: (a) inner side, (b) outer side, and (c) configuration with three screws. Source: (Tai, Shih et al. 2003) with permission from Elsevier.

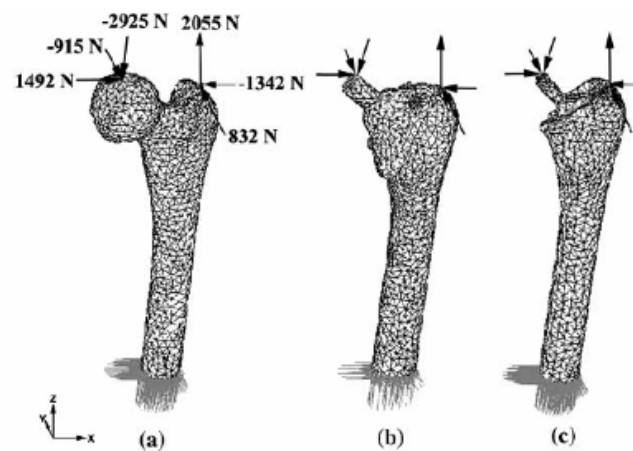


**Figure 78:** The loading configuration of generated 3-D finite meshes for the (a) intact, (b) C-T, and (c) PCA implanted femora. Source: (Tai, Shih et al. 2003) with permission from Elsevier.

Small changes in stem geometry have been analyzed. Mann et al. also used 3D finite elements to analyze the stress levels of Charnley and Distal-Round stems for a proximal stem-cement bonded interface and for a fully debonded interface as seen in Figure 79 (Mann, Bartel et al. 1997). The stem has been removed to reveal the inner

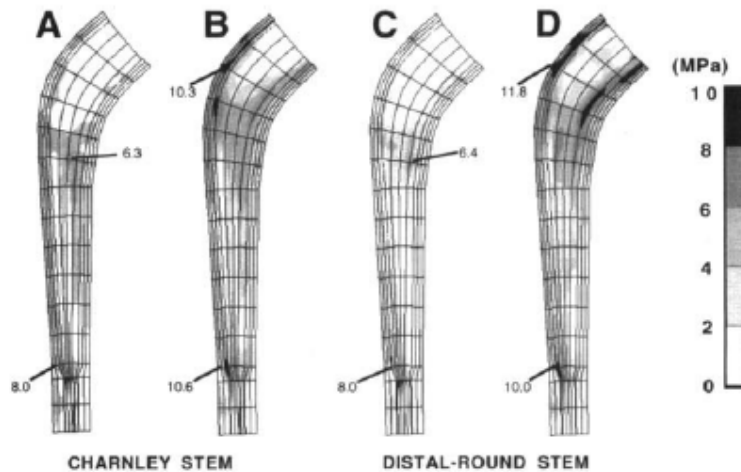


**Figure 79 : Maximum principal stresses within the cement mantle for the Charnley stem with a proximal bond (A), Charnley stem without a proximal bond (B), Distal-Round stem with a proximal bond (C), and Distal-Round stem without a proximal bond (D). Source: (Mann, Bartel et al. 1997)**

concave surface of the anterior portion of the cement mantle. The maximum principal stresses in the cement were substantially higher when there was not a proximal bond, and were highest for the Distal-Round stem without a proximal bond.

Collars and collarless implants have been studied for differences in stress transfer (Whiteside, Amador et al. 1988; Prendergast and Taylor 1990; Settecerri, Kelley et al. 2002). Collars are typically flat, as shown in Figure 80, and are designed to provide a path for direct axial stress transfer from the prosthesis to the proximal femur. Stems tapered from proximal to distal in one or more planes are called collarless. In the collared designs, it is difficult to achieve and maintain calcar contact for direct axial stress transfer, and

seating at the collar can prevent full insertion of the prosthesis (Settecerri, Kelley et al. 2002). Collarless designs have been criticized because of potential over-insertion and the possibility of excess micromotions. Mandell et al. studied conical-collared intramedullary stems to improve the stress transfer with limiting micromotions (Mandell, Carter et al. 2004). Three dimensional FEA was used to compare straight-stemmed, axisymmetric prostheses: flat-collared ( $0^\circ$ ), conical-collared ( $30^\circ$  and  $60^\circ$ ), and collarless tapered ( $80^\circ$ ) as shown in Figure 80. Axial loading and non-axial loading were used with and without bone ingrowth. Results showed that there is a tradeoff between initial stress transfer and micromotion with the selection of collar angle. Stems with conical collar angles in the range of  $30^\circ$ – $60^\circ$  resulted in increased stress transfer compared to a flat collar design, and reduced micromotion compared to a collarless tapered design.

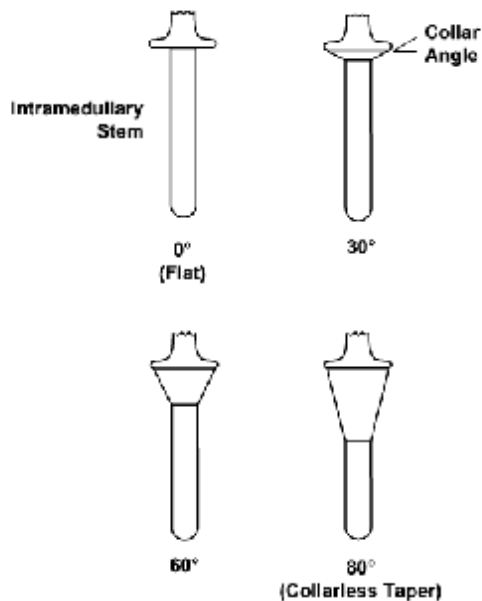


**Figure 80: Progression of flat-collared, conical-collared, and collarless tapered stem designs. Source: (Mandell, Carter et al. 2004), with permission from the author.**

The deformed shape of the model, stresses, strains and strain energy density (SED) within the proximal bone, bone-implant interface stresses, and micromotion, were compared for different implant models. They concluded that bone ingrowth over an extensive proximal region reduces the effect of collar design on stress transfer and micromotion.

Hollow stem designs were also considered to adjust the stiffness of the stem at different levels. Gross et al. developed cylindrical simple hollow stems (Gross and Abel 2001). The analysis of the hollow stems revealed reduced stress levels. Some of the designs used in the study are show in Figure 81.

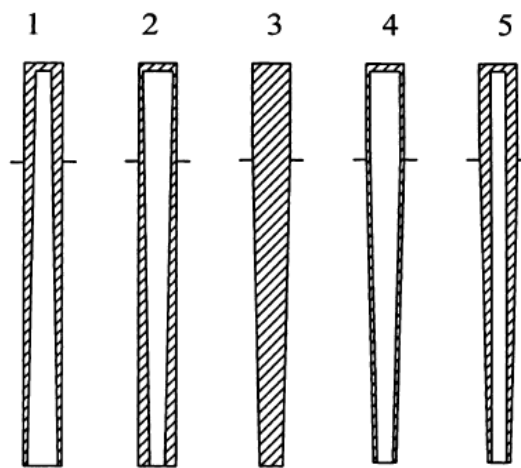


**Figure 81: Simple stem designs for less stress shielding. Source:(Gross and Abel 2001), with permission from Elsevier.**

Different geometries have been considered in terms of filling the femoral canal. A fit-and-fill algorithm has been commonly used to design stems, which aims to maximize contact between prosthesis and cortex in priority areas for better stability (Poss, Walker et al. 1988). Fit-and-fill designs may result in early torsional instability and micromotion due to the differences in femur geometries. In 1979, Karl Zweymuller implanted the first cementless, tapered, rectangular cross-sectioned femoral component of his design as seen

in Figure 82. It has been reported to have axial stability through a dual longitudinal taper and rotational stability through cancellous bone compaction. Primary stability is provided by contact between the cortex and corners of the stem. Secondary stability is achieved by osseointegration to the grit-blasted titanium aluminum-niobium surface (Swanson 2005). Bone and blood supply are conserved with the fit without fill concept. Seven hundred thousand tapered rectangular stems have been implanted since 1979 (Swanson 2005).



**Figure 82 : Modern tapered rectangular press fit design of Zweymuller (SL-Plus, Plus Orthopedics AG, Rotkreuz, Switzerland). Source: (Swanson 2005), with permission from Elsevier.**

#### **4.3.2. Composite stems**

Composites have been considered as well to reduce implant stiffness without decreasing stem strength. In general, FEA models were used to predict the failure of composite stems, which is different and dependent on ply orientation, stacking sequence, manufacturing process, and overall geometry. Composite stems, regular laminated composites, have been manufactured to verify the FEA models. To our knowledge, there is no published study modeling bone ingrowth of the composite stems. Composites without lamination have also been manufactured and tested. Early results of composite

stems show high failure rates (Jakim , Barlin et al. 1988; Ritter, Keating et al. 1990; Au 1994; Niinimaki, Puranen et al. 1994; Niinimaki and Jalovaara 1995; Adam, Hammer et al. 2002). Isoelastic stems, made from lower modulus material, polyacetal by R. Mathys', has poor primary fixation and resulted in early subsidence. Inferior surface characteristics or incompatibility of polymer with tissue were other factors affecting the failure of implants. There are composite hip stems on the market. Zimmer (Warsaw, Indiana) has a composite hip stem called EPOCH that has been sold in Europe for approximately eight years. It has a forged cobalt-chromium-molybdenum core section. The outer layer is a commercially pure titanium fiber metal section applied over a polyaryletherketone (PAEK) middle section. The layer of PAEK is injection molded onto the metallic core. The fiber mesh with an effective thickness of around 0.83mm is attached to the polymer at injection molding<sup>5</sup>. The mesh covers the polymer up to the shoulder of the stem. The average pore size is around 300µm. The mesh is covered with a ceramic coating of 70µm thickness. The coating is 65% HA with some tricalcium phosphate. This stem was in the 6 year multicenter clinical trial in United States and received a 510k clearance in 2002 from the FDA.

Karrholm et al. evaluated the EPOCH stems and anatomic stems in a follow up study (Karrholm, Anderberg et al. 2002). EPOCH stems were reported to achieve good primary fixation with less proximal bone loss of bone mineral density. Sixty-five patients were included in the study and 34 of them were followed with dual energy x-ray absorptiometry.

---

<sup>5</sup> [www.zimmer.com](http://www.zimmer.com)

Different combinations of materials have been used for composites in laminated versions and some of them will be discussed below. Sumner et al. used two different stem stiffnesses with identical geometry and porous coating regions (Sumner, Turner et al. 1998). The high stiffness stem resulted in 26% cortical stress shielding, versus 7.5% for the low stiffness stem. A unidirectional carbon fiber central core was inserted into polyaryletherketone for the low stiffness stem. Commercially pure Ti fiber metal porous coatings (1.5 mm thick) were used on the surface of the stem faces. The titanium porous coating and plastic were joined using heat staking, which locks the protruding feature from one component into a second component through the cold flow or melting of the plastic. The high stiffness stem was a titanium alloy (Ti6Al4V) with diffusion bonded porous surfaces. They were identical in cross section and shape.

Zhang et al. tested the long-term compressive properties of carbon fiber reinforced polyetheretherketone (PEEK) composite femoral components (Zhang, Latour et al. 1996). Since their compressive properties are generally lower than their tensile properties, compressive properties of 0°/90° angle composites in saline solution at different temperatures were tested. Results showed that ultimate compressive strength, modulus, and Poisson's ratio were not affected by the stability of the material.

Scotchford et al., 2003, investigated the human osteoblast-like cell and macrophage responses to carbon fiber reinforced PEEK. Osteoblast attachment was observed to be similar to Ti6Al4V (Scotchford, Garle et al. 2003).

Katoozian et al. used reinforced fiber composites for hip implants (Katoozian, Davy et al. 2001). Two objective functions were defined based on interface failure and bone remodeling. Numerical optimization of the bone implant system with the sum of Von Mises stress (VMS) as the objective function was used. Adaptive response of the

bone was considered with the stress shielding ratio, which is the ratio of equivalent stress at normal bone to implanted bone. A ratio equal to 1 means that the implant system is similar to the natural state. Bone loss,  $F_2$ , and mechanical failure potential,  $F_1$ , were included in the objective with stress shielding ratio as follows:

$$F_1(X) = \sum_{i=1}^N s_i^2, F_2(X) = \sum_{i=1}^N (h_i - 1)^2, h_i = \frac{s_i}{s_{ni}}, \text{ where } h_i \text{ is the stress shielding}$$

ratio at point I,  $s_i$  is the VMS at point i,  $s_{ni}$  is the same quantity in normal bone, and N is the number of elements. Optimization procedures found fiber volume fraction and angles to minimize F1 and F2 separately. CT scan data was used to construct an FEM mesh. A single loading condition was used in this study. Three components of the forces were adapted from the terminal stance phase of horizontal walking. The overall results showed the effectiveness of the technique and possibility to design a composite stem with stress patterns similar to natural bone.

Chang et al. designed a composite stem by selecting the proper ply orientation and stacking sequence for thin layers of composite (Chang and Perez 1990). Composites were claimed to have high strength and low stiffness. The important factors in composite stem design were fabrication process, machining, ply orientation, and stacking sequence. Tsai-Hill failure criterion and delamination failure criterion were used for in-plane failure and out-of-plane delamination respectively. Analytical equations were tested for a simplified L shape stem geometry in 2D with thickness. Graphite/epoxy was used, due to its well known curing parameters. Specimens had nearly linear stress-strain curves up to failure. Some of the stems failed due to the ply orientations and stacking sequence. Different ply orientation and stacking sequences were tested to determine failure load. It was suggested

that 3D FEA using the actual implant configuration is needed for optimal composite stems.

Mckellop et al. compared the displacement in cemented Muller, Spotorno stem (Protekal AG Sulzer, Bern, Switzerland) , press fit Muller, composite stem with modulus around 60GPa, and Austin Moore stems under the same loading (Mckellop, Ebramzadeh et al. 1991). Each stem was placed into synthetic femurs according to the manufacturers' recommendation. Composite stem displacement was close to press fit Muller and cemented Muller.

Kaddick et al., 1997, developed a FEA model for composite failure modes (Kaddick, Stur et al. 1997). The experimental results were compared with FEA results and they reported that FEA models can be useful in predicting composite strength. Yildiz et al. also performed FEA of composite hip implants. A 3D composite element was suggested and used in 3D FEA (Yildiz, Ha et al. 1998). It was effective in calculating the effect of multidirectional layers and tapered geometries. Santis et al. used composite stems made from carbon fibers and glass fabric pre-impregnated with poly-etherimide (Santis, Ambrosio et al. 2000). Stems were implanted in a PMMA cup without using actual bones. Rigidity was adjusted along different sections. Comparison showed that the adjusted composite stem has similar properties to the referenced surrounding bone, Figure 83.

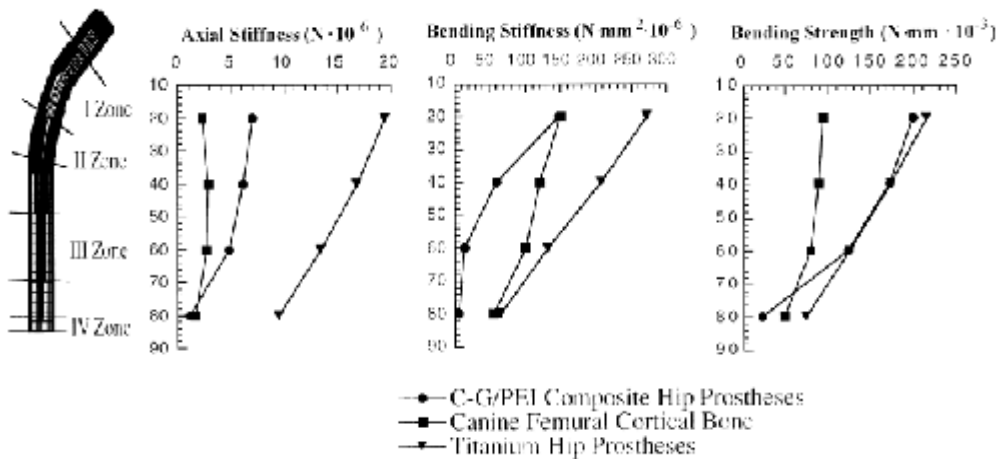


**Figure 83: Mechanical behavior of composite stem made using carbon fibers and glass fabric pre-impregnated with poly-etherimide C-G/PEI (Santis, Ambrosio et al. 2000) with permission from Elsevier.**

Adam et al. reported that aseptic loosening was observed in 92% of the press-fit anatomically shaped hip stems in a 6-year follow-up as seen in Figure 84 (Adam, Hammer et al. 2002). A total of 51 carbon stems were implanted. The proximal portion was rough while the distal portion had a smooth finish. Fibrous fixation was observed instead of bony ingrowth on carbon stems. The high loosening rate was related to the suboptimal stem shape and poor surface properties. A macro-texture was suggested for the next generation of composite stems to promote bone ingrowth.

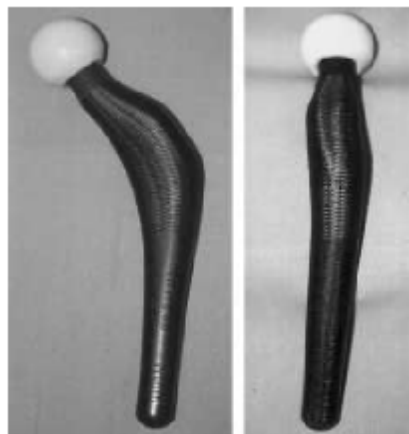


**Figure 84: Long carbon fibers closed the carbon powder core, (Adam, Hammer et al. 2002) with permission from Elsevier.**



U.S. Pat. Nos. 5,702,482, 5,509,935, 5,336,265, 5,007,931, 4,921,501 and 4,808,186 disclose femoral implants with longitudinal slots or channels to decrease the stiffness of the stem. U.S. Pat. Nos. 5,725,586, 5,316,550 and 5,092,899 proposed to decrease the stiffness of the stem with hollow interiors. Segmented flexible stems have also been suggested to change the stiffness of the stem from the proximal end to the distal end in U.S. Pat. No. 6,887,278. U.S. Pat. No. 5,480,449 describes a method to make a composite stem with a tapered metal core with a predetermined cross section and a composite shell. U.S. Pat. No. 6,913,623 discloses a two-piece fused femoral hip stem with different moduli. Implant manufacturing systems have also been patented. U.S. Pat. Nos. 6,254,639, 5,824,083, 6,932,842, and 5,370,692 suggest using CAD and image analysis for the production of customized implants.

#### **4.5. Metal Mesh stems**

We designed hip stems with mesh structures using the rhombic structures that were described in previous chapters. Cell sizes and orientations were also described above. Solid BioMedtrix BFX stems were used as the basis of these mesh stems. Three millimeter rhombic structures at 40% relative density were used in the design of the hip stems. They had high compressive strength (more than 80 MPa) and had a modulus close to cortical bone 12GPa.

Hip stems were designed using CAD files from BioMedtrix, Boonton, NJ, a veterinary orthopedic implant company. This model was first modified by creating through holes in the lower portion to reduce bending stiffness as shown in Figure 86(c). Then, as shown in Figure 86 (a) and (b), Boolean operations were used in Magics to create a hip implant with a lattice structure below the neck of the stem.

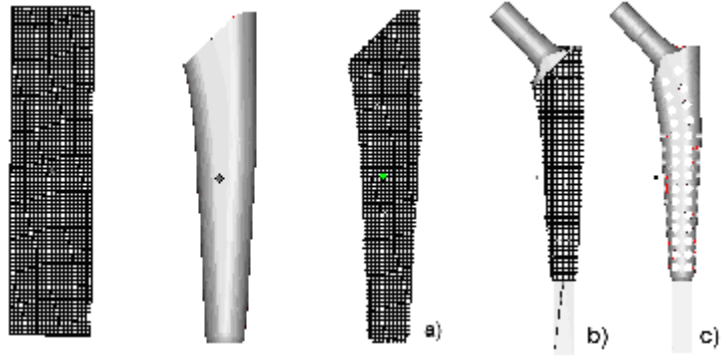


**Figure 86: Different configurations of hip stems a) Mesh block, Solid hip stem, and resulting mesh hip stem b) Complete mesh hip stem after Boolean operations. c) Solid hip stem with holes.**

Solid necks on the implants were retained to preserve compatibility with standard prosthetic heads and to have a stable head-to-stem interface. Solid material at the neck is also needed due to the impact the implant absorbs during insertion into the patient. Square pegs were added to the distal end of the stem to facilitate fixturing during subsequent 4-axis finish machining (see Figure 87).



**Figure 87: Hip stems with mesh, with holes, and solid from (left to right).**

The mesh stems were fabricated with reduced preheating to lessen the amount of powder sintering and to make it easier to remove unmelted powder from the meshed

region following processing. All mesh specimens were fabricated using the same beam segment thickness and beam segment orientation with respect to the build plane.

Three EBM fabricated hip stems were tested in the same fixture and setup. The weight of the stems after cleaning the powder was 46.72 grams for the solid stem, 33.83 grams for the stem with holes, and 26.19 grams for the mesh stem. The load was applied at the head at a rate of 1.27 mm/min. Hip stems were tested by fixing the square peg at the distal end in a vise as shown in Figure 89. The relative load/displacement ratio with respect to the solid stem was 1.16 for the stem with holes and 2.38 for the mesh stem. Linear load-displacement relationships are shown in Figure 88.

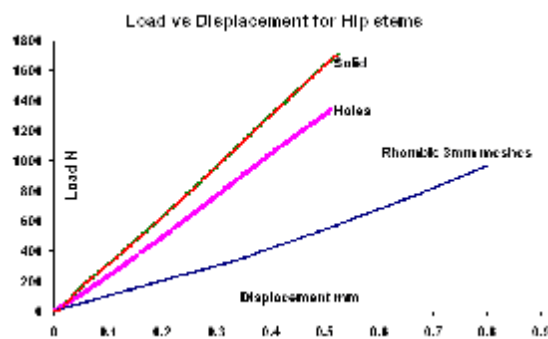
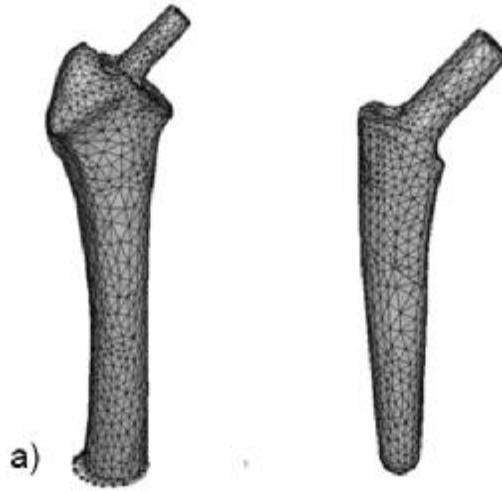


Figure 88: Results of bend testing of solid stem, stem with holes, and stem with mesh structure are shown in the graph



Figure 89: Testing of the hip stems

ABAQUS CAE 6.4 was used to model the effect of stem stiffness on bone and implant stresses. A Computed Tomography (CT) -scan of a broached femur was converted into an ABAQUS model using Materialise's Mimics 9.11 and assembled with different hip stem models (see Figure 90).



**Figure 90: Finite Element Analysis tetrahedral meshes of the femur-hip implant assembly and hip stem**

Due to the limitations of Mimics, only a tetrahedral mesh could be used for the femur. Materials and properties were assigned as follows: Ti-6Al-4V stem,  $E = 110$  GPa; bone,  $E = 15$  GPa; stem-shell,  $E = 20$  GPa; Stem-CoCr,  $E = 200$  GPa; Stem-Mesh,  $E = 20$  GPa. A Poisson's ratio of 0.3 was used for all cases. The bone ingrowth area was bounded to the stem as if it were one unit. Frictionless contact was assigned at the interface between the distal stem and the bone. The distal end of the bone was fixed, and the head of the stem was loaded normal to the surface. Input files were generated for each material assignment and submitted to the ABAQUS solver at the High Performance Computing Center (NCSU).

The results of the hip stem analyses for different material configurations are shown in Figure 91. Three material configurations were used for the hip stems - solid Co-Cr, solid Ti-6Al-4V, and mesh Ti-6Al-4V. Not surprisingly, the stresses on the distal portion of the stems were higher for stiffer materials. The contact regions were defined as the same at the bone ingrowth region for all three cases. The stress distribution on the femurs was different for the three cases.

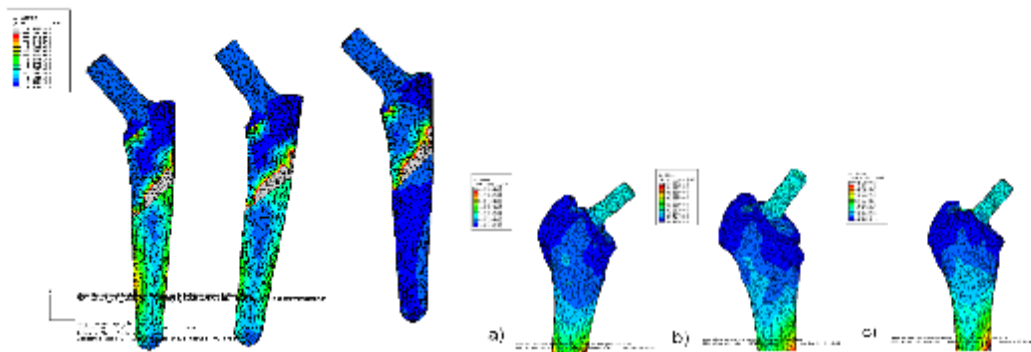


**Figure 91: Left) Von Mises stresses at the same scale show results for solid Co-Cr stem, solid Ti-6Al-4V stem, and mesh Ti-6Al-4V stem from left to right. Right) Von Mises stresses on the femur for a) Co-Cr stem b) Ti-6Al-4V stem c) mesh Ti-6Al-4V stem at the same stress color coding.**

The proximal portion of the femur exhibited higher stresses with decreasing stem stiffness as shown in Figure 91(b). The proximal portion of the femur with a Co-Cr stem shows a more pronounced stress shielding than the other two cases, and the mesh Ti6Al4V stem shows the lowest level of stress shielding.

The same design and manufacturing procedure was applied for different sizes of the implants. Extra machining features were also added and combined with the solid head section. Extra core sections may also be added to the solid part file and merged together with Boolean operations. At the end, two files will be created, one for solid parts and one for mesh parts.

Layered manufacturing processes need different processing parameters for thin sections and solid sections, depending on the area. EBM requires different processing parameters for mesh sections and solid sections. Beam speed and current are the most important parameters for meshes.

Because of these reasons, two different files are created to define mesh and solid regions. Layered manufacturing implants need supports to get a good surface finish and quality of down-facing surfaces. The EBM system has recently added wafer supports, which are similar to SLA Lightyear supports. These supports create thin walls, blocks, or lines that touch the part, but are easily broken away, as seen in Figure 92.

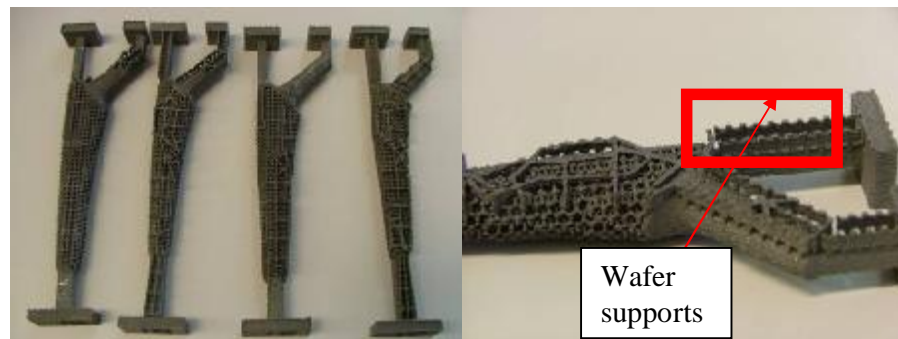


**Figure 92: Left) Hip stems size 9 and 10 were manufactured with reference features Right) Wafer supports are shown on the part surface.**

An important part of the layered based manufacturing is to define and add supports to the part files. This is very important in the EBM system due to the charging of the particles when the electrical conductivity of the current layer to the ground is weak. Thin solid sections may also curl up and deform during the processing. There are permanent supports and invisible supports in the EBM system. Sintered supports are invisible supports, which are mostly recyclable. Wafer supports are permanent and not recyclable and they need to be cut from the part. It is difficult to add supports on mesh surfaces. These supports need to be added such that they do not change the surface after

they are removed. The solid body of the implant is used to create supports for the mesh body. Wafer supports are similar to mesh files, but they are processed at different parameters. At the end of the file processing, four different files should be created for meshes, volume supports (invisible supports), wafer supports, and solid sections. Each implant file can be combined to create four files for the EBM build. The ratio of solid regions to mesh regions is important when processing time exceeds 2 or 3 minutes. It is important to keep the layers hot during the EBM processing; otherwise powder particles will charge and repel each other until an arc trip occurs. Powder charging is extremely deleterious to the success of the EBM build. For 4 hip stems, extra preheating was added after solid section melting to warm the powder before the mesh melting. Different sizes of implants or other unrelated parts can be combined with the current build files. Different sizes of hip implants and other parts can be built at a reasonable cost. According to the recent estimations, four hip implants will take 4 hours of melting time. Machine set up time is around 30 minutes. After the completion of the build, the machine will cool down for a minimum of 4 hours. Total cycle time for one set of implants will take approximately 8 to 9 hours.

The cost of the implants can be reduced with economies of scale, but post-processing is difficult. Parts will have approximately 0.4 mm surface roughness on each side. Reference features may be distorted because of the layered manufacturing and surface artifacts from supports. Machining offsets (minimum of 0.5 mm) may be added to machine components to final dimensions. Large parts may have distortions that affect the reference features. It is difficult to machine parts if they have internal features such as core sections. Even with the extra machining tolerances, parts can be off in relative positions of the internal features. Careful reference point planning is needed to achieve

good tolerances. The general quality of EBM parts is similar to the quality of sand castings. The EBM process enables the integration of mesh structures and solid sections in one part at the same build time. It is a single, complete process that can be used to create the hip stems with bone ingrowth features and also with skins at different regions. Hip stems with only bone ingrowth features are also shown in Figure 94. Bone ingrowth regions and populated meshes were intersected to create the mesh region see Figure 94.

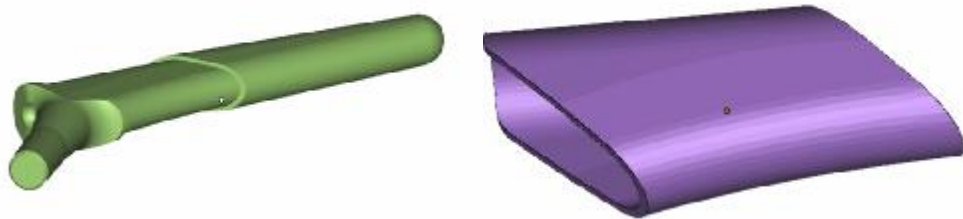


**Figure 93: Left) Solid hip stem without bone ingrowth region, Right) Bone ingrowth region**



**Figure 94: Hip stem with bone ingrowth meshes and reference features for finishing.**

## 5. BIOMECHANICAL TESTING OF STEMS

New hip implants need to be tested to determine the load transfer characteristics of the different stem designs. Initial tests were performed using cyclic loading for a predetermined loading scenario such as stair climbing. Different studies have been undertaken to investigate issues related to stresses at bone-implant interfaces. Primary stability has been investigated in experiments and also in FEA for the success of cementless implants. Follow-up studies and bone remodeling algorithms have been used to analyze the long-term behavior of the implant. Clinical studies are also conducted for new designs in multiple hospitals for several years to evaluate the safety and effectiveness of new implants. Composite femurs have been used to reduce the inter-variability in the femur in many studies. Other reported concerns in the primary stability testing are repeatability of the test, different responses from different stems, not including the benefit of porous coating, difference in insertion, and measurement methods.

Waide et al. investigated the bone remodeling for two different cemented hip implants (Waide, Cristofolini et al. 2003). Composite femurs were used in the study. Experimental and finite element methods have been used to determine strains under heel-strike phase loading. Different protocols have been combined and *in vitro* performance of cemented hip implants has been investigated as shown in Figure 95. Strain gages were attached at 5 levels. The bones were aligned at 11°.

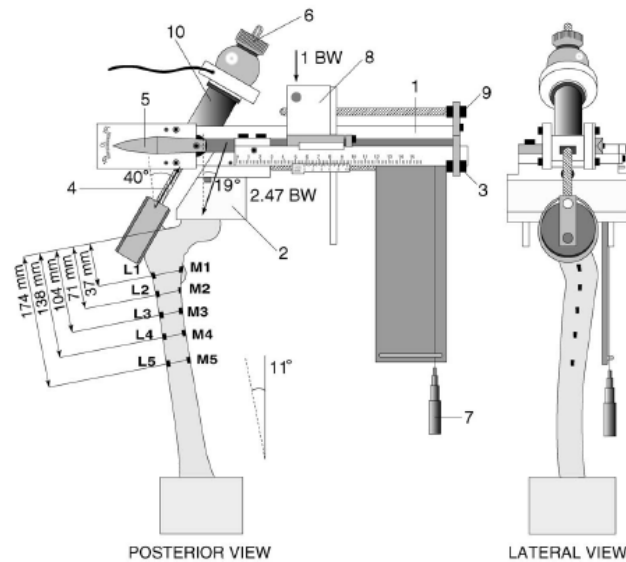


**Figure 95: Strain gages at five levels are shown at heel strike loading set up, (Waide, Cristofolini et al. 2003), reprinted with permission from Elsevier.**

Shih et al. performed mechanical and FE analysis for comparing intact and implanted femurs (Shih, Chen et al. 1997). Six pairs of human femora were used to measure the strain at every 100 N load increments. The loading angle was 10°. The ratio of proximal to distal strains were analyzed to understand the stress shielding effect. Failure load tests were also performed for some of the specimens from the load-displacement tests.

Walker et al. used 25 human femora to get the average geometry for designing a stem to fit the channel (Walker, Schneeweis et al. 1987). Tests were performed for uncemented and cemented stems using strain gages near the middle level. Micromotions were recorded with proximally installed transducers. Variations in the study were related to stem and bone contact. Gebauer et al. used 30 cementless stems of 6 different types and implanted in femurs taken at autopsy (Gebauer, Refior et al. 1989). Static loading and 50,000 cycle dynamic loading tests simulated the early months after surgery.

Harman et al. used composite femurs in primary stability tests (Harman, Toni et al. 1995). Use of a consistent geometry of composite femurs helped to reduce the variability. Controlled insertion for each stem also reduced inter-femur variability from 35% to 20%. Each femur was radiographed before the insertion of the stem and after the insertion to mark the alignment. Stair climbing loads were applied.

Besides using the uniform geometry for femurs, jigs for stem insertion, and other alignment features to reduce variability with cementless hip stem stability, Ooms et al. used calcium phosphate cement to fill the small gaps at the bone-implant interface (Ooms, Verdonschot et al. 2004). Cement was not used as a regular PMMA in the cemented hip stems. Instead it was used to reduce the variability in the cementless stem experiments. A paired t-test showed that there were significant differences between regular cementless stem and cementless with Ca-P. It was also reported that *in vivo* tests are needed for final conclusions.

Design parameter effects have also been analyzed to understand the relations between parameters and stresses. Vicecontia et al. studied the primary stability of uncemented human hip stems in probabilistic simulation (Vicecontia, Brusia et al. 2006). ANSYS was used for a Monte Carlo simulation to estimate the effect of weight, height, bone quality, and interface gaps on the anatomical stem under the stair climbing forces. Gillies et al. studied 5 different human hip implant designs and compared principal cortical bone strain distributions for those designs (Gillies, Morberg et al. 2002). It was also for primary stability test. Orientation of femurs were according to ISO 7206-4 (10° flexion and with 10° of adduction in the coronal plane). They have also reported the lack of experiments for long-term effects of those different designs.

## **5.1. In Vitro testing**

### **5.1.1. Overview**

The purpose of this testing was to show the difference between commercial BFX canine hip stems and newly developed EBM-made porous hip stems. This testing showed the relative stress shielding of the new hip stems compared to BFX hip stems. Testing was performed using cadaver bones, so it does not show what the differences are during bone ingrowth and bone remodeling. This study limits the scope of the results to the initial phase of the implant, where only press fit and related friction holds the stem inside the bone. Different sizes of hip stems were manufactured and tested. The results of these theses are presented below.

### **5.1.2. Materials and Methods**

Thirteen cadaver bones were harvested from skeletally mature large dogs that were euthanatized to control the dog population at the Harnett County animal shelter. The soft tissue was cleaned from around the femurs, and they were wrapped with saline-saturated gauze and placed in a plastic storage bag, at the necropsy lab of the College of Veterinary Medicine. Bones were scanned before and after stem preparation with an available CT scanner (Siemens Somatom 16 helical multislice CT scanner). Femurs were frozen until their use in testing. Cranio-caudal and medio-lateral radiographs were also made. Calibrated markers were placed between the bones to document the magnification of these radiographs. Parameter settings were adjusted based on bone density and experience. An experienced surgeon used radiographs as template to size the bones for

hip implants. Implant sizes were determined according to the BioMedtrix master templates. Surgery was performed in random order with exceptions in a few cases. Nine femur pairs were implanted and others were excluded because of small stem sizes. Hip stem types were implanted to random sides. For the details of the cadaver surgery see Appendix 2. Femur pairs were prepared with the same sizes of the broaches to implant one commercial BFX stem and one newly developed mesh based hip stem. The outer shape of the mesh hip implant was the same as the BioMedtrix hip implants. Commercial broaches were used for all surgeries.

All femora were cleaned of the remaining soft tissue and femoral condyles were cut at a 5.6" distance to the edge of the stem before potting. This distance was reduced to 5" for short femurs. Each pair was prepared together to reduce the variability in the study. After potting with cement, femurs were aligned in the fixture to a 10° angle as shown in the vertical direction and aligned horizontally to the screws on the fixture as shown in Figure 96.



**Figure 96: Left) Hip stems were aligned vertically at 10° with using impaction hole in the stem, and Right) aligned horizontally with reference to the screws on the alignment fixture.**

Strain gages were attached at four levels of the bone to get stress data at sections which were close to the greater trochanter, in the middle section, and in the tail of the

implant, which is similar to the study shown in Figure 98. One strain gage was attached to the opposite side as shown in Figure 97. The position of the strain gages is very important with respect to the hip stems, so the same referencing features were used to place the strain gages. A total of 5 120ohms linear strain gages (Omega Engineering) were used for each femur side (see Figure 97). Gage factor was 2.1 and excitation voltage 2.5Volts. Bone surfaces were prepared according to the Vishay Instruments strain gage manual. A polyurethane coating was applied over the strain gages after attachment to prevent short circuits due to the saline saturated gauzes on bones and also to reduce noise (Vishay Measurements Group, Raleigh, NC, USA).

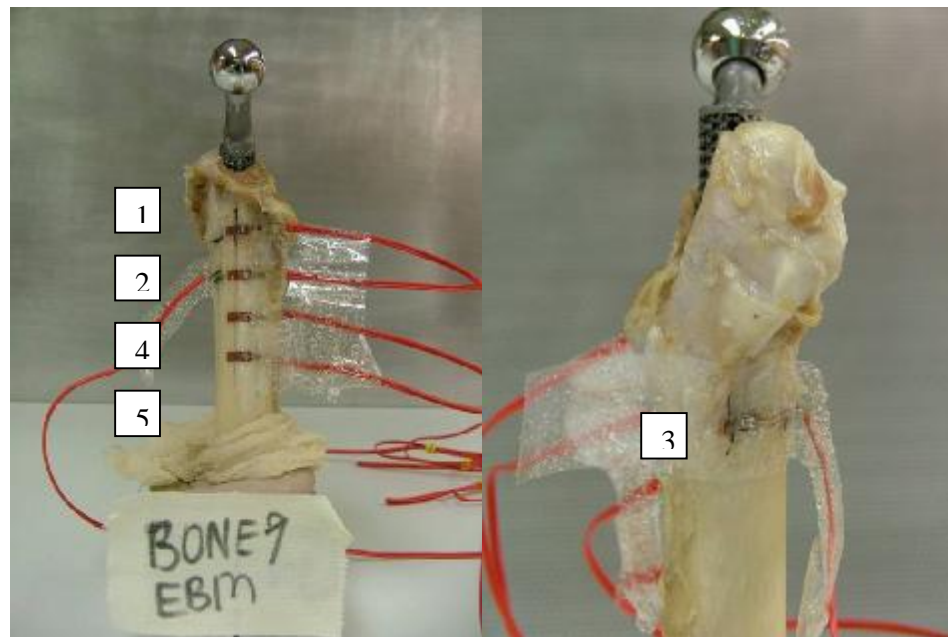


**Figure 97: Four strain gages were attached at the bending direction and one is at the same level at strain gage-2 opposite direction**

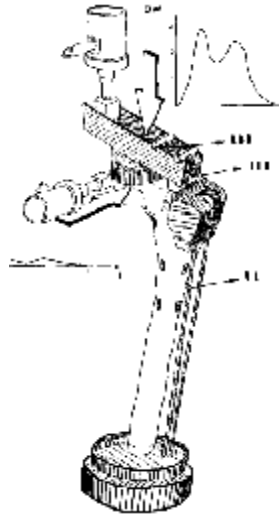


**Figure 98: Example test set up which shows 4 strain gages, (Munting and Verhelpen, 1995)**

Implanted bones were tested and data from strain gages was collected for further analysis in a setup shown in Figure 99. Data was collected with the auxiliary input channels of the Instron 8501 (Canton, MA) machine. The data acquisition board is an National Instruments (Austin, TX) SC-2043-SG set up for a 1/4 bridge circuit. Strain gages were attached to the bridge circuit and circuits were balanced for each gage before testing.

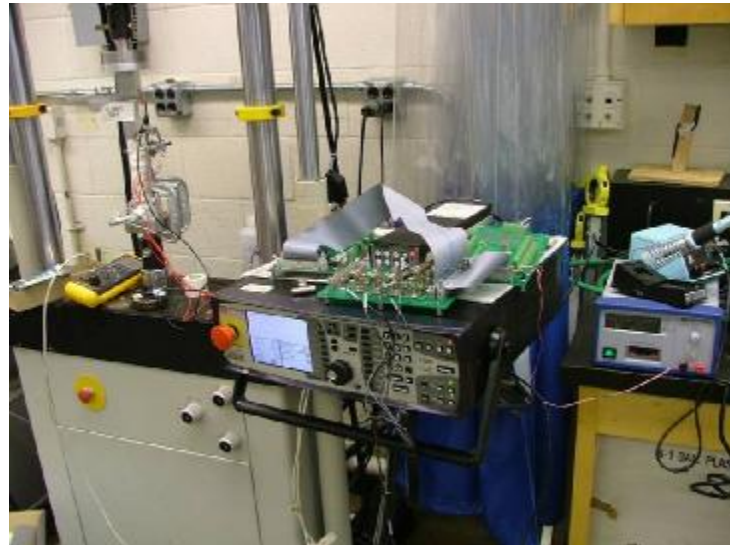


**Figure 99: In Vitro testing set up for hip stems.**

Loading was chosen as simple vertical loading for this phase of the study. Two loads were tested, 800N and 1600N for all implants. Loads were adjusted for the differences in the neck lengths. Before applying the loads, the implants were held at 20N for 30sec. The load increased at a displacement of 0.1mm/min up to 800N at first loading, and four cycles were repeated. Specimens were held at 20N for 30sec before loading in each run. Then, 1600N was applied without changing the setup. The loading angle was the same for all specimens. The distal portions of the femurs were fixed in PMMA casted cups. The same implant cup and head size were used for both implants as shown in Figure 100.



**Figure 100: Close up view of implant head and cup in a testing set up.**

Non-stochastic lattice structures were used to design hip implants for different sizes of the cadaver bones. Mesh hip stems with sizes of 9, 10, and 11 were manufactured

using EBM technology. EBM hip stems and commercial implants had the same external geometry, which was proper to use commercial tools in cadaver surgery.

The data was recorded in the testing machine for all gages, loads and displacements. Matlab R2007a (Natick, MA) was used to analyze data and reduce noise with moving averages. Strain readings, force and displacement of the load cell were recorded and analyzed in statistical software package (Jump, SAS version7). Gage positions were analyzed using one way Anova test and p values were checked for each loading level. Paired differences for cadaver pairs at different load levels were analyzed and paired mean was tested using “Student t” test and Wilcoxon signed rank test.

### **5.1.3. Results and Discussion**

Strain readings were analyzed in Matlab and noise is filtered using moving averages for 30 periods. Gage positions were compared with each other and results from each group were listed below. Example strain readings in mV are shown in Figure 101. Four loading cycles are shown for 5 strain gages.

#### 800N group:

- Gage3 and Gage1 were not significantly different ( $p=0.69$ ).
- Gage5 and Gage4 were not significantly different ( $p=0.27$ ).
- Others were significantly different as pairs, ( $p<0.01$ ).
- Measurements were over  $n=18$

#### 1600N group:

- Gage3 and Gage1 were not significantly different, ( $p=0.38$ ).
- Gage5 and Gage 2 were not significantly different, ( $p=0.13$ ).
- Gage5 and Gage4 were not significantly different, ( $p=0.45$ ).
- Other pairs were significantly different, ( $p<0.01$ ).
- Measurements were over  $n=15$  (other 3 was broken at this load level).

The paired differences of strain readings (mV) are compared in the table below for different load levels. Excitation voltage was 2.5 Volts and Gage factor was 2.13. Distal strain readings were significantly different at 1600N loading. Paired differences were not significantly different at 800N.

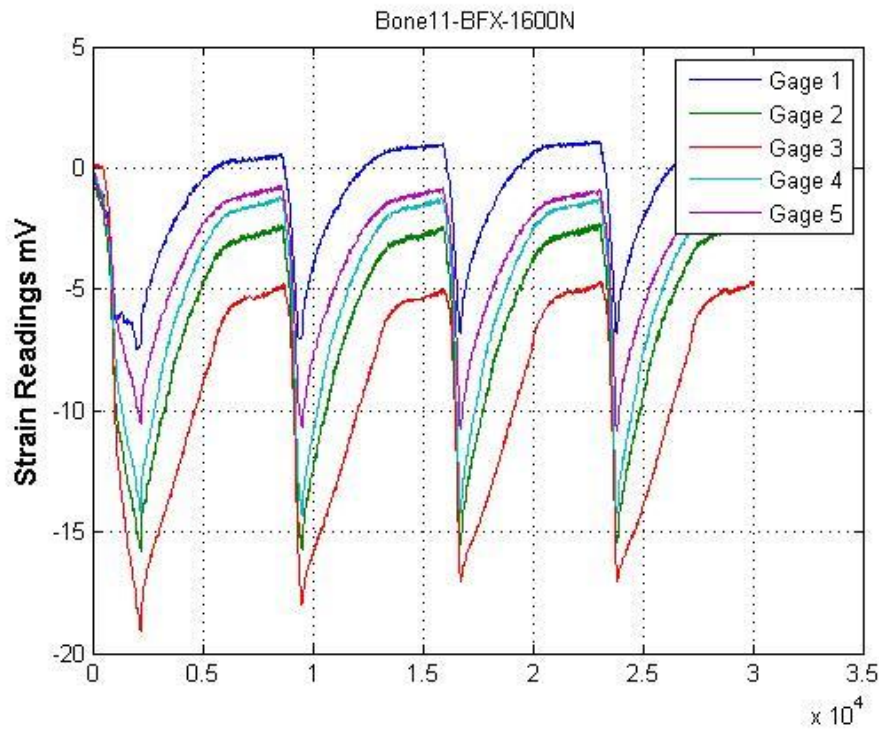


Figure 101: Strain Gage readings for Bone11-BFX at 1600N loading.

Table 12: 800N measurement of 9 paired samples

	Gage1	Gage2	Gage3	Gage4	Gage5
	P=0.375	P=0.1136	P=0.8403	P=0.4301	P=0.1895
	13.5 signed rank p=0.1289	13.5 signed rank p=0.1289	-6.5 signed rank p=0.4961	9.5 signed rank p=0.3008	7.5 signed rank p=0.4258
Paired differences Mean(mV):	0.9950	1.4462	-0.3492	0.3207	1.0849
St.dev.:	3.1776	2.4429	5.0335	1.1578	2.2698

**Table 13: 1600N measurement of 6 paired samples**

	Gage1	Gage2	Gage3	Gage4	Gage5
	P=0.2941	0.0856	0.2379	P=0.0303*	P=0.0625
	7 signed rank p=0.2969	9 signed rank p=0.1563	-7 signed rank p=0.2969	14 signed rank p=0.0078*	9 signed rank p=0.0781
Paired differences Mean(mV):	2.2365	5.4878	-2.7368	7.4261	5.2268
Stdev:	5.1474	7.0636	5.5243	8.5204	7.7595

Paired differences showed higher variations at distal strain gages. Gage 3 was placed at the back position with the same level as gage 2. Gages at different levels showed smooth distribution for EBM stems, whereas BFX stem showed concentrations at different points.

Interface stiffness was calculated at the last cycle of the 800N loading for all samples. It was observed that BFX stem-bone stiffness was significantly higher than EBM stem-bone stiffness over 8 pair values. . The mean ( $\pm$ SD) difference in stiffness was  $611.29 \pm 76$  N/mm ( $P < 0.0001$ ).

#### **5.1.4. Conclusion**

Hip stems with tailored material properties and integrated bone ingrowth features were manufactured in Electron Beam Melting System. Different sizes of the hip stems were manufactured and implanted into nine pairs of cadaver femur to compare with the commercial BFX hip stems. Commercially available surgical instruments were used to perform the surgeries. The surgical performance of the new hip stems was similar to the commercially available stem. Some additional over-broaching was required because of

the exposed mesh sections from the support structures in EBM. No fissure occurred during the surgery and all stems were successfully implanted the conventional cementless surgical protocol.

The stiffness of the bone-implant interface was significantly lower for flexible stems than conventional cementless stems. Strain was significantly lower at the tail of the stems for flexible stems compared to conventional BFX stems. There were not significant differences in subsidence and impaction distances. Sample size was limited to nine in this study and some of the results did not differ between groups. Thirteen bone pairs were collected, but only 9 of them were templated for the large stems sizes available for this project.

Even though homogenous meshes were used in this study, it is also possible to manufacture gradient meshes. The mesh density may be decreased from the proximal to the tail of the stem to further reduce modulus at the end.

Suggested manufacturing method can be used to make hip stems with different sizes in one step which will reduce the cost. EBM stems can withstand higher compaction stresses and it is possible to make them for people. Further fatigue testing is required to be confident in long-term life of the stems.

## 6. CONCLUSION AND FUTURE WORK

This dissertation shows the development, design, manufacturing, testing, and analysis of the new hip stems and mesh structures. Discussed methods and technologies are applicable to many different areas. The suggested hip stem manufacturing process is a novel method, and hip stems were tested and showed practical usage in cadaver bones. Further studies are needed to characterize the bone ingrowth and long term behavior of the new hip stems.

Mesh structures with high compressive strength over 87 MPa and elastic modulus around 12 GPa were developed. Tailored properties of the structures were shown for different unit cell designs. It is possible to manufacture structures with a modulus from 25MPa to 12GPa using similar cell topologies. It was shown that non-stochastic cellular structures can be designed with complex cell topologies, and fabricated using Electron Beam Melting technology. These EBM-processed structures have material properties that comparable and may even be superior in some instances to structures made using other processes.

The effects of build orientation and build parameters were studied and useful knowledge was gained. However, additional experiments and testing are needed to quantify all the effects in mesh properties. Some of the structures show low plasticity and sensitivity to the processing parameters. Future work will focus on the development of the structures under different processing parameters and heat treatments.

Non-stochastic cell structures can be used for different applications and only the hip stem application was discussed in this dissertation. Hip stems were designed and fabricated using the EBM technology. Mesh hip stems were compared to the commercial

CoCr hip stems, which have the same design, in a cadaver study. The results from this study indicate that mesh hip stems have less bone-implant stiffness and less distal stresses.

Our structural optimization work suggests that cell topologies can be improved to increase the strength of the structure or to reduce the weight of the structure to tailor for specific applications. Future 3D optimization of large scale structures, including hip stems, shows promise. Ongoing work in 3D optimization will combine finite element analysis and optimization software (ANSYS and Matlab) to optimize structures for given objectives and constraints.

## 7. REFERENCES

- Adam, F., D. S. Hammer, et al. (2002). "Early failure of a press-fit Carbon Fiber Hip Prosthesis with a smooth surface." The journal of Arthroplasty **17**: 217-223.
- Ashby, M. F. (2006). "The properties of foams and lattices." Philosophical Transactions of the Royal Society A **364**: 15-30.
- Ashby, M. F., A. G. Evans, et al. (2000). Metal foams: a design guide. UK Butterworth-heinemann.
- Au, M. (1994). "Isoelastic total hip replacement: Clinical evaluation of prosthetic isoelasticity." J Formos Med. Assoc. **93**: 497-502.
- Bagge, M. (2000). "A model of bone adaptation as an optimization process." Journal of Biomechanics **33**: 1349-1357.
- Banhart, J. (2000). "Manufacturing Routes for Metallic Foams." Jom **52**: 22-27.
- Baris, N. M., M. G. Golkovsky, et al. (2000). "Study of coatings obtained by electron beam melting of TiN, TiC, TiB<sub>2</sub>, ?-MoB powders on titanium base." Proceedings of the VI International Scientific and Practical Conference of Students, Post-graduates and Young Scientists: 129-130.
- Bellemans, J. (1999). "Osseointegration in porous coated knee arthroplasty. The influence of component coating type in sheep." Acta Orthop Scand Suppl **288**: 1-35.
- Bendsoe, M. and N. Kikuchi (1988). "Generating optimal topologies in structural design using a homogenization method." Computer Methods in Applied Mechanics and Engineering **71**: 197-224.
- Bendsoe, M. P. (1995). Optimization of structural topology, shape, and material. Springer-Verlag, Berlin.
- Bendsoe, M. P., A. Ben-Tal, et al. (1994). "Optimization methods for truss geometry and topology design." Structural and Multidisciplinary Optimization **7**: 141-159.

- Bendsoe, M. P. and O. Sigmund (2003). Topology Optimization: Theory, Methods and Applications. Berlin, Germany, Springer.
- Bobyn, J. D., E. S. Mortimer, et al. (1992). "Producing and avoiding stress shielding. Laboratory and clinical observations of noncemented total hip arthroplasty." Clinical orthopaedics and related research **274**(274): 79-96.
- Bobyn, J. D., G. J. Stackpool, et al. (1999). "Characteristics of bone ingrowth and interface mechanics of a new porous tantalum biomaterial." J Bone Joint Surg Br **81-B**: 907-914.
- Brothers, A. H. and D. C. Dunand (2006). "Amorphous metal foams." Scripta Materialia **54**: 513-520.
- Buhl, T. (2002). "Simultaneous topology optimization of structure and supports." Struc. Multidisc. Optim. **23**: 336-346.
- Calhoun, L. R., J. T. Allen, et al. (1997). "Electron-Beam Systems for Medical Device Sterilization." Medical Plastics and Biomaterials Magazine(July).
- Callaghan, J. J., J. C. Albright, et al. (2000). "Charnley Total Hip Arthroplasty with Cement : Minimum Twenty-five-Year Follow-up." Journal of Bone and Joint Surgery Am **82**(4): 487-497.
- Chang, F. K. and J. L. Perez (1990). "Stiffness and strength tailoring of a hip prosthesis made of advanced composite materials." J. of Biomedical Materials Research **24**: 873-899.
- Charnley, J. (1960). "Anchorage of femoral head prosthesis to shaft of femur." Journal of Bone and Joint Surgery **42B**: 28-30.
- Cheng, G. (1995). "Some aspects of truss topology optimization." Structural and Multidisciplinary Optimization **10**: 173-179.
- Chino, Y., M. Mabuchi, et al. (2006). "Processing and mechanical properties of a porous low carbon steel with a controlled porous structure by imposition of a static magnetic field." Materials Science and Engineering A **417**: 281-286.
- Chua, C. K., K. F. Leong, et al. (2003). "Development of a tissue engineering scaffold structure library for rapid prototyping. Part 1: investigation and classification." International Journal of Advanced Manufacturing Technology **21**: 291-301.

- Cook, R. D., D. S. Malkus, et al. (2002). Concepts and Applications of Finite Element Analysis. New York, John Wiley & Sons.
- Cormier, D., O. Harrysson, et al. (2004). Optimization of the Electron Beam Melting Process. IERC 2004, Houston, Texas, USA.
- Cormier, D., O. Harrysson, et al. (2004). "Characterization of High Alloy Steel Produced Via Electron Beam Melting." Rapid Prototyping Journal **10**(1): 35-41.
- Cormier, D., H. West, et al. (2005). "Electron Beam Melting of g-Titanium Aluminide." Proceedings of SFF 2005.
- Cormier, D., H. West, et al. (2004). "Characterization of Thin Walled Ti-6Al-4V Components Produced Via Electron Beam Melting." Proceedings of SFF 2004.
- Cowin, S. C., L. Moss-Salentijn, et al. (1991). "Candidates for the mechanosensory system in bone." J Biomech Eng. **113**: 191-197.
- Crowninshield, R. D. (1986). "Mechanical properties of porous metal total hip prostheses." Instr. Course Lect. **35**: 144-148.
- Curodeau, A., E. Sachs, et al. (2000). "Design and Fabrication of Cast Orthopedic Implants with Freeform Surface Textures from 3-D Printed Ceramic Shell." Journal of Biomedical Materials Research Applied Biomaterials **53**: 525-535.
- Ducy, P., T. Schinke, et al. (2000). "The Osteoblast: A Sophisticated Fibroblast under Central Surveillance." Science **289**: 1501-1504.
- El-Warrak, A. O., M. Olmstead, et al. (2004). "An experimental animal model of aseptic loosening of hip prostheses in sheep to study early biochemical changes at the interface membrane." BMC Musculoskelet Disord. **5**: 1-13.
- Engh, C. A. and J. D. Bobyn (1988). "The influence of stem size and extent of porous coating on femoral bone resorption after primary cementless hip arthroplasty." Clinical orthopaedics and related research **231**(231): 7-28.
- Engh, C. A., J. D. Bobyn, et al. (1987). "Porous-coated hip replacement. The factors governing bone ingrowth, stress shielding, and clinical results." J Bone Joint Surg Br **69**: 45-55.
- Fang, Z., B. Starly, et al. (2005). "Computer-aided characterization for effective mechanical properties of porous tissue scaffolds." Computer-Aided Design **37**(65-72).

- Fernandes, P. R., J. Folgado, et al. (2002). "A contact model with ingrowth control for bone remodeling around cementless stems." Journal of Biomechanics **35**(2): 167-176.
- Gebauer, D., H. J. Refior, et al. (1989). "Micromotions in the primary fixation of cementless femoral stem prostheses." Archives of Orthopaedic and Trauma Surgery **108**: 300-307.
- Gibson, L. J. (2000). "Mechanical Behavior of Metallic Foams." Annu. Rev. Mater. Sci. **30**: 191-227.
- Gillies, R. M., P. H. Morberg, et al. (2002). "The influence of design parameters on cortical strain distribution of a cementless titanium femoral stem." Medical Engineering & Physics **24**: 109-114.
- Gross, S. and E. W. Abel (2001). "A finite element analysis of hollow stemmed hip prostheses as a means of reducing stress shielding of the femur." Journal of Biomechanics **34**: 995-1003.
- Gruen, T. A., G. M. McNeic, et al. (1979). "Modes of failure of cemented stem-type femoral components: a radiographic analysis of loosening." Clinical Orthopaedics and Related Research **141**: 17-23.
- Haferkamp, H., A. Ostendorf, et al. (2004). "Combinations of Yb: TAG- disc laser and roll-based powder deposition for the micro-laser sintering." Journal of Materials Processing Technology **149**: 623-626.
- Harman, M. K., A. Toni, et al. (1995). "Initial stability of uncemented hip stems: an in-vitro protocol to measure torsional interface motion." Medical Engineering & Physics **17**: 163-171.
- Harrysson, O. L. A., D. R. Cormier, et al. (2003). Direct Fabrication of Metal Orthopedic Implants Using Electron Beam Melting Technology. Solid Freeform Fabrication Symposium, Austin, Texas, USA.
- Harte, A. M., N. A. Fleck, et al. (2001). "The fatigue strength of sandwich beams with an aluminium alloy foam core." International Journal of Fatigue **23**: 499-507.
- Hollister, S. J. (2005). "Porous scaffold design for tissue engineering." Nature materials **4**: 518-524.
- Hollister, S. J., R. Maddox, et al. (2002). "Optimal design and fabrication of scaffolds to mimic tissue properties and satisfy biological constraints." Biomaterials **23**: 4095-4103.

- Huang, S.-C. and G.-J. Lan (2006). "Design and fabrication of a micro-compliant amplifier with a topology optimal compliant mechanism integrated with a piezoelectric microactuator." Journal of Micromechanics Microengineering **16**: 531-538.
- Huiskes, R., R. Ruimerman, et al. (2000). "Effects of mechanical forces on maintenance and adaptation of form in trabecular bone." Nature materials **405**: 704-706.
- Huiskes, R., H. Weinans, et al. (1992). "The relationship between stress shielding and bone resorption around total hip stems and the effects of flexible materials." Clinical orthopaedics and related research **274**(274): 124-134.
- Imatani, J., T. Ogura, et al. (2005). "Custom AO small T plate for transcondylar fractures of the distal humerus in the elderly." Journal of Shoulder and Elbow Surgery **14**(6): 611-615.
- Jacobs, J. J., J. L. Gilbers, et al. (1998). "Corrosion of metal orthopaedic implants." The Journal of Bone and Joint Surgery (American) **80**: 268-282.
- Jakim, I., C. Barlin, et al. (1988). "RM isoelastic total hip arthroplasty: A review of 34 cases." The Journal of Arthroplasty **3**: 191-199.
- Jang, I. G. and B. M. Kwak (2005). Evolutionary topology optimization for large-scale problems using design space adjustment and refinement. 6th World Congresses of Structural and Multidisciplinary Optimization, Rio de Janeiro, Brazil.
- Kaddick, C., S. Stur, et al. (1997). "Mechanical simulation of composite hip stems." Medical Engineering and Physics **19**(5): 431-439.
- Kanetake, N. and M. Kobashi (2006). "Innovative processing of porous and cellular materials by chemical reaction." Scripta Materialia **54**: 521-525.
- Karrholm, J., C. Anderberg, et al. (2002). "Evaluation of a femoral stem with reduced stiffness." The Journal of Bone & Joint Surgery **84-A**(9): 1651-1658.
- Katoozian, H., D. T. Davy, et al. (2001). "Material optimization of femoral component of total hip prosthesis using fiber reinforced polymeric composites." Medical Engineering & Physics **23**: 503-509.
- Kirsh, U. (1989). "Optimal topologies of structures." Applied Mechanics Reviews **42**: 223-239.
- Klein-Nulend, J., R. G. Bacabac, et al. (2005). "Mechanobiology of bone tissue." Pathologie Biologie **53**: 576-580.

Kowalczyk, P. (2006). "Orthotropic properties of cancellous bone modelled as parameterized cellular material " Computer Methods in Biomechanics and Biomedical Engineering **9**(3): 135-147.

Kroger, H., E. Vanninen, et al. (1997). "Periprosthetic bone loss and regional bone turnover in uncemented total hip arthroplasty: a prospective study using high resolution single photon emission tomography and dual-energy X-ray absorptiometry." Journal of Bone Mineral Research **12**(3): 487-492.

Kruth, J. P., X. Wang, et al. (2003). "Lasers and materials in selective laser sintering." Assembly Automation **23**: 357-371.

Kuo, C. K., W. J. Li, et al. (2006). "Cartilage tissue engineering: its potential and uses." Current Opinion in Rheumatology **18**: 64-73.

Kurtz, S. M., O. K. Muratoglu, et al. (1999). "Advances in the processing, sterilization, and crosslinking of ultra-high molecular weight polyethylene for total joint arthroplasty." Biomaterials **20**(18): 1659-1688.

Kusakabe, H., T. Sakamaki, et al. (2004). "Osseointegration of a hydroxyapatite-coated multilayered mesh stem." Biomaterials **25**: 2957-2969.

Lee, W. H., J. W. Park, et al. (2000). "Surface characteristics of a porous-surfaced Ti-6Al-4V implant fabricated by electro-discharge-compaction." Journal of Materials Science **35**: 593 - 598.

Lemaire, V., F. L. Tobin, et al. (2004). "Modeling the interactions between osteoblast and osteoclast activities in bone remodeling." Journal of Theoretical Biology **229**: 293-309.

Li, J. P., J. R. Wijn, et al. (2006). "Porous Ti6Al4V scaffold directly fabricating by rapid prototyping: Preparation and in vitro experiment." Biomaterials **27**: 1223-1235.

Lin, C. Y., N. Kikuchi, et al. (2004). " A novel method for biomaterial scaffold internal architecture design to match bone elastic properties with desired porosity." Journal of Biomechanics **37**: 623-636.

Lin , L. (2000). "The advances and characteristics of high-power diode laser materials processing." Optics and Lasers in Engineering **34**: 231-253.

Lopes, R. A., F. V. Stump, et al. ( 2005). Topology optimization of three dimensional structures under self-weight and inertial forces

6th World Congresses of Structural and Multidisciplinary Optimization Rio de Janeiro, Brazil

Madey, S. M., J. J. Callaghan, et al. (1997). "Charnley total hip arthroplasty with use of improved techniques of cementing." Journal of Bone and Joint Surgery **79A**: 53-64.

Maistrelli, G. L., V. Fornasier, et al. (1991). "Effect of Stem Modulus in a Total hip Arthroplasty Model." Journal of Bone and Joint Surgery - British **73-B**: 43-46.

Mandell, J. A., D. R. Carter, et al. (2004). "A conical-collared intramedullary stem can improve stress transfer and limit micromotion." Clinical Biomechanics **19**: 695-703.

Mann, K. A., D. L. Bartel, et al. (1997). "Influence of stem geometry on mechanics of cemented femoral hip components with a proximal bond." Journal of Orthopaedic Research **15**: 700-706.

Maxwell, J. C. (1864). "On the calculation of the equilibrium and stiffness of frames." Philosophical Magazine **27**: 294-299.

Mazunder, J., A. Schifferer, et al. (1999). "Direct materials deposition: designed macro and microstructure." Materials Research Innovations **3**: 118-131.

Mckellop, H., E. Ebramzadeh, et al. (1991). "Comparison of the Stability of Press-Fit Hip Prosthesis Femoral Stems Using a Synthetic Model Femur." Journal of Orthopaedic Research **9**: 297-305.

Medlin, D. J., S. Charlebois, et al. (2004). Metallurgical characterization of a porous tantalum biomaterial (Trabecular Metal) for orthopaedic implant applications. Materials & Processes from Medical Devices Conference. Anaheim, CA; USA: 394-398.

Melican, M. C., M. C. Zimmerman, et al. (2001). "Three-dimensional printing and porous metallic surfaces: A new orthopedic application." Journal of Biomedical Material Research **55**: 194-202.

Miller, S. C., L. de Saint-Georges, et al. (1989). "Bone lining cells: structure and function." Scanning Microscopy **3**: 953-960.

Moroz, A., M. C. Crane, et al. (2006). "Phenomenological model of bone remodeling cycle containing osteocyte regulation loop." BioSystems **84**: 183-190.

- Munting, E. and M. Verhelpen (1995). "Fixation and effect on bone strain pattern of a stemless hip prosthesis." Journal of Biomechanics **28**: 949-961.
- Naidu, S. H., M. J. Moulton, et al. (1997). "Orderly oriented wire mesh: a novel porous coating." Orthopedics **20**: 437-441.
- Nelson, C. L. (2002). "Cemented femoral revision: technique and outcome." American Journal of Orthopedics **31**: 187-189.
- Nieh, T. G., K. Higashi, et al. (2000). "Effect of cell morphology on the compressive properties of open-cell aluminum foams." Materials Science and Engineering A **283**: 105-110.
- Niinimaki, T. and P. Jalovaara, 66, 347-51. (1995). "Bone loss from the proximal femur after arthroplasty with an isoelastic femoral stem. BMD measurements in 25 patients after 9 years." Acta Orthopaedica Scand.
- Niinimaki, T., J. Puranen, et al. (1994). "Total hip arthroplasty using isoelastic femoral stems. A seven- to nine-year follow-up in 108 patients." Journal of Bone and Joint Surgery - British **76**: 413-418.
- Ooms, E. M., N. Verdonshot, et al. (2004). "Enhancement of initial stability of press-fit femoral stems using injectable calcium phosphate cement: an in vitro study in dog bones." Biomaterials **25**: 3887-3894.
- Papalambros, P. Y. and D. J. Wilde (2000). Principle of optimal design: Modelling and computation. Cambridge, UK, Cambridge University Press.
- Poss, R., P. Walker, et al. (1988). "Strategies for improving fixation of femoral components in total hip arthroplasty." Clinical orthopaedics and related research **235**: 181-194.
- Prendergast, P. J. and D. Taylor (1990). "Stress analysis of the proximomedial femur after total hip replacement." Journal of Biomedical Engineering **12**: 379- 382.
- Qiu, J., J. T. Dominici, et al. (1997). "Composite titanium dental implant fabricated by electro-discharge compaction." Biomaterials **18**: 153-160.
- Rabiei, A. and A. T. O'Neill (2005). "A study on processing of a composite metal foam via casting." Materials Science and Engineering A **404**: 159-164.

Ramamurti, B. S., T. E. Orr, et al. (1997). "Factors influencing stability at the interface between a porous surface and cancellous bone: a finite element analysis of a canine in vivo micromotion experiment." Journal of Biomedical Materials Research **36**: 274-280.

Ramaniraka, N. A., L. R. Rakotomanana, et al. (2000). "The fixation of the cemented femoral component effects of stem stiffness, cement thickness and roughness of the cement-bone surface." The journal of Bone & Joint Surgery Br **82**(2): 297-303.

Ritter, M. A., E. M. Keating, et al. (1990). "A porous polyethylene-coated femoral component of a total hip arthroplasty." The journal of Arthroplasty **5**(1): 83-88.

Rozvany, G. I. N. (1996). "Difficulties in truss topology optimization with stress, local buckling and system stability constraints." Structural and Multidisciplinary Optimization **11**: 213-217.

Rozvany, G. I. N., M. P. Bendsoe, et al. (1995). "Layout optimization of structures." Applied Mechanics Reviews **48**: 41-119.

Rozvany, G. I. N., M. Zhou, et al. (1992). "Generalized shape optimization without homogenization." Structural Optimization **4**: 250-252.

Ruimerman, R., P. Hilbers, et al. (2005). "A theoretical framework for strain-related trabecular bone maintenance and adaptation." Journal of Biomechanics **38**(4): 931-941.

Ryan, G., A. Pandit, et al. (2006). "Fabrication methods of porous metals for use in orthopaedic applications." Biomaterials **27**(13): 2651-2670.

Santis, R. D., L. Ambrosio, et al. (2000). "Polymer-based composite hip prostheses." Journal of Inorganic Biochemistry **79**: 97-102.

Santos, E. C., M. Shiomi, et al. (2006). "Rapid manufacturing of metal components by laser forming." International journal of machine tools & Manufacture **46**: 1459-1468.

Sarzi-Puttini, P., M. A. Cimmino, et al. (2005). "Osteoarthritis: an overview of the disease and its treatment strategies." Seminars in Arthritis Rheumatism **35**: 1-10.

Scales, J. T. (1966). "Arthroplasty of the hip using foreign materials: a history." Proceedings of the Institution of Mechanical Engineers **181**: 64-84.

Scotchford, C. A., M. J. Garle, et al. (2003). "Use of a novel carbon fibre composite material for the femoral stem component of a THR system: in vitro biological assessment." Biomaterials **24**: 4871-4879.

- Semlitsch, M. and H. G. Willert (1997). "Clinical wear behaviour of ultra-high molecular weight polyethylene cups paired with metal and ceramic ball heads in comparison to metal-on-metal pairings of hip joint replacements " **211**(1): 73-88.
- Settecerri, J. J., S. S. Kelley, et al. (2002). "Collar versus collarless cemented HD-II femoral prostheses." Clinical Orthopaedics & Related Research **398**: 146-152.
- Shih, C. H., W. P. Chen, et al. (1997). "New concepts- biomechanical studies of a newly designed femoral prosthesis (cervico-trochanter prosthesis)." Clinical Biomechanics **12**: 482-490.
- Sigmund, O. (1994). "Materials with prescribed constitutive parameters an inverse homogenization problem." International Journal of Solids and Structures **31**: 2329-2513.
- Sigmund, O. (1995). "Tailoring materials with prescribed elastic properties." Mechanical Materials **20**: 351-368.
- Sigmund, O. (2000). "Topology optimization: A Tool for the Tailoring of Structures and Materials." Philosophical Transactions of the Royal Society London A **358**: 211-227.
- Sigmund, O. (2001). "A 99 line topology optimization code written in Matlab." Structural and Multidisciplinary Optimization **21**: 120-127.
- Stains, J. P. and R. Civitelli (2005). "Cell-to-cell interactions in bone." Biochemical and Biophysical Research Communications **328**: 721-727.
- Sumner, D. R., T. M. Turner, et al. (1998). "Functional adaptation and ingrowth of bone vary as a function of hip implant stiffness." Journal of Biomechanics **31**: 909-917.
- Sun, W., B. Starly, et al. (2005). "Bio-CAD modeling and its applications in computer-aided tissue engineering." Computer-Aided Design **37**: 1097-1114.
- Suva, L. J., D. Gaddy, et al. (2005). "Regulation of bone mass by mechanical loading: microarchitecture and genetics." Current Osteoporosis Reports **3**: 46-51.
- Svanberg, K. (1987). "The method of moving asymptotes-a new Method for structural optimization." International journal for numerical methods in engineering **24**: 359-373.
- Swanson, T. V. (2005). "The Tapered Press Fit Total Hip Arthroplasty A European Alternative." The Journal of Arthroplasty **20**: 63-67.
- Tai, C. L., C. H. Shih, et al. (2003). "Finite element analysis of the cervico-trochanteric stemless femoral prosthesis." Clinical Biomechanics **18**: S53-S58.

- Teitelbaum, S. L. (2000). "Bone resorption by Osteoclasts." Science **289**: 1504-1508.
- Turner, T. M., D. R. Sumner, et al. (1997). "Maintenance of Proximal Cortical Bone with Use of a Less Stiff Femoral Component in Hemiarthroplasty of the Hip without Cement. An Investigation in a Canine Model at Six Months and Two Years." Journal of Bone and Joint Surgery Am **79**: 1381-1390.
- Vendra, L. J. and A. Rabiei (2007). "A study on aluminum-steel composite metal foam processed by casting " Materials Science and Engineering A **465**: 59-67.
- Vicecontia, M., G. Brusia, et al. (2006). "Primary stability of an anatomical cementless hip stem: A statistical analysis." Journal of Biomechanics **39**(7): 1169-1179.
- Vutova, K. and G. Mladenov (1999). "Computer simulation of the heat transfer during electron beam melting and refining." Vacuum **53**(1): 87-91.
- Wadley, H. N. G., N. A. Fleck, et al. (2003). "Fabrication and structural performance of periodic cellular metal sandwich structures." Composites Science and Technology **63**: 2331-2343.
- Waide, V., L. Cristofolini, et al. (2003). "Experimental investigation of bone remodeling using composite femurs." Clinical Biomechanics **18**: 523-536.
- Walker, P. S., D. Schneeweis, et al. (1987). "Strains and micromotions of press-fit femoral stem prostheses." Journal of Biomechanics **20**: 693-702.
- Wang, D., W. H. Zhang, et al. (2002). "Truss shape optimization with multiple displacement constraints." Computer Methods In Applied Mechanics And Engineering **191**(33): 3597-3612.
- Wen, C. E., Y. Yamada, et al. (2002). "Novel titanium foam for bone tissue engineering." Journal of Materials Research **17**: 2633-2639.
- Wettergreen, M. A., B. S. Bucklen, et al. (2005). "Creation of a unit block library of architectures for use in assembled scaffold engineering." Computer-Aided Design **37**: 1141-1149.
- Whiteside, L. A., D. Amador, et al. (1988). "The effects of the collar on total hip femoral component subsidence." Clinical Orthopaedics & Related Research **231**: 120-126.
- Willert, H. G., H. Bertram, et al. (1990). "Osteolysis in alloarthroplasty of the hip: the role of bone cement fragmentation." Clinical Orthopaedics & Related Research **258**: 108-121.

- Wu, X. and J. Mei (2003). "Near net shape manufacturing of components using direct laser fabrication technology " Journal of Materials Processing Technology **135**: 266-270.
- Yang, Y. Z., J. M. Tian, et al. (2000). "Preparation of graded porous titanium coatings on titanium implant materials by plasma spraying." Journal of Biomedical Material Research **52**: 333-337.
- Yildiz, H., S. K. Ha, et al. (1998). "Composite hip prosthesis design: I Analysis." Journal of Biomedical Material Research **39**: 92-101.
- Yue, S., R. M. Pilliar, et al. (1984). "The fatigue strength of porous-coated Ti-6%Al-4%V implant alloy." Journal of Biomedical Material Research **18**: 1043-1058.
- Zardiackas, L. D., D. E. Parsell, et al. (2001). "Structure, Metallurgy, and Mechanical Properties of a Porous Tantalum Foam." Journal of Biomedical Material Research **58**(2): 180-187.
- Zhang, G., R. A. Latour, et al. (1996). "Long-term compressive property durability of carbon fibre-reinforced polyetheretherketone composite in physiological saline." Biomaterials **17**: 781-789.
- Zhang, X., R. A. Ayers, et al. (2001). "Combustion synthesis of porous materials for bone replacement." Biomedical sciences instrumentation **37**: 463-468.

## **8. APPENDIX**

## 8.1. Appendix 1

**Table 14: List of Cadaver Bones**

<b>Bone ID</b>	<b>Dog-Type</b>	<b>M/F</b>	<b>weight lb</b>	<b>Reason</b>	<b>Method</b>
Bone1	Hound-mix	male	54.5	from Owners	euthanize-lethal injection
Bone2	Boxter	female	64.5	from Owners	euthanize-lethal injection
Bone3	lab-mix	male	102.5	Stray	euthanize-lethal injection
Bone4	Rott Wheeler	female	87.5	surrender	euthanize-lethal injection
Bone5	Black lab mix	male	59	owner surrender (bite)	euthanize-lethal injection
Bone6	pittbull mix	female	54.9	aggressive	euthanize-lethal injection
Bone7	pittbull mix	male	64.6	aggressive	euthanize-lethal injection
exclude	Great dane	male	114	aggressive	euthanize-lethal injection
Bone8	pittbull mix	female	82	owner surrender	euthanize-lethal injection
Bone9	Rott Wheeler	male	100	owner surrender	euthanize-lethal injection
Bone10	pittbull mix	male	60	owner surrender	euthanize-lethal injection
Bone11	lab-mix	male	77	owner surrender	euthanize-lethal injection
Bone12	german shepherd	male	86	owner surrender	euthanize-lethal injection
Bone13	Great dane	female	106	owner surrender	euthanize-lethal injection
Bone14	pittbull mix	male	63	owner surrender	euthanize-lethal injection

## 8.2. Appendix 2

**Table 15: Cadavre surgery notes**

Specimen	Hip Stem	Final Position	Notes	Method
Bone2-Left	Wait for EBM8			Broached(B#8) -1mm.
Bone5-Left	BFX9	0mm	Nutrient foreman cranially	Initial DD:entire beaded region OB#10 at Line 5: DD is 14mm OB#10 at Line 4: DD is 12mm OB#10 at Line 3: DD is 11mm OB#10 at Line 2: DD is 6mm
Bone8-Left	EBM9	+1mm	Hip dysphasia. Cranial medial foreman small.	Broached(#9) -2mm Initial DD is 24mm OB#10 at Line 3: DD is 13mm OB#10 at Line 1.5: DD is 7mm
Bone9-Left	BFX9	+2mm		Broached (#9) is at neck cut Initial DD is 22mm OB#10 at Line 4: DD is 16mm OB#10 at Line 3: DD is 11mm OB#10 at Line 2.5: DD is 6mm
Bone8-Right	BFX9	-2mm	Cranial foreman small	Broached(#9):-2mm to neck cut Initial DD is 2mm
Bone1-Right	EBM9	+2mm	Cranial foreman small	Broached(#9) is flash to neck cut Initial DD is 19mm OB#10 at Line 4: DD is 12mm OB#10 at Line 2: DD is 10mm OB#10 at Line 1: DD is 7mm
Bone7-Right	BFX8	-3mm		Broached(#8): -3mm to neck cut Initial DD is 6mm

**Table 15 (Continued)**

Bone1-Left	BFX9	+1mm		Broached(#9) is flash to neck cut Initial DD is 15mm OB#10 at Line 3: DD 7mm
Bone4-Right	BFX11	0mm	Cranial foreman small	Broached (#11) is at -1mm to neck cut Initial DD: 6mm
Bone11-Left	EBM10	+5mm	Cranial foreman small	Broached(#10) is at 1mm to neck cut Initial DD is 24mm OB#11 at Line 2: DD is 15mm OB#11 at 1mm to Line 1: DD is 12mm OB#11 at Line 1: DD is 10mm
Bone5-Right	EBM9	+2mm		Broached(#9) is 0mm to neck cut Initial DD is 16mm OB#10 at Line 3: DD is 13mm OB#10 at Line 2: DD is 13mm Impacted: 6mm beads exposed Extracted and #7broach was used to file edges OB#10 at Line 1: DD is 6mm
Bone9-Right	EBM9	+3mm		Broached(#9) is at -4mm to neck cut Initial DD is 14mm OB#10 Line 3: DD is 10mm OB#10 Line 2: DD is 9mm OB#10 Line 1: DD is 6mm
Bone11-Right	BFX10	-2mm	Cranial foreman small	Broached(#10) is at -3mm to neck cut Initial DD is 4mm Impacted without OB
Bone3-Right	BFX10	0mm		Broached(#10) is at -2mm to neck cut Initial DD is 4mm
Bone12-Right	BFX10	-4mm	Cancellous bone has gray color	Broached(#10) is at -4mm to neck cut Initial DD is 8mm

**Table 15 (Continued)**

<b>Specimen</b>	<b>Hip Stem</b>	<b>Final Position</b>	<b>Notes</b>	<b>Method</b>
Bone3-Left	EBM10	+1mm	Cranial foreman small	Broached(#10) is at -2mm to neck cut Initial DD is 18mm OB#11 Line 2: DD is 14mm OB#11 1mm from Line 1: DD is 8mm OB#11 Line 1: DD is 4mm
Bone12-Left	EBM10	+2mm		Broached(#10) is at -2mm to neck cut Initial DD is 19mm OB#11 Line 2: DD is 12mm OB#11 Line 1: DD is 8mm
Bone13-Right	BFX11	-1mm		Broached(#11) is at -1mm to neck cut Initial DD is 6mm Impacted without OB

### 8.3. Appendix 3

**Table 16: Xray templating**

Templating of radiographs									
Number	Technique	View	Magnification	Maximal size	Optimal size	View	Magnification	Maximal size	Optimal size
#14 (D)	45/7.5	CC	2%	10 (loose)	10 (loose)	ML	2%	11+	10 (loose)
#18 (D)	45/7.5	CC	2%	11+	11	ML	2%	11+	11 (loose)
#12 (D)	44/7.5	CC	2%	9	9 (tight)	ML	2%	9	9
#6 (OC)	42/7.5	CC	1.50%	9	8 (tight)	ML	2%	9	8
#7 (OC)	44/7.5	CC	2%	10	9 (loose)	ML	2.25%	10	9
#13 (D)	42/7.5	CC	1.25%	9	8 (loose)	ML	2%	9	8
#16 (D)	43/7.5	CC	1.75%	10	10 (tight)	ML	2.75%	10	10
#9 (OC)	41/7.5	CC	1.75%	10	10 (loose)	ML	2%	10	10
Notes		Templates with #5 to #10 templates with "0%" magnification.							
		Final implant size is chosen most often as the optimal size on the CC view							
		The bone are slightly magnified and therefore the optimal size is likely to be the size							
		used during implantation							
		The fit (loose or tight) is indicated after the implant size.							
		With loose implant the use of the next size up is possible.							
		Key: CC, cranio-caudal; ML, medio-lateral							

Table-16 (Continued)

Number	Technique	View	Magnification	Maximal size	View	Magnification	Maximal size
A	?	CC	3.50%	10 (tight)	ML	3.00%	11(loose)
B	?	CC	2.25%	9(tight)	ML	2.50%	10(tight)
C	?	CC	2.25%	10(very tight)	ML	2.50%	11(loose)
D	?	CC	2.50%	11(loose)	ML	2.75%	11(loose)
E	?	CC	2.00%	9(loose)	ML	2.25%	10(loose)
Note from Dr. Marcelline							
<p>I made a subjective decision about the largest size that would fit in the canal. Some of them are tight and some are loose, based on the relative fit of the stem in the bone. Because the radiographs are slightly magnified but the templates are not, the bone is not quite as large in reality compared to the radiographs. It is therefore likely that something that appears tight during templating may not be achievable during implantation. Practically, this means that for a femur templated as '10 tight', a 9 implant may be required but for a femur templated at 9 loose, a 9 implant may also be required.</p> <p>Please note that the templated values are different for the CC and ML views. It is my impression that the bone in most instances accepts larger stems in the cranial to caudal direction compared to the medial to lateral direction. The first list of value, because they are smaller (by 1 size in all cases), have priority.</p>							